

26962



National Library
of Canada

Bibliothèque nationale
du Canada

CANADIAN THESES
ON MICROFICHE

THÈSES CANADIENNES
SUR MICROFICHE

NAME OF AUTHOR / NOM DE L'AUTEUR DAVID K. WONG

TITLE OF THESIS / TITRE DE LA THÈSE MICROWAVE DIELECTRIC
CONSTANTS OF METAL OXIDES
AT HIGH TEMPERATURES

UNIVERSITY / UNIVERSITÉ UNIVERSITY OF ALBERTA

DEGREE FOR WHICH THESIS WAS PRESENTED /
GRADE POUR LEQUEL CETTE THÈSE FUT PRÉSENTÉE M.Sc.

YEAR THIS DEGREE CONFERRED / ANNÉE D'OBTENTION DE CE GRADE 1975

NAME OF SUPERVISOR / NOM DU DIRECTEUR DE THÈSE DR. W. TINGA

Permission is hereby granted to the NATIONAL LIBRARY OF
CANADA to microfilm this thesis and to lend or sell copies
of the film.

The author reserves other publication rights, and neither the
thesis nor extensive extracts from it may be printed or other-
wise reproduced without the author's written permission.

L'autorisation est, par la présente, accordée à la BIBLIOTHÈ-
QUE NATIONALE DU CANADA de microfilmer cette thèse et
de prêter ou de vendre des exemplaires du film.

L'auteur se réserve les autres droits de publication, ni la
thèse ni de longs extraits de celle-ci ne doivent être imprimés
ou autrement reproduits sans l'autorisation écrite de l'auteur.

DATED / DATE 8-10-75 SIGNED / SIGNÉ David K. Wong

PERMANENT ADDRESS / RÉSIDENCE FIXE 23 MACDONNELL RD
402
HONG KONG

THE UNIVERSITY OF ALBERTA

MICROWAVE DIELECTRIC CONSTANTS OF METAL OXIDES AT
HIGH TEMPERATURES

by

DAVID K. WONG

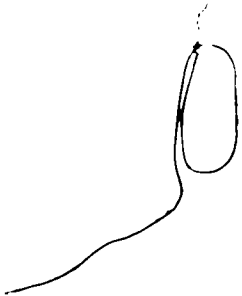
A THESIS

SUBMITTED TO THE FACULTY OF GRADUATE STUDIES
IN PARTIAL FULFILMENT OF THE REQUIREMENTS FOR THE DEGREE
OF MASTER OF SCIENCE

DEPARTMENT OF ELECTRICAL ENGINEERING

EDMONTON, ALBERTA

FALL 1975



THE UNIVERSITY OF ALBERTA
 FACULTY OF GRADUATE STUDIES AND RESEARCH

The undersigned certify that they have read, and recommend to the Faculty of Graduate Studies and Research for acceptance, a thesis entitled Microwave Dielectric Constant of Metal Oxides at High Temperatures submitted by David K. Wong in partial fulfilment of the requirements for the degree of Master of Science.

M. J. King

 Supervisor
Frank C. Wesche

W. ...

Date *August 29, 1975*

ABSTRACT

Metallic oxide and sulfide powders heated by microwaves at 2.45 GHz were, according to the literature, reported to exhibit a cut-off temperature phenomena. The temperature "cut-off" effect was thought to be caused by an increase of conductivity of the sample causing most of the microwave energy impinging on the sample to be reflected. Since microwave heating is strongly dependent on the dielectric loss, which include conductivity effects, in a material, the purpose of this thesis is to investigate the microwave dielectric properties of metal oxides as a function of temperature. Results of the investigation are used to explain the temperature "cut-off" phenomena.

Dielectric measurements were made using a thin, short, rectangular sample centered in a waveguide. Resulting data were interpreted using a modified waveguide perturbation theory by accounting for sample interface reflections. The final equations had to be solved iteratively. Temperatures were varied over the range 25°C - 900°C. Results of experiments show that the microwave heating rate for the compounds tested depends strongly on the dielectric constant ϵ' and loss factor ϵ'' . High values of ϵ' and ϵ'' cause more microwave energy to be reflected. The amount of energy in the form of heat absorbed by the sample is determined by ϵ'' . For most of the materials tested, both ϵ' and ϵ'' values

increase with increasing temperature causing more microwave energy impinging on the sample to be reflected. Nevertheless, some energy is still transmitted and absorbed by the sample. This absorbed energy is balanced by heat energy loss to the surroundings through conduction, convection and radiation. This balance of energy leads to the temperature "cut-off" phenomena observed. In other words, the sample temperature increases to a given maximum value and remains constant at that level with respect to heating time. Higher "cut-off" temperatures can be obtained by applying a higher level of microwave power to the sample. Dielectric data obtained from the experiments show a number of interesting characteristics including an apparent relaxation peak for zinc oxide occurring at about 200°C. However, experimental accuracy was rather limited for some of the materials tested due to inherently low dielectric loss factors. Further interpretation of the oxides' dielectric behavior versus temperature requires more accurate data.

Errors are mainly caused by attenuation uncertainties and the approximate theory used to calculate the dielectric constant from the experimental data.

ACKNOWLEDGEMENT

I am most grateful to Dr. W. R. Tinga for his patient guidance and encouraging discussions throughout this work. I would also like to extend my sincere gratitude to Dr. Y. Nigrin for his many helpful suggestions. In addition, I acknowledge the skilful aids of the technical staffs of the Department.

TABLE OF CONTENTS

<u>CHAPTER</u>		<u>PAGE</u>
1	INTRODUCTION	1
	A. Purpose of the Thesis	1
	B. Review of the Literature	3
	C. Choice of Method	6
	D. Choice of Sample	9
	E. Outline of each Chapter	9
	List of Footnotes	11
2	THEORY	12
	A. Introduction	12
	B. Development and Limitations of Perturbation Theory	14
	C. Theory of Reflection from a Multiple Interface	23
	D. Iteration Technique used	28
	E. Higher Mode Interference	34
	List of Footnotes	39
3	EXPERIMENTAL METHODS	40
	A. Introduction	40
	B. Experimental set-up	40
	1. Precision Bridge Circuit	40
	2. Sample Mount Design	44
	3. Temperature Control and Detection	45
	C. Calibration	47
	1. Calibration of Sample Temperature	47

2. Phase-shifter Calibration	47
3. Calibration of the microwave bridge using samples with known Complex Dielectric Constants and comparing results of calculations of two sample cells on the same sample	48
D. Measurement Procedure	50
E. Measurement Errors	51
1. Mismatch Errors	51
2. Errors due to Thermal Expansion	51
3. Multimode Propagation Errors	52
4. Temperature Variation Errors	55
5. Violation of Perturbation Theoretical Assumptions	55
6. Other Experimental Errors	55
F. Heating Time Measurement using Microwave Energy	57
Experimental Set-up and Measurement Procedure	57
List of Footnotes	60
4 EXPERIMENTAL RESULTS AND ANALYSIS	62
A. Introduction	62
B. Experimental Results	63
C. Analysis of Data	82
1. Data on Physics and Metallurgy of Materials Tested	82
2. Probable Dielectric loss Mechanism - Dipolar Relaxation and Conductivity	86
3. Explanation of Temperature cut-off Effect	95
List of Footnotes	99
5 CONCLUSION	100
BIBLIOGRAPHY	103

APPENDIX A - ERROR ANALYSIS	108
APPENDIX B - COMPUTER PROGRAM FOR ITERATION METHOD	113
APPENDIX C - IMPURITIES OF COMPOUNDS TESTED	115

LIST OF TABLES

<u>TABLE</u>		<u>PAGE</u>
4-1	Comparison of test results and literature data	64
A-1	Summary of uncertainty errors for CuO	100
A-2	Total uncertainty errors for sample materials tested	101
A-3	Estimated worst case error due to evanescent modes	112

LIST OF FIGURES

	<u>PAGE</u>
Fig. 1-1 Microwave heating curve for CuO	2
Fig. 2-1 S-band guide and sample slab cross-section	14
Fig. 2-2 Attenuation versus filling factor (w/a) in WR-975 waveguide at $f = 915$ MHz (20)	20
Fig. 2-3 Compression of E field into slab of high ϵ' in a waveguide (22)	20
Fig. 2-4 Polarization around sample with w comparable to h (23)	20
Fig. 2-5 Construction of quartz sample cell	22
Fig. 2-6 Multiple reflections of three layers of dielectric in a rectangular waveguide, top view	24
Fig. 2-7 Reflection from an interface of two dielectrics	24
Fig. 2-8 Top view of sample mount and sample cell	28
Fig. 2-9 Flow diagram of iteration method used	33
Fig. 2-10 Symmetrically loaded waveguide	35
Fig. 2-11 Comparison of approximate propagation constant with exact solution as a function of relative dielectric constant (17)	35
Fig. 2-12 Comparison of approximate propagation constants with exact solution as a function of dielectric thickness (17)	36
Fig. 2-13 Mode filter construction and wall current for TE_{10} , TE_{20} , TE_{01} modes	38
Fig. 3-1 Experimental apparatus	41
Fig. 3-2 Sample mount construction detail	43
Fig. 3-3 Sample temperature calibration set-up	46
Fig. 3-4 Metal lens and lens barrel of infrared camera detail	46

Fig. 3-5	Phase change as a function of temperature due to expansion of sample mount	53
Fig. 3-6	Percentage difference between the values of the propagation constant $\gamma = \alpha + j\beta$ as a function of w/a and ϵ_r at 34.5 GHz for $\sigma = 10$ mho/m or $\epsilon'' = 73.37$ (26.)	54
Fig. 3-7	Microwave heating set-up	58
Fig. 4-1	Real and imaginary parts of complex dielectric constant of CuO as a function of temperature at 2.45 GHz and density of 2.3079 gm/cc	66
Fig. 4-2	Real and imaginary parts of complex dielectric constant of CuS as a function of temperature at 2.45 GHz and density of 1.549 gm/cc	67
Fig. 4-3	Real and imaginary parts of complex dielectric constant of CaO as a function of temperature at 2.45 GHz and density of 0.275 gm/cc	68
Fig. 4-4	Real and imaginary parts of complex dielectric constant of ZnO as a function of temperature at 2.45 GHz, density of .816 gm/cc. See figure 4-5 also	70
Fig. 4-5	Real and imaginary parts of complex dielectric constant of ZnO as a function of temperature at 2.45 GHz and density of .816 gm/cc (second interpretation)	71
Fig. 4-6	Real and imaginary parts of complex dielectric constant of PbO as a function of temperature at 2.45 GHz and density of 2.78 gm/cc after oven drying at 100°C for 12 hours. See figure 4-7 also	73
Fig. 4-7	Real and imaginary parts of complex dielectric constant of PbO as a function of temperature at 2.45 GHz and density of 2.49 gm/cc before oven drying	74
Fig. 4-8	Detected temperature versus time of CuO using microwave heating with sample density of 2.29 gm/cc	75
Fig. 4-9	Percentage power reflection versus detected temperature of CuO using microwave heating with sample density of 2.29 gm/cc	76
Fig. 4-10	Detected temperature versus time for ZnO using microwave heating with sample density of .82 gm/cc	77

Fig. 4-11	Detected temperature versus percentage reflection of ZnO using microwave heating with sample density of .82 gm/cc	79
Fig. 4-12	Complex dielectric constant of CuO as a function of density at room temperature	81
Fig. 4-13	Build-up of polarization upon sudden application of steady field(34)	88
Fig. 4-14	Decay of polarization upon sudden removal of steady field(34)	88
Fig. 4-15	Debye curves for a dielectric material with $\epsilon_s=8$, $\epsilon_{e1}=2$ (36)	90
Fig. 4-16	Shift of ϵ'' curve as temperature increases	92
Fig. 4-17	Shift of ϵ' curve as temperature increases	92
Fig. 4-18	Loss factor ϵ'' as a function of temperature T showing separate effects of dipolar relaxation and conductivity. (refer to figure 4-4)	93
Fig. 4-19	Loss factor ϵ'' as a function of temperature T with effects of dipolar relaxation and conductivity overlap. (refer to figure 4-1)	94

CHAPTER 1

INTRODUCTION

A. Purpose of the Thesis

The use of microwaves as a source of heat energy has become increasingly attractive. The desirable features of microwave energy are its selectivity whereby materials can be heated to a high temperature in relatively cool surroundings, and the rapidity with which the heating can be accomplished. However, parameters such as heating rate, temperature rise and power penetration depth all depend strongly on the complex dielectric constant of the material being treated(1). Therefore, in order to utilize microwave energy effectively and economically, adequate information about microwave properties of material must be available.

Behavior of metallic oxide and sulfide powders heated by microwaves at 2.45 GHz has been reported by Ford and Pei(2). In their experiment, a different heating rate for different oxide samples was observed. But the most interesting phenomena observed was the existence of a "cut-off" temperature for a number of oxides beyond which the temperature remained constant even after further increase of microwave energy, see figure 1-1. The temperature "cut-off" effect was thought to be caused by an increase of conductivity of the sample causing microwave energy

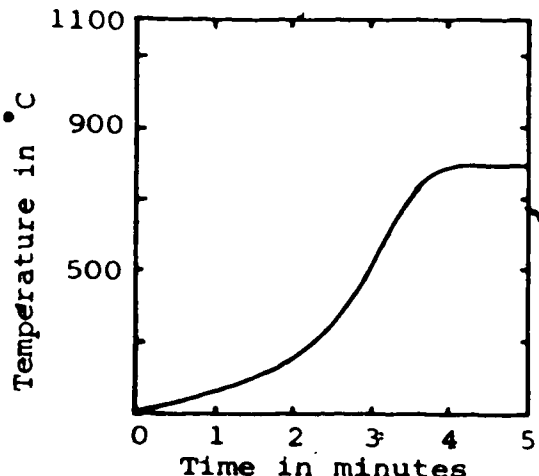


Fig. 1-1 Microwave heating curve for CuO

impinging on the sample to be mainly reflected. But this theory remains untested and the temperature "cut-off" phenomena remains unexplained.

Since microwave heating is strongly dependent on the dielectric loss in a material, a study of the dielectric

properties as a function of temperature and frequency should reveal the answer to the temperature "cut-off" phenomena.

A literature search reveals that there is little data available on the microwave properties of metal oxides at high temperatures. This makes the analysis of these materials and the general prediction of their microwave heating behavior quite difficult. The purpose of this thesis is to investigate the complex dielectric constants of cupric oxide, cupric sulfide, calcium oxide, lead oxide and zinc oxide as a function of temperature up to 900°C, the upper temperature limit of 900°C being set by experimental limitations. Secondly, such data will be used to explain the temperature "cut-off" phenomena.

B. Review of the Literature

In 1953, an extensive compilation of dielectric data in the frequency range from 100 Hz to 25 GHz and temperature range from -200°C to 600°C was published by Von Hippel(3). His book includes a general theory of dielectrics and its measurement techniques.

In 1967, the experiment on high temperature chemical processing of metal oxides using microwaves was performed by Ford and Pei(2). The following year, a swept frequency technique was used on cupric oxide by Ford and Tinga(4) to investigate the high temperature complex dielectric constant of cupric oxide and other metallic oxides. The temperature reached then for cupric oxide was only 270°C and there was no conclusive data to quantify the temperature cut-off effect of metallic oxides.

In 1970, a publication entitled "Standard Methods of Tests for Complex Permittivity of Solid Electrical Insulating Materials at Microwave Frequencies and Temperatures to 1650°C " was published by the American National Standards Institute(5). The paper outlined the shorted transmission line method and the resonant cavity perturbation method for testing solid specimens at high temperature.

A high temperature shorted line measurement was also made on alumina at 10 GHz by Wickenden and Duesden in 1972(6).

This paper described the use of the shorted-line technique for the measurement of permittivity and loss tangent of alumina at elevated temperatures. The method of computing the dielectric parameters from the observed VSWR and displacement of the minima due to the introduction of the sample was outlined and the errors associated with this type of measurement were discussed. The above methods are not ideally suitable for the materials under consideration here.

In 1973, dielectric properties of materials for microwave processing were tabulated by Tinga and Nelson(7). A brief description was given of the dielectric dispersion and relaxation as a function of frequency and temperature. The dielectric constant and loss factor of many materials were tabulated as functions of frequency, temperature, moisture content, and composition. Materials were classified as Agricultural products, Biological materials, Foods, Forest products, Leather, Rubber, and Soil and Minerals. However, no information relating to metal oxides and sulfides was found in this tabulation.

Recently, Couderc(8) used a bi-modal technique to determine complex dielectric constants of Mycalex, Centralab type 302, Corning 7740 and iron sulfide as a function of temperature. His method used one resonant cavity mode for heating and simultaneously another mode for measurement.

Since the two modes were well isolated electrically, samples could be heated and measured simultaneously with microwaves. However, Couderc's method would be limited to temperatures below "cut-off" temperatures for metal oxide measurements.

Another important contribution to the understanding of temperature and frequency dependence of the complex dielectric constant of metal oxides was made by Weichman (9) in 1969. In his paper, variation of complex dielectric constant of cuprous oxide, Cu_2O , as a function of temperature (274.5 K to 314.5 K) and frequency (8 Hz to 26 KHz) is related to the variation in the depletion layer formed around each copper inclusion embedded in the semiconducting material. Calculations are based on a highly simplified model of the copper inclusions. Behavior of other semiconducting metal oxides was believed due to the same mechanism.

C. Choice of Method

When looking for an appropriate technique for measuring the complex dielectric constant of materials at microwave frequencies (3, 10, 11, 12, 13, 14, 15) one finds that measurement techniques are divided into three major classes: 1) resonant cavity methods, 2) free space methods and 3) transmission line or waveguide methods. The choice of a particular method is determined by a) geometry and makeup of the sample to be tested, b) environmental requirements for the sample, c) simplicity of the measurement, d) accuracy desired and e) frequency used. After a particular method is chosen, the experimental technique is modified to suit a particular need.

The requirement for reasonable temperature control at high temperatures narrows the choice of method down to either the resonant cavity method or the transmission line method by which samples can be confined in a cavity or a waveguide and then insulated against heat loss.

For the two ISM^a frequencies used in industry, namely 915 MHz and 2450 MHz, a resonant cavity would be large and difficult to heat uniformly using external heating elements. Thus a waveguide method was chosen (16).

To assure rapid and, above all, uniform heating, a sample partially filling a waveguide in a region of

7

relatively uniform electric field is used. Sample length is chosen to give a reasonable temperature distribution and a measurable attenuation.

Using a precision microwave bridge, the propagation constant of the sample is determined by applying perturbation theory to the thin dielectric sample in the waveguide. However, measured attenuation and phase shift values obtained from the bridge cannot be used in the perturbation theory directly due to interface reflection and higher order mode propagation in the sample mount.

To correct for interface reflection, the multiple reflection problem is solved to yield a transcendental equation with respect to the propagation constant of the composite guide and sample, γ . By solving the resulting equation iteratively, assuming a trial solution of the complex dielectric constant, the actual γ can be calculated.

Regarding higher order mode propagation, Hord and Rosenbaum (17) showed that a two-mode approximation should yield accurate values (-10%) of the measured propagation constant for most waveguide loadings. Since the TE_{01} mode is coupled most strongly to the TE_{10} mode, and its cut-off frequency is the lowest of the coupled higher order modes, longitudinal slots cut in the middle of both broad waveguide walls should prevent the

propagation of the TE_{01} mode and attenuate the propagation of the TE_{20} mode. With the two higher order modes effectively filtered out, propagation will essentially be in the fundamental mode thus satisfying another of the requirements necessary for the application of perturbation theory. However, there are mode conversions (evanescent modes) in the front and the back of the sample slab. Since the length of the sample slab is small compared with a wavelength, these local mode conversion effects could cause an increase in measured attenuation values. However, in the error calculation and estimations, these effects are accounted for.

D. Choice of Sample

For materials tested by Ford and Pei, cut-off temperatures reached as high as 1900°C . To achieve this high temperature, one requires a large energy source to heat the sample and good insulation to prevent heat loss and damage to adjacent measurement equipment. Thus, the choice of sample is in practice determined by the maximum attainable temperature of the available equipment and availability of the sample. Due to these limitations, reagent grade cupric oxide, cupric sulfide, calcium oxide, lead oxide, and zinc oxide were chosen. Their cut-off temperatures at 800°C , 600°C , 200°C , 900°C and 1100°C respectively are typical of the materials tested by Ford and Pei. Yet, these temperatures are low enough to allow the use of conventional heating methods using external electrical heating elements.

E. Outline of each Chapter

Chapter two is devoted to the development of the perturbation theory, its limitations and a solution to the multiple interface reflection problem for which an iteration method is used. Approximation techniques for dielectric loaded waveguide and design of the mode filter are also outlined in this chapter.

With the help of the perturbation theory and the theory of multiple reflections, dielectric constants for cupric oxide,

cupric sulfide, calcium oxide, zinc oxide, and lead oxide are calculated from data obtained using a microwave bridge technique. The validity of the measurement method used is then tested using samples with known complex dielectric constant. Chapter three gives the detailed construction of the measurement bridge circuit, the measurement procedure, the heating method and the calibration procedure. Sources of errors are also discussed in the same chapter.

Results of the bridge calibration, measurements on different metal oxides and/or sulfides and temperature versus time measurements using microwave heating are given in Chapter four. It is shown that the behavior of these materials as a function of temperature can be explained by the dipolar relaxation and conductivity of the material tested. The so-called "cut-off" temperature for a material seems to be due to a balance between input microwave energy and heat loss through conduction, convection and radiation.

List of Footnotes

^aISM stands for Industrial Scientific and Medical.

CHAPTER 2

THEORY

A. Introduction

A detailed review of the perturbation theory, its limitations and its use in calculating the sample's complex dielectric constant will be given in this chapter.

Internal reflections from the sample's boundaries and those of the quartz sample cell being used will give erroneous readings of sample attenuation and phase shift. To improve these readings, the multiple reflection problem for three layers of lossy dielectric is solved. Since this results in a transcendental equation, an iteration method is developed using both the perturbation theory and the multiple reflection theory to solve for the complex dielectric constant of the sample tested using the experimental data.

It was shown in the paper by Hord and Rosenbaum(17) that a centre-loaded guide will introduce an overmoding problem. Since the modes coupled most strongly to the fundamental mode are the lowest order modes with the lowest propagation cut-off frequencies, accounting for the next two higher order modes will give improved results. For our experiment, rather than solving the two modes

approximation problem mathematically, a mode filter was constructed to suppress higher order modes, thus improving the accuracy of measurement results. Theory of the two mode approximation will be given in the last section of this chapter.

B. Development and Limitations of Perturbation Theory

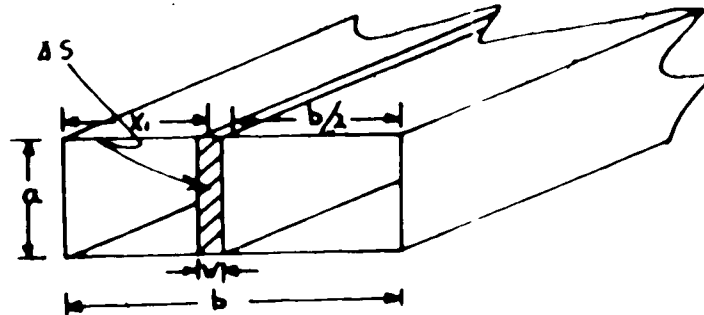


Fig. 2-1 S-band guide and sample slab cross-section

Following Altman(18) and Sookoo(19), the perturbation problem is solved below. Consider an infinite uniform waveguide with an infinite, uniform slab of dielectric centered on the broad wall of the waveguide as shown in figure 2-1. For the composite structure, let the propagation constant and the fields at each point be γ , \vec{E} and \vec{H} respectively and characterize the perturbing region by ϵ and μ . For the unperturbed waveguide without the dielectric slab, denote the same quantities above with a zero subscript.

Then \vec{E} and \vec{H} will have the form

$$\vec{E} = \vec{E}' e^{j(\omega t - \gamma z)} \quad (2.1)$$

$$\vec{H} = \vec{H}' e^{j(\omega t - \gamma z)} \quad (2.2)$$

where \vec{E}' and \vec{H}' are functions only of the transverse coordinates

For the unperturbed waveguide, Maxwell's equations then

become

$$\nabla_x \vec{H}_0 = \nabla_x (\vec{H}'_0 e^{j(\omega t - \gamma z)}) = j\omega \epsilon_0 \vec{E}'_0 e^{j(\omega t - \gamma z)} \quad (2.3)$$

$$\nabla_x \vec{E}_0 = \nabla_x (\vec{E}'_0 e^{j(\omega t - \gamma z)}) = -j\omega \mu_0 \vec{H}'_0 e^{j(\omega t - \gamma z)} \quad (2.4)$$

Using the vector identity,

$$\begin{aligned}\nabla \times a \vec{M} &= a \nabla \times \vec{M} + (\nabla a) \times \vec{M} \\ \nabla \times (\vec{H}_0' e^{j\omega t - \gamma_0 z}) &= e^{j\omega t - \gamma_0 z} (\nabla \times \vec{H}_0') + (\nabla e^{j\omega t - \gamma_0 z}) \times \vec{H}_0' \\ &= e^{j\omega t - \gamma_0 z} [\nabla \times \vec{H}_0' - \vec{a}_z \times j \gamma_0 \vec{H}_0']\end{aligned}\quad (2.5)$$

where \vec{a}_z is the unit vector in the z direction.

Then, equations (2.3) and (2.4) become

$$(\nabla \times \vec{H}_0') - (\vec{a}_z \times j \gamma_0 \vec{H}_0') = j \omega \epsilon_0 \vec{E}_0' \quad (2.6)$$

$$(\nabla \times \vec{E}_0') - (\vec{a}_z \times j \gamma_0 \vec{E}_0') = -j \omega \mu_0 \vec{H}_0' \quad (2.7)$$

Similarly for the perturbed waveguide,

$$(\nabla \times \vec{H}') - (\vec{a}_z \times j \gamma \vec{H}') = j \omega \epsilon_0 \vec{E}' \quad \text{outside } \Delta S \quad (2.8)$$

$$(\nabla \times \vec{H}') - (\vec{a}_z \times j \gamma \vec{H}') = j \omega \epsilon \vec{E}' \quad \text{inside } \Delta S \quad (2.9)$$

$$(\nabla \times \vec{E}') - (\vec{a}_z \times j \gamma \vec{E}') = -j \omega \mu_0 \vec{H}' \quad \text{outside } \Delta S \quad (2.10)$$

$$(\nabla \times \vec{E}') - (\vec{a}_z \times j \gamma \vec{E}') = -j \omega \mu \vec{H}' \quad \text{inside } \Delta S \quad (2.11)$$

Multiplying equations (2.8) and (2.9) by $\vec{E}_0'^*$ yields

$$(\vec{E}_0'^* \cdot \nabla \times \vec{H}') - (\vec{E}_0'^* \cdot \vec{a}_z \times j \gamma \vec{H}') = j \omega \epsilon_0 \vec{E}_0'^* \cdot \vec{E}' \quad \text{outside } \Delta S \quad (2.12)$$

$$(\vec{E}_0'^* \cdot \nabla \times \vec{H}') - (\vec{E}_0'^* \cdot \vec{a}_z \times j \gamma \vec{H}') = j \omega \epsilon \vec{E}_0'^* \cdot \vec{E}' \quad \text{inside } \Delta S \quad (2.13)$$

where * represents the complex conjugate.

Similarly, equations (2.10) and (2.11) become

$$(\vec{H}_0'^* \cdot \nabla \times \vec{E}') - (\vec{H}_0'^* \cdot \vec{a}_z \times j \gamma \vec{E}') = -j \omega \mu_0 \vec{H}_0'^* \cdot \vec{H}' \quad \text{outside } \Delta S \quad (2.14)$$

$$(\vec{H}_0'^* \cdot \nabla \times \vec{E}') - (\vec{H}_0'^* \cdot \vec{a}_z \times j \gamma \vec{E}') = -j \omega \mu \vec{H}_0'^* \cdot \vec{H}' \quad \text{inside } \Delta S \quad (2.15)$$

Multiplying equations (2.6) and (2.7) by \vec{E}' and \vec{H}'

respectively gives

$$(\vec{E}' \cdot \nabla \times \vec{H}_0'^*) + (\vec{E}' \cdot \vec{a}_z \times j \gamma_0 \vec{H}_0'^*) = -j \omega \epsilon_0 \vec{E}_0'^* \cdot \vec{E}' \quad (2.16)$$

$$(\vec{H}' \cdot \nabla \times \vec{E}_0'^*) + (\vec{H}' \cdot \vec{a}_z \times j \gamma_0 \vec{E}_0'^*) = j \omega \mu_0 \vec{H}_0'^* \cdot \vec{H}' \quad (2.17)$$

Combining equations [(2.12)+(2.16)-(2.14)-(2.17)] and integrating over the rectangular volume V, with sides a,

$$\begin{aligned}
& \int_V \{ [\vec{E}'^* \cdot \vec{\nabla} \times \vec{H}' + \vec{E}' \cdot \vec{\nabla} \times \vec{H}'^*] - [\vec{H}'^* \cdot \vec{\nabla} \times \vec{E}' + \vec{H}' \cdot \vec{\nabla} \times \vec{E}'^*] \} dV \\
& - j(\gamma - \gamma_0) \int_V [\vec{E}'^* \cdot \vec{a}_z \times \vec{H}' - \vec{H}'^* \cdot \vec{a}_z \times \vec{E}'] dV \\
& = j\omega \int_{\Delta V} [(\epsilon - \epsilon_0) \vec{E}'^* \cdot \vec{E}' + (\mu - \mu_0) \vec{H}'^* \cdot \vec{H}'] dV \quad (2.18)
\end{aligned}$$

Using the vector identity,

$$\vec{\nabla} \times (\vec{A} \times \vec{B}) = \vec{B} \cdot (\vec{\nabla} \times \vec{A}) - \vec{A} \cdot (\vec{\nabla} \times \vec{B})$$

the first integral becomes,

$$\int_V [\vec{\nabla} \cdot (\vec{H}' \times \vec{E}'^*) + \vec{\nabla} \cdot (\vec{H}'^* \times \vec{E}')] dV \quad (2.19)$$

Using the divergence theorem, (2.19) becomes,

$$\begin{aligned}
& \int_V [\vec{\nabla} \cdot (\vec{H}' \times \vec{E}'^*) + \vec{\nabla} \cdot (\vec{H}'^* \times \vec{E}')] dV \\
& = \int_S (\vec{H}' \times \vec{E}'^* + \vec{H}'^* \times \vec{E}') \cdot d\vec{a} \quad (2.20)
\end{aligned}$$

where S is the surface enclosing the volume V . For propagation of the fundamental mode, \vec{E}' and \vec{E}'^* are perpendicular to the conducting surface of the waveguide, thus parallel to $d\vec{a}$, the outward normal vector at the waveguide surface, and the surface integral (2.20) vanishes. However, depolarization of the field and propagation of other than TE modes will introduce \vec{E}' and \vec{E}'^* components which are not perpendicular to the conducting surface of the waveguide. Thus equation (2.20) will have a finite value and errors will develop in the subsequent equations. Therefore, equation (2.18) reduces to

$$\begin{aligned}
& -j(\gamma - \gamma_0) \int_V [\vec{E}'^* \cdot \vec{a}_z \times \vec{H}' - \vec{H}'^* \cdot \vec{a}_z \times \vec{E}'] dV \\
& = j(\gamma - \gamma_0) \int_V [\vec{E}'^* \times \vec{H}' - \vec{H}'^* \times \vec{E}'] \cdot \vec{a}_z dV \quad (2.20A)
\end{aligned}$$

With the existence of evanescent modes at both ends of the sample slab neglected, equation (2.20A) must remain true for any length, so that integration over the cross-sections must also be equal assuming uniform cross-section. Here

modes than TE modes and,

$$\begin{aligned} \gamma - \gamma_0 &= j\omega \int_S [(\vec{E}'^* \times \vec{H}') - (\vec{H}'^* \times \vec{E}')] \cdot d\vec{a} \\ &= j\omega \int_S [(\epsilon - \epsilon_0) \vec{E}'^* \cdot \vec{E}' + (\mu - \mu_0) \vec{H}'^* \cdot \vec{H}'] da \end{aligned} \quad (2.21)$$

Rearranging terms,

$$\begin{aligned} \gamma - \gamma_0 &= \frac{\omega \int_S [(\epsilon - \epsilon_0) \vec{E}'^* \cdot \vec{E}' + (\mu - \mu_0) \vec{H}'^* \cdot \vec{H}'] da}{\int_S (\vec{E}'^* \times \vec{H}' - \vec{H}'^* \times \vec{E}') \cdot d\vec{a}} \\ &= \frac{\omega \int_S [(\epsilon - \epsilon_0) \vec{E}'^* \cdot \vec{E}' + (\mu - \mu_0) \vec{H}'^* \cdot \vec{H}'] da}{\int_S (\vec{E}'^* \times \vec{H}' + \vec{E}' \times \vec{H}'^*) \cdot d\vec{a}} \end{aligned} \quad (2.22)$$

Assuming non-magnetic materials such that $\mu = \mu_0$, equation (2.22)

becomes

$$\gamma - \gamma_0 = \frac{\omega \int_S (\epsilon - \epsilon_0) \vec{E}'^* \cdot \vec{E}' da}{\int_S (\vec{E}'^* \times \vec{H}' + \vec{E}' \times \vec{H}'^*) \cdot d\vec{a}} \quad (2.23)$$

So far, the only assumptions made are that the sample is uniform, homogeneous, non-magnetic and only the fundamental mode propagates. But if the disturbance caused by the sample slab is assumed to have but a small localized effect, with $\Delta S \ll S$ and if $\vec{H} = \vec{H}_0$ and $\vec{E} = \vec{E}_0$ outside the perturbing region, equation (2.23) becomes

$$\gamma - \gamma_0 = \frac{\omega \epsilon_0 (\epsilon_r - 1) \int_{\Delta S} \vec{E}'^* \cdot \vec{E}' da}{2 \int_S (\vec{E}'^* \times \vec{H}') \cdot d\vec{a}} \quad (2.24)$$

Since the average power flow, P , is equal to $\frac{1}{2} \int_S (\vec{E}' \times \vec{H}') \cdot d\vec{a}$, equation (2.24) becomes

$$\gamma - \gamma_0 = \frac{\omega \epsilon_0 (\epsilon_r - 1) \int_{\Delta S} \vec{E}'^* \cdot \vec{E}' da}{4P} \quad (2.25)$$

If ϵ is given by $\epsilon = \epsilon' - j\epsilon''$, γ in turn is complex given by $\gamma = \alpha - j\beta$. α is the attenuation constant in nepers per meter

and β is the phase constant in radians per meter in the MKS system.

Separating equation (2.25) into real and imaginary components

$$\beta - \beta_0 = \frac{\omega \epsilon_0 (\epsilon_r' - 1) \int_{as} (\vec{E}_0^* \cdot \vec{E}') da}{4P} \quad (2.26)$$

$$\alpha = \frac{\omega \epsilon_0 \epsilon_r'' \int_{as} (\vec{E}_0^* \cdot \vec{E}') da}{4P} \quad (2.27)$$

In general, the average power flow, P , is obtained from the real part of the integration of Poynting's vector, $\vec{E} \times \vec{H}^*$, over the waveguide cross-section. But

$$P = \frac{1}{2} \text{Re} \left\{ \int_S \vec{E} \times \vec{H}^* \cdot d\vec{a} \right\} = \frac{1}{2} \text{Re} \left\{ \int_S \vec{E}_t \times \vec{H}_t^* \cdot d\vec{a} \right\} \quad (2.28)$$

since the vector triple product involving the longitudinal components, $\vec{E}_1 \times \vec{H}^* \cdot d\vec{a}$, is zero. Here again, some errors are introduced by the existence of other than TE modes.

For an infinite waveguide, \vec{E}_t and \vec{H}_t are in time phase and orthogonal to each other, Z_0 may be used in the expression for power to eliminate either \vec{E}_t or \vec{H}_t . Thus

$$P = \frac{1}{2Z_0} \int_S |\vec{E}_t|^2 da \quad (2.29)$$

Since the mode filter of the sample mount will limit the propagation to the fundamental TE_{10} mode, one can write

$$\vec{E} = \vec{E}_0 = \vec{a}_y E_m \sin \frac{\pi x}{a} \quad (2.30)$$

where \vec{a}_y is the unit vector in the y-direction and E_m is

the maximum value of E field. Hence, for the TE_{10} mode, equation (2.29) becomes

$$P = \frac{E_m^2}{2 \epsilon_0} \int_0^b \int_0^a \sin^2 \frac{\pi x_1}{a} dx dy \quad (2.31)$$

where

$$z_0 = \sqrt{\frac{\mu_0}{\epsilon_0}} \frac{\lambda_{g0}}{\lambda}$$

If the thickness t is assumed to be small compared to the broad waveguide dimension a , the integral in equation (2.26) becomes

$$\int_{\Delta S} \vec{E}^* \cdot \vec{E} da = t E_m^2 \sin^2 \frac{\pi x_1}{a} = E_m^2 \sin^2 \frac{\pi x_1}{a} \Delta S \quad (2.32)$$

which when substituted into equation (2.26) and (2.27) yields

$$\begin{aligned} \beta &= \beta_0 + (\epsilon'_r - 1) \left(\omega \epsilon_0 \sqrt{\frac{\mu_0}{\epsilon_0}} \right) \frac{\lambda_{g0}}{\lambda} \sin^2 \frac{\pi x_1}{a} \left(\frac{\Delta S}{S} \right) \\ &= \beta_0 + 2\pi (\epsilon'_r - 1) \left(\frac{\Delta S}{S} \right) \frac{\lambda_{g0}}{\lambda} \sin^2 \frac{\pi x_1}{a} \end{aligned} \quad (2.33)$$

$$\alpha = 2\pi \epsilon'' \left(\frac{\Delta S}{S} \right) \frac{\lambda_{g0}}{\lambda} \sin^2 \frac{\pi x_1}{a} \quad (2.34)$$

Equations (2.33) and (2.34) are only approximate and subject to the assumptions made during the development of the perturbation theory. The solution is based on the assumptions that the energy in the waveguide is changed very little by the presence of the sample slab, that operation is in the fundamental mode, and that the sample is uniform in the z direction. The energy change referred

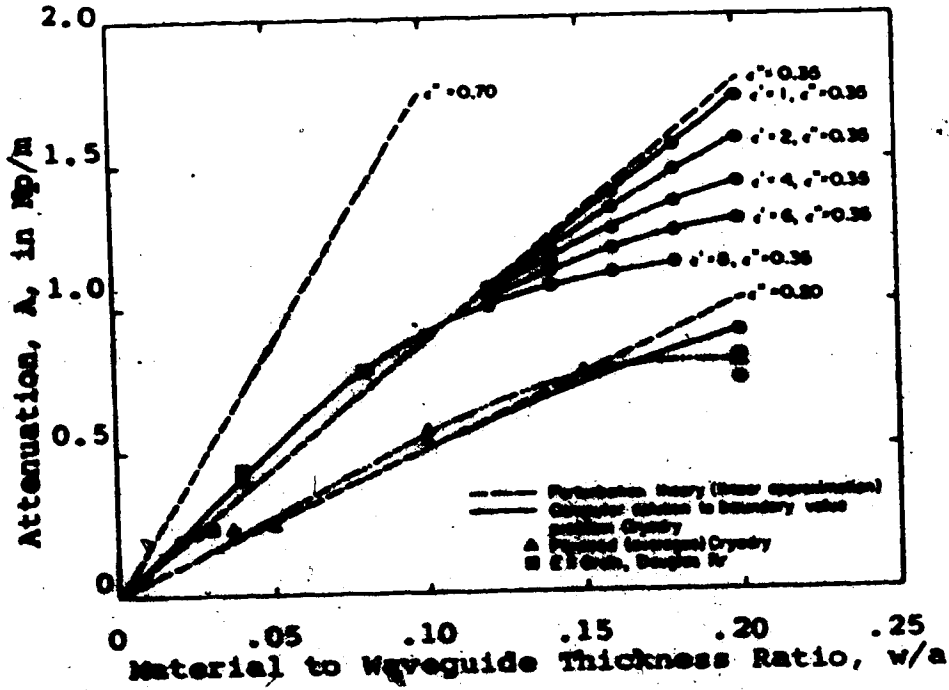


Fig. 2-2 Attenuation vs. filling factor (w/a) in 975 waveguide at $f = 915$ MHz (20).

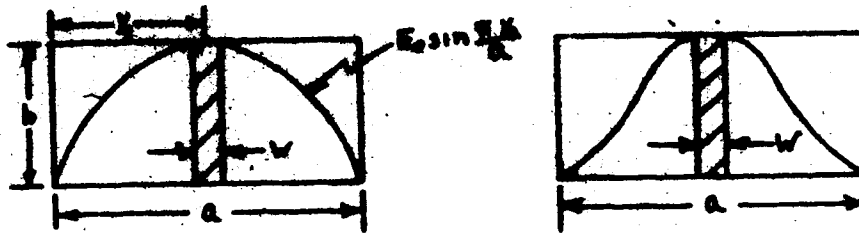


Fig. 2-3 Compression of E field into slab of high ϵ' in a waveguide (22).

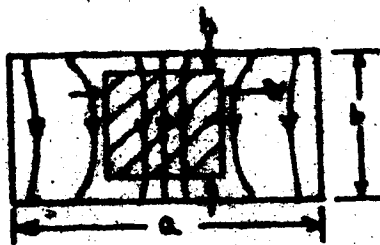


Fig. 2-4 Polarisation around sample with w comparable to h (23).

to is one of redistribution due to g' .

Moreover, Voss and Tinga (20) have shown the tendency of the waveguide to saturate for values of w/a greater than 0.1 as g' increases, see figure 2-2. This phenomenon has also been investigated by Foulds and Campaio (21). Figure 2-3 as obtained by Voss (22), shows how the field is compressed into regions of high g' . For higher g' , accuracy of the perturbation method can be improved by decreasing the width of the sample slab.

Another problem arises when the height of the sample h , is not substantially larger than the width, w , of the sample. Figure 2-4 shows how the electric field lines outside the sample are distorted when h is comparable to w . Tinga and Voss (20) suggest that a round tube placed perpendicular to the dominant mode of the electric field can be used as a sample holder for dielectric measurements using perturbation theory. However, that application does not account for the depolarization factor due to the geometry of the sample plus holder.

A tapered sample would cut down reflection from the front and the back of the sample slab. But the tapers can cause depolarization of the fields and hence introduce errors in the measurement. Therefore, rather than using tapers, a multiple reflection theory is developed to

account for reflection from the front and the back of the sample. Another disadvantage of a tapered sample is that the sample length has to be of the order of a wavelength or more which would make it more difficult to obtain temperature uniformity.

Because the materials being studied are available in powder form, a sample cell is needed. The width of the cell is made less than one-tenth of the width of the waveguide to satisfy one of the assumptions of perturbation theory. The height of the cell is made as tall as the narrow waveguide dimension to avoid the polarization effect referred to in figure 2-4. Sample length was chosen to give a measurable attenuation and phase shift and yet was kept short enough to minimize temperature variations. The side walls of the cell were ground very thin, about 0.02 inch, to minimize dielectric loading on the sample. To withstand high temperature, the cell is made of quartz. Furthermore, quartz has a well defined dielectric properties over a wide temperature range (24). Figure 2-5 show the dimensions of the quartz cell.

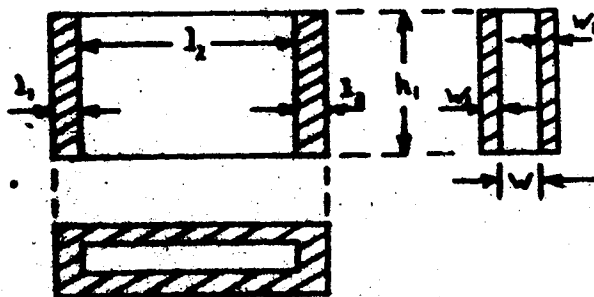


Fig. 2-5 Construction of quartz sample cell.

C. Theory of Reflection from a Multiple Interface

Consider propagation of a guided electromagnetic wave incident normally on three layers of dielectrics as shown in figure 2-6, combining the procedures of Tinga et al(25) and Stratton(26). Expressions for the total wave amplitude with due regard for phase are designated by A through P. Going from one medium say a, to another medium, say b, gives rise to interface reflection and transmission for which the definitions are

$$\Gamma_{ab} = -\Gamma_{ba} = \frac{Z_b - Z_a}{Z_b + Z_a} \quad (2.35)$$

$$t_{ab} = 1 + \Gamma_{ab} \quad (2.36)$$

where Γ denotes the reflection coefficient, t , is the transmission coefficient, Z_a and Z_b are impedances of medium a and b respectively as shown in figure 2-7. The sign of Γ depends on whether the direction of the incident signal is from a to b or from b to a.

Writing down the expression for quantities A through P in terms of the interface reflection coefficients and the propagation constants, one gets, referring to Figure 2-6,

$$A = 1 \quad (2.37a)$$

$$B = \Gamma_{21} A + (1 - \Gamma_{21}) D \quad (2.37b)$$

$$C = (1 + \Gamma_{21}) A - \Gamma_{21} D \quad (2.37c)$$

$$D = F e^{-j\beta_1 l} \quad (2.37d)$$

$$E = C e^{-j\beta_1 l} \quad (2.37e)$$

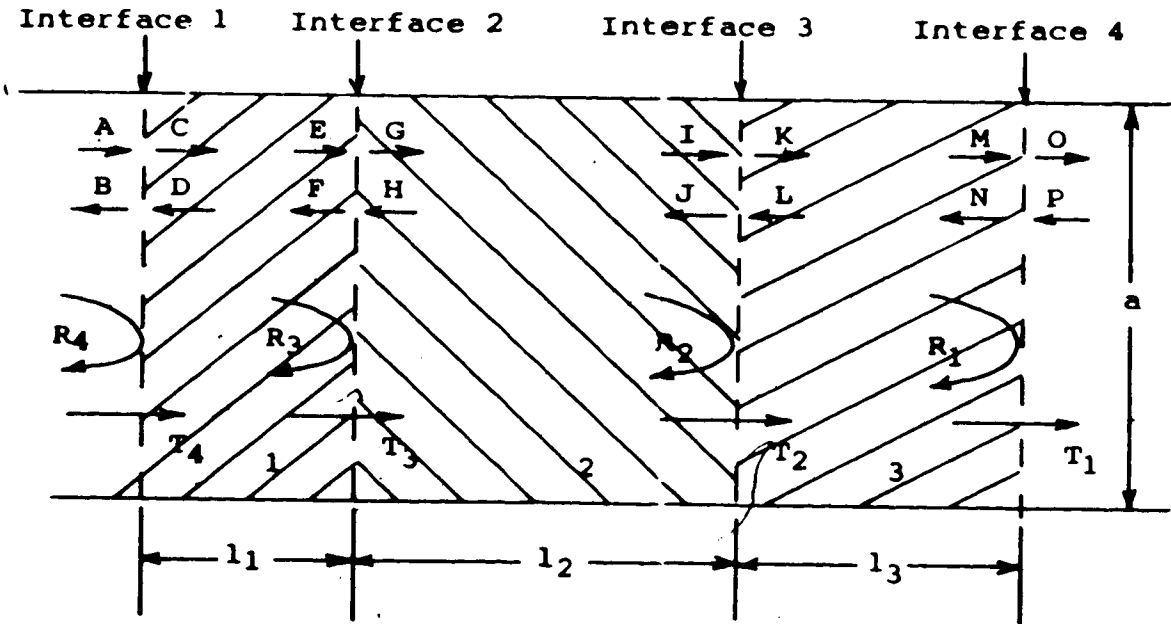


Fig. 2-6 Multiple reflections of three layers of dielectric in a rectangular waveguide, top view.

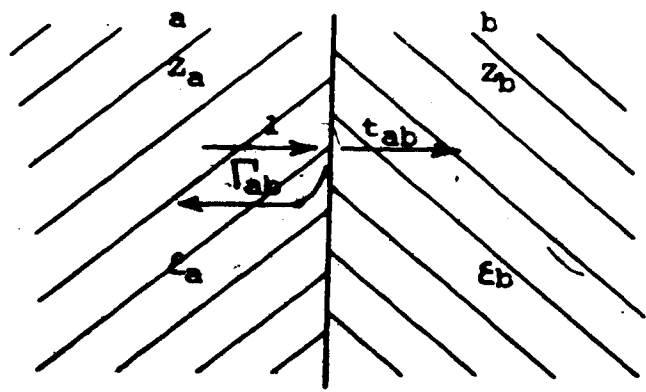


Fig. 2-7 Reflection from an interface of two dielectrics.

$$F = \Gamma_{qs} E + (1 - \Gamma_{qs}) H \quad (2.37f)$$

$$G = (1 + \Gamma_{qs}) E - \Gamma_{qs} H \quad (2.37g)$$

$$H = J e^{-j\gamma_2 l_2} \quad (2.37h)$$

$$I = G e^{-j\gamma_2 l_2} \quad (2.37i)$$

$$J = \Gamma_{sq} I + (1 - \Gamma_{sq}) L \quad (2.37j)$$

$$K = (1 + \Gamma_{sq}) I - \Gamma_{sq} L \quad (2.37k)$$

$$L = N e^{-j\gamma_3 l_3} \quad (2.37l)$$

$$M = K e^{-j\gamma_3 l_3} \quad (2.37m)$$

$$N = \Gamma_{qa} M + (1 - \Gamma_{qa}) P \quad (2.37n)$$

$$O = (1 + \Gamma_{qa}) M - \Gamma_{qa} P \quad (2.37o)$$

$$P = X O e^{-2j\gamma_4 l_4} \quad (2.37p)$$

where Γ_{qs} , Γ_{qa} , Γ_{sq} , and Γ_{aq} are reflections from quartz sample interface, quartz air interface, sample quartz interface, and air quartz interface respectively; X is the total reflection at the termination, and γ_1 and l_1 , γ_2 and l_2 , and γ_3 and l_3 are the complex propagation constant and the layer thickness for layer 1, 2, and 3 respectively, and l_4 is the distance from the last quartz air interface to the load. For a well matched generator and load,

$$X = 0 \quad (2.38a)$$

$$P = 0 \quad (2.38b)$$

Hence

$$N = \Gamma_{qa} M \quad (2.38c)$$

$$O = (1 + \Gamma_{qa}) M \quad (2.38d)$$

Designate R_1 , R_2 , R_3 and R_4 to be the ratio N/M , J/I , F/E and P/A respectively. Also designate T_1 , T_2 , T_3 and T_4 to be the ratio O/M , K/I , G/E and C/A respectively as shown in

figure 2-6. Solving for R_1 , we get

$$R_1 = N/M = \Gamma_{qa} \quad (2.39)$$

Thus R_1 is the normalized total return in medium 3 from interface 4. When equations (2.37J), (2.37K) and (2.37L) are solved for J/I , we get

$$R_2 = J/I = \frac{\Gamma_{q1} + \Gamma_{q0} e^{-2j\gamma_3 l_3}}{1 + \Gamma_{s1} \Gamma_{qa} e^{-2j\gamma_3 l_3}} = \frac{\Gamma_{s1} + R_1 e^{-2j\gamma_3 l_3}}{1 + \Gamma_{s1} R_1 e^{-2j\gamma_3 l_3}} \quad (2.40)$$

Similarly,

$$R_3 = F/E = \frac{\Gamma_{qs} + R_2 e^{-2j\gamma_2 l_2}}{1 + \Gamma_{qs} R_2 e^{-2j\gamma_2 l_2}} \quad (2.41)$$

$$R_4 = B/A = \frac{\Gamma_{s1} + R_3 e^{-2j\gamma_1 l_1}}{1 + \Gamma_{s1} R_3 e^{-2j\gamma_1 l_1}} \quad (2.42)$$

Here R_4 is the total reflection of the system. T_1 , T_2 , T_3 and T_4 can be solved using similar methods.

$$T_1 = O/M = 1 + \Gamma_{qa} \quad (2.43)$$

$$T_2 = K/I = \frac{1 + \Gamma_{s1}}{1 + \Gamma_{s1} R_1 e^{-2j\gamma_3 l_3}} \quad (2.44)$$

$$T_3 = G/E = \frac{1 + \Gamma_{qs}}{1 + \Gamma_{qs} R_2 e^{-2j\gamma_2 l_2}} \quad (2.45)$$

$$T_4 = C/A = \frac{1 + \Gamma_{s1}}{1 + \Gamma_{s1} R_3 e^{-2j\gamma_1 l_1}} \quad (2.46)$$

When incident signal goes through interfaces 1, 2, 3 and 4 as shown in figure 2-6, the transmission coefficients are T_1 , T_2 , T_3 and T_4 respectively. Similarly, incident signal through dielectric layers 1, 2 and 3 undergoes a phase and an amplitude change of $e^{-j\gamma_1 l_1}$, $e^{-j\gamma_2 l_2}$, and $e^{-j\gamma_3 l_3}$ respectively. Thus the total transmission T_T of the three layers of dielectric is given by

$$T_T \text{ o/a} = T_1 T_2 T_3 T_4 e^{-j(\gamma_1 l_1 + \gamma_2 l_2 + \gamma_3 l_3)} \quad (2.47)$$

The apparent attenuation of the incident signal, given by equation (2.47) is the total power loss in the dielectrics plus the total reflection, R_4 , from the sample.

D. Iteration Technique used

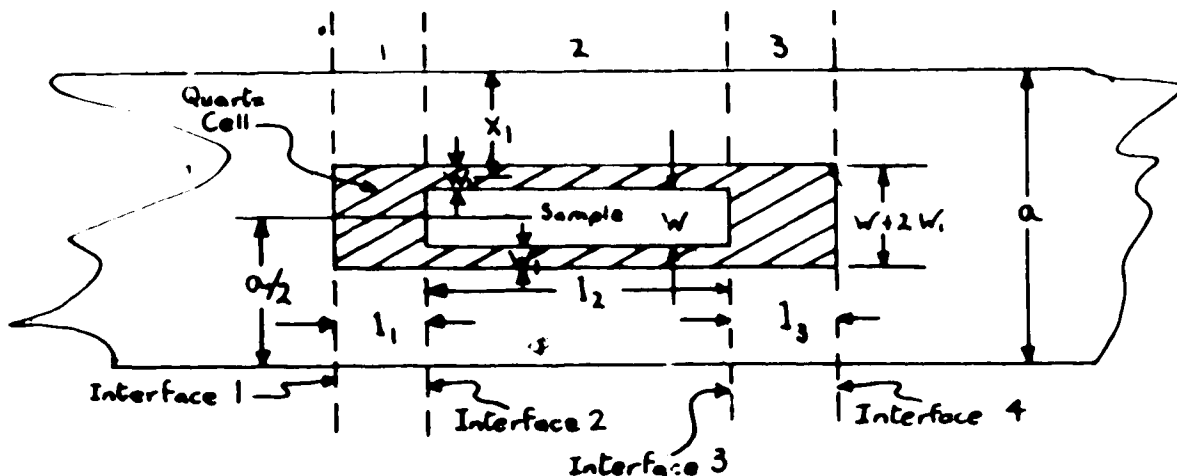


Fig. 2-8 Top view of sample mount and sample cell.

Consider figure 2-8 above showing the top view of the sample mount with a sample cell in it. The propagation constant γ of each of the three sections (sections 1, 2 and 3 as shown on figure 2-8) can be calculated using perturbation formulas (2.33), (2.34) and the complex dielectric constant for the particular material. For sections 1 and 3, the propagation constants γ_1 and γ_3 were calculated using the width of each section, $w + 2w_1$, and the complex dielectric constant for quartz ϵ_a^a . Thus

$$\gamma_1 = \gamma_3 = \beta_1 - j\alpha_1 \quad (2.48)$$

$$\begin{aligned} \gamma_2 &= -j \left[2\pi \epsilon_q'' \left(\frac{4S}{S} \right) \frac{\lambda_0}{\lambda_1} \sin^2 \frac{\pi x}{2} \right] + \left[\beta_0 + 2\pi (\epsilon_q' - 1) \left(\frac{4S}{S} \right) \frac{\lambda_0}{\lambda_1} \sin^2 \frac{\pi x}{2} \right] \\ &= \beta_0 + 2\pi \left(\frac{4S}{S} \right) \frac{\lambda_0}{\lambda_1} \sin^2 \frac{\pi x}{2} \left[(\epsilon_q' - 1) - j \epsilon_q'' \right] \quad (2.49) \end{aligned}$$

where β_0 is the phase constant of an empty waveguide in radians per meter given by,

$$\beta_0 = \frac{2\pi f \sqrt{1 - (f_c/f)^2}}{C} \quad (2.50)$$

where $f_c = 2.078 \times 10^9$ Hz, is the cut-off frequency for an S-band waveguide and $C = 2.997925 \times 10^8$ m/sec, is the speed of light in air. Since the quartz in sections 1 and 3 are centrally located in the sample mount, $\sin^2 \frac{\pi x}{a} = 1$, and γ_1 and γ_3 are reduced to,

$$\gamma_1 = \gamma_3 = \beta_0 + 2\pi \left(\frac{\Delta S_1}{S}\right) \frac{\lambda_0}{\lambda^2} [(\epsilon'_a - 1) - j\epsilon''_a] \quad (2.51)$$

For section 2, the propagation constant γ_2 is the sum^e of the propagation constants of the sample slab, γ_s , and those of the two quartz side walls $2\gamma_{w1}$. Since the perturbation relations are linear in γ .

Since the dielectric loss of quartz is very small ($\epsilon''_Q = .0002268$) and the quartz cell side walls are very thin ($w_1 = .02''$) compared to the sample thickness ($w = .157''$), the loss due to them are ignored. Thus,

$$\gamma_{w1} = \beta_{w1} = \beta_0 + 2\pi (\epsilon'_a - 1) \left(\frac{\Delta S_2}{S}\right) \frac{\lambda_0}{\lambda^2} \sin^2 \pi \left(\frac{a-w-w_1}{2a}\right) \quad (2.52)$$

and

$$\begin{aligned} \gamma_2 &= 2\beta_{w1} + 2\pi (\epsilon'_s - 1) \left(\frac{\Delta S_3}{S}\right) \frac{\lambda_0}{\lambda^2} \sin^2 \frac{\pi x}{a} - j[2\pi \epsilon''_s \left(\frac{\Delta S_3}{S}\right) \frac{\lambda_0}{\lambda^2} \sin^2 \frac{\pi x}{a}] \\ &= 2\beta_{w1} + 2\pi \left(\frac{\Delta S_3}{S}\right) \frac{\lambda_0}{\lambda^2} \sin^2 \frac{\pi x}{a} [(\epsilon'_s - 1) - j\epsilon''_s] \end{aligned} \quad (2.53)$$

$$\gamma_2 = 2\beta_{w1} + 2\pi \left(\frac{\Delta S_3}{S}\right) \frac{\lambda_0}{\lambda^2} [(\epsilon'_s - 1) - j\epsilon''_s] \quad (2.54)$$

since the sample slab is centrally located. In equations (2.51), (2.52) and (2.54) above, ΔS_1 , ΔS_2 and ΔS_3 are the cross-sectional areas for quartz slabs in sections 1 and 3,

quartz cell side walls in section 2, and sample slab in section 2 respectively.

Using the calculated propagation constants $\gamma_1 = \gamma_3$ and γ_2 , the impedances for each section, $Z_1 = Z_3$ and Z_2 for guided TE waves were then obtained using the relation

$$Z_{iTE} = j \frac{\omega \mu}{\gamma_i} \quad (2.55)$$

given in Ramo, Whinnery and Van Duzer (23). The reflection and transmission coefficients Γ_i and t_i for each interface were obtained using formulas (2.35) and (2.36). Following the multiple reflection theory developed in section C of this chapter, the total transmission coefficient, T_s , through the three sections of the sample mount (see figure 2-6) can then be calculated for different sample materials in the quartz cell.

The first step in the iteration method (see appendix B) is to input all constants necessary for the calculation leading to the total transmission, T_s . These constants include dimensions of the quartz cell l_1 , l_2 , l_3 , w , w_1 and h_1 in meters, inside cross-sectional dimensions of an S-band waveguide a and b , sample height h , measured change of phase and attenuation, $\Delta\phi$ and $\Delta\alpha$, in radians/m and nepers/m respectively due to the introduction of the sample, the frequency, f , used in hertz and the complex dielectric

constant of fused quartz, ϵ_0 .

Then an estimation of the complex dielectric constant, ϵ_s , for the sample material tested is assumed. For cupric oxide, the value used for the first approximation was taken from the results of the experiments at room temperature by Tinga and Ford(4).

Using all these constants, the total transmission T_{air} is first calculated using air as the sample material with $\epsilon_{air} = 1 - j0$. Then the total transmission for a particular sample T_s is calculated using the estimated complex dielectric constant for the sample ϵ_s . Both T_s and T_{air} are complex giving amplitude and phase information. The normalized total power transmission for these two cases are given by,

$$P_{T_s} = T_s \times T_s^* \quad (2.56)$$

$$P_{air} = T_{air} \times T_{air}^* \quad (2.57)$$

where T_s^* and T_{air}^* are the complex conjugates of T_s and T_{air} respectively. The attenuation α_{cal} in nepers, and phase shift ϕ_{cal} in radians caused by the introduction of the sample are then calculated using the equations below.

$$\alpha_{cal} = 10 \log_{10} (P_{T_s} / P_{air}) \quad (2.58)$$

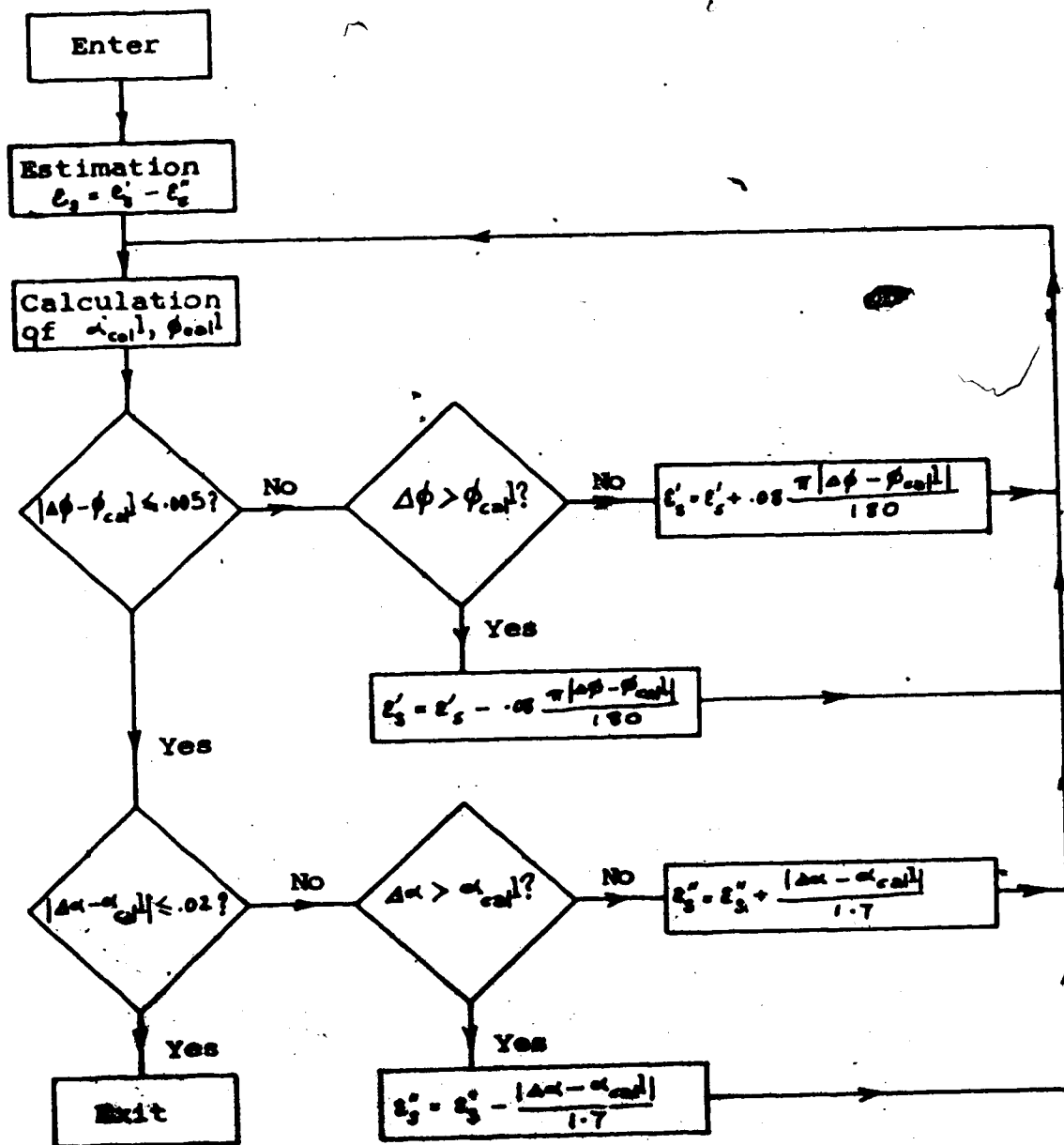
$$\phi_{cal} = \angle T_s - \angle T_{air} \quad (2.59)$$

where $\angle T_s$ and $\angle T_{air}$ are arguments of the complex quantities T_s and T_{air} respectively. α_{cal} and ϕ_{cal} are then compared

with the measured phase shift, $\Delta\phi$, and attenuation, $\Delta\alpha$, due to the introduction of sample in the quartz cell. If, ϕ_{cal} is smaller than $\Delta\phi$, the estimated real part of complex dielectric constant, ϵ_s' , is increased, or the estimated value ϵ_s' is decreased if ϕ_{cal} is larger than $\Delta\phi$ and another iteration is made. The iteration process continues until ϕ_{cal} and $\Delta\phi$ are within $\pm 1^\circ$ phase change which is the accuracy of the phase shifter used.

Similarly, α_{cal} and $\Delta\alpha$ are compared and the imaginary part of the complex dielectric constant, ϵ_s'' , is changed until the difference in α_{cal} and $\Delta\alpha$ is within the accuracy of the attenuator used which is 0.04 db. On every iteration, ϕ_{cal} and $\Delta\phi$ are compared again to see if the difference is still within $\pm 1^\circ$.

The final value of $\epsilon_s = \epsilon_s' - j\epsilon_s''$ is then the complex dielectric constant of the sample at one particular temperature. Figure 2-9 shows the flow diagram for the iteration method used.



ϕ_{cal} = calculated phase change due to introduction of sample.
 α_{cal} = calculated attenuation due to introduction of sample.
 $\Delta\phi$ = measured phase change due to the introduction of sample.
 $\Delta\alpha$ = measured attenuation change due to introduction of sample.
 ϵ_s = estimated complex dielectric constant of sample.
 ϵ'_s = real part of ϵ_s .
 ϵ''_s = imaginary part of ϵ_s .

Fig. 2-9 Flow diagram of iteration method used.

E. Higher mode Interference

In the paper by Hord and Rosenbaum(17) , an algebraic procedure is described which yields approximate values for the "cut-off" frequencies and propagation constants of dielectric loaded waveguide, the first order approximation for the normalized propagation constant β_a in radians results in more than -20% error compared to the exact solution for the normalized dielectric of thickness $w/a = 0.1$ and $\epsilon_r \approx 10$ (see figures 2-10, 2-11 and 2-12).

A better approximation is obtain by including coupling to the next higher order mode with the closest cut-off frequency, which is the TE₂₀ modes. Figures 2-11 and 2-12 show that errors for the propagation constant, β_a , are now reduced to less than -10%. It should be noted that parameter values of $\epsilon_r = 16$ and $w/a = .2$ for figures 2-11 and 2-12 respectively were chosen to given a worst possible case for the perturbation method used^c.

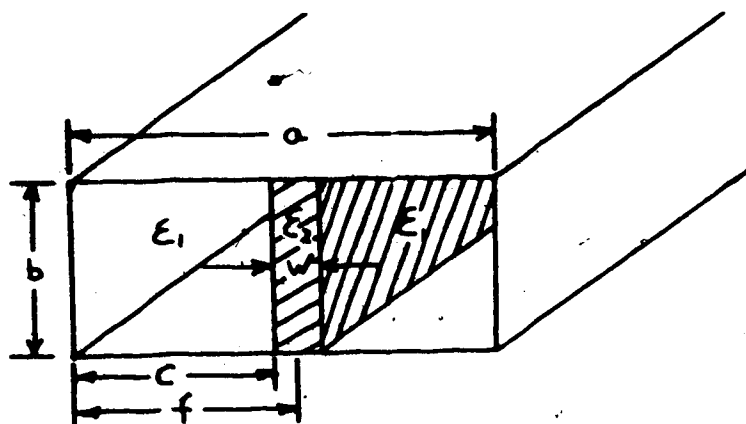


Fig. 2-10 Symmetrically loaded waveguide.

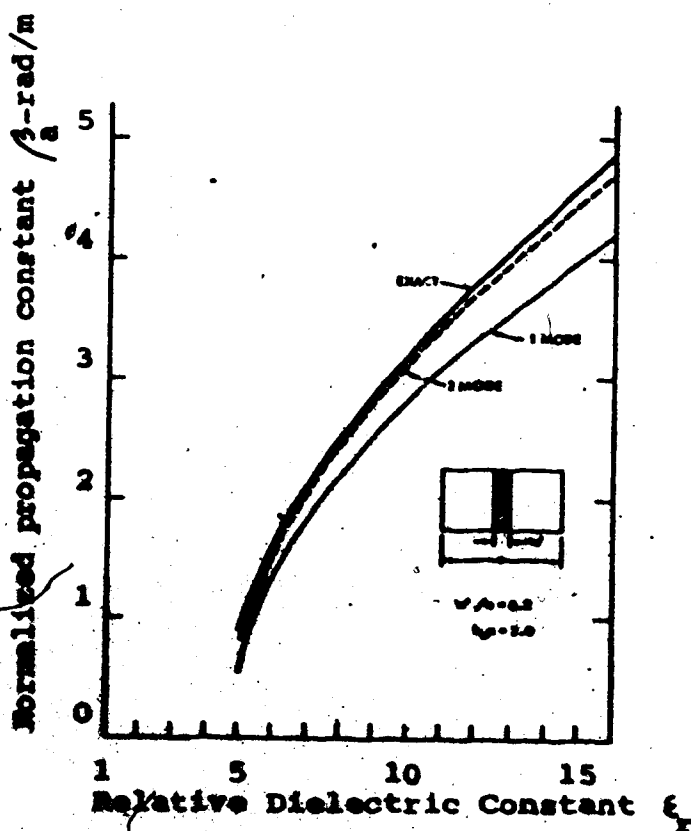


Fig. 2-11 Comparison of approximate propagation constant with exact solution as a function of relative dielectric constant (17).

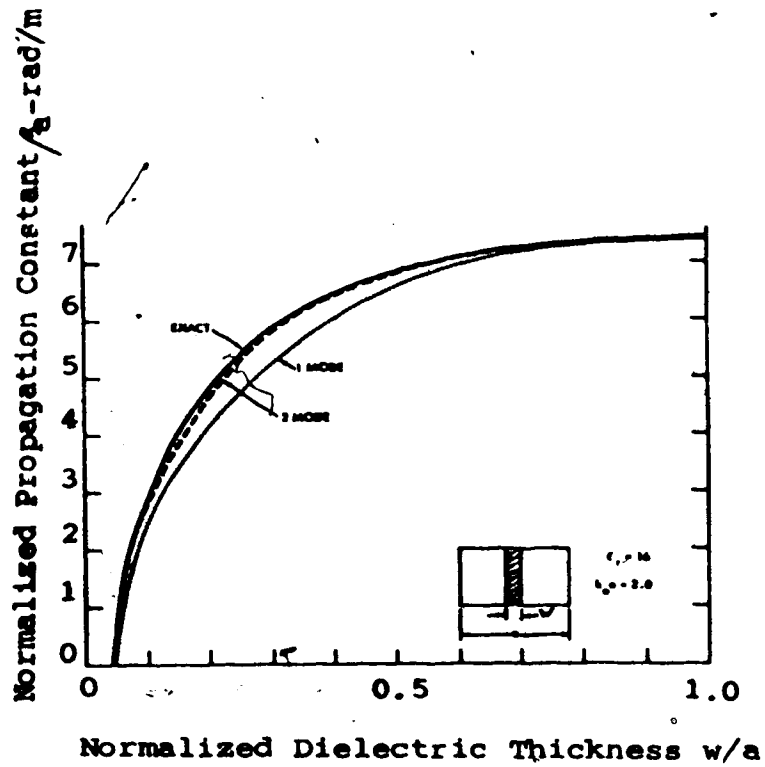


Fig. 2-12 Comparison of approximate propagation constants with exact solution as a function of dielectric thickness (17).

For the case under investigation, TE_{20} and TE_{01} modes couple most strongly to the fundamental mode and by accounting for them, results close to the exact solution will be obtained. By suppressing the two higher modes, accuracy of the measurement for the propagation constant will improve considerably. Figure 2-13 gives the wall currents for rectangular waveguide for the TE_{10} , TE_{20} and TE_{01} modes. By cutting two slots along the center of both broad waveguide walls as shown will not impede the propagation of the fundamental mode. But it will completely cut off the propagation of the TE_{01} mode and partially impede the propagation of the TE_{20} mode thus improving the measurement accuracy. Contribution from evanescent modes is already accounted for in the two modes approximation.

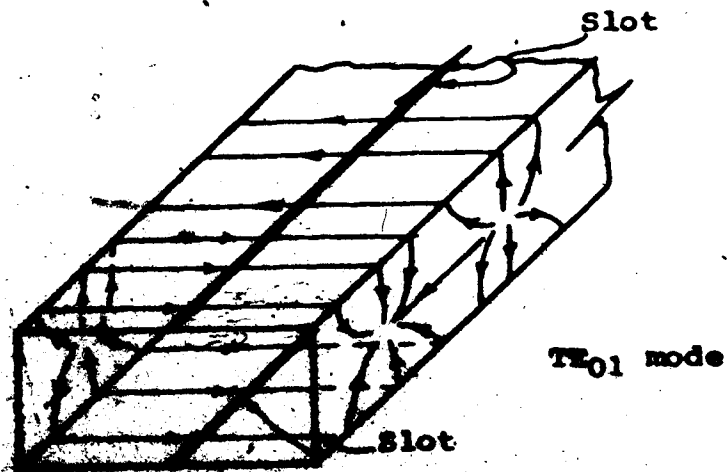
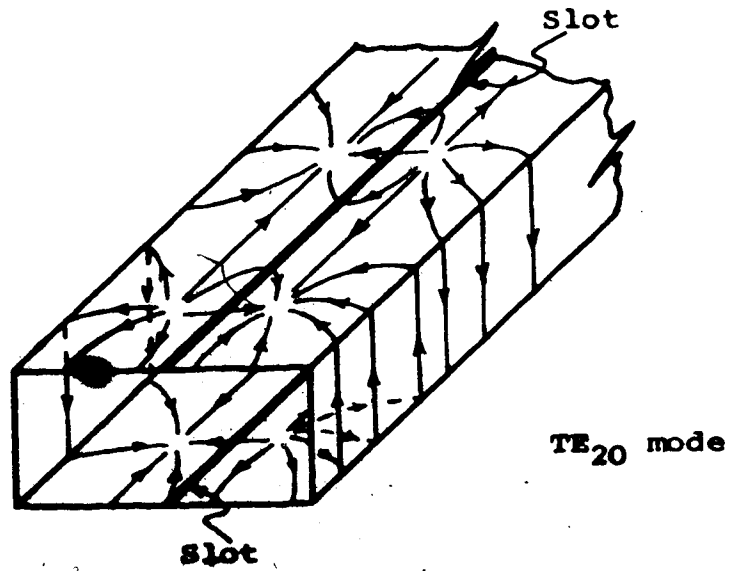
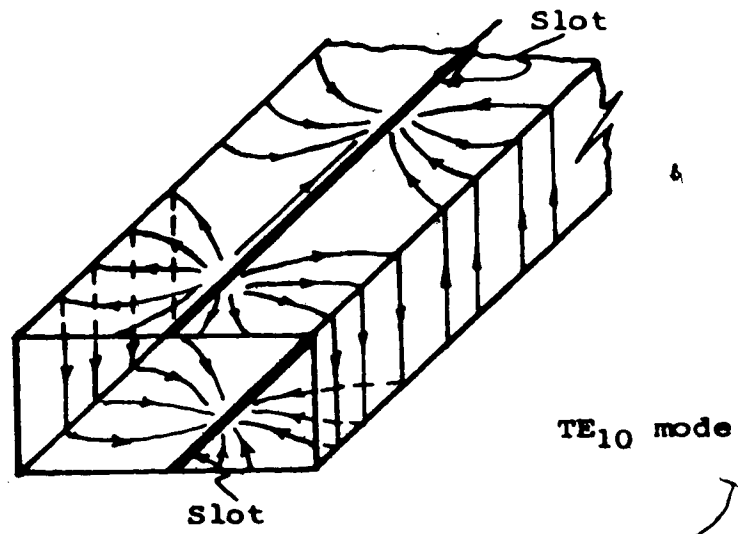


Fig. 2-13 Wave filter construction and wall current for TE₁₀, TE₂₀, TE₀₁ modes.

List of Footnotes

^a $\epsilon_0 = 3.78 - j0.0002258(3)$.

^bWR-284 waveguide was used in this work.

^cFor our measurement, $w/a < 0.1$ and $\epsilon_r' < 10$.

CHAPTER 3

EXPERIMENTAL METHODS

A. Introduction

Having developed an analytical model for finding the complex dielectric constant of thin samples in a waveguide, experimental data on the propagation constant is obtained by using a microwave bridge. The validity of the iteration method used is tested using samples with known complex dielectric constants and comparing results obtained by the use of two different sample cells for the same dielectric material. Details of the bridge construction, the heating method, the measurement procedure, and the calibration procedure are outlined in the following sections.

B. Experimental set-up

1. Precision bridge circuit

A block diagram of the experimental apparatus is given in figure 3-1. Low power (~10mw) microwaves at 245 GHz are generated by the signal generator. The signal is passed through an isolator, a coaxial to waveguide adapter and tuner (3) before it is split into the two arms of the microwave bridge via a 10 db directional coupler (6). In the reference arm, the signal passes through a waveguide tuner (5), a waveguide to coaxial adapter, a precision phase shifter^b, another waveguide tuner (7) and a precision attenuator^c. In

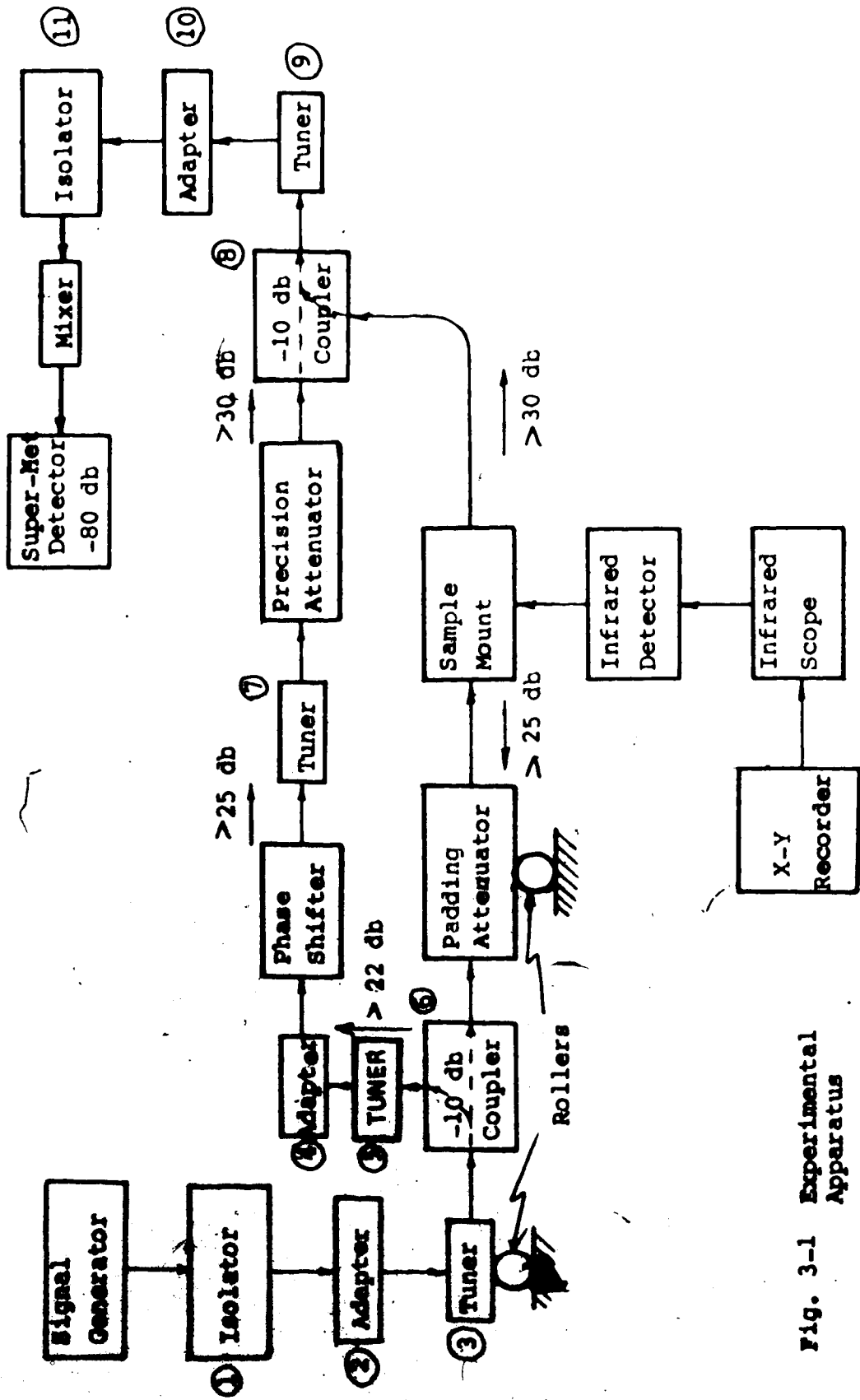


Fig. 3-1 Experimental Apparatus

the sample mount arm, the signal passes through a padding attenuator (Microlab S155A 0-20 db) and through the sample mount. Signals in the two arms are recombined through a second 10 db directional coupler (8) (HP-S752C). The combined signal passes through tuner (9) a waveguide, to coaxial adapter (10), and a coaxial isolator (11) before it is detected by a crystal mixer and the output fed to a sensitive (-80 dbm) super-heterodyne microwave receiver^d.

Both the precision attenuator and the precision phase-shifter are adjusted to obtain a deep null on the detector indicating a balanced condition. Care was taken to ensure that both arms of the bridge were properly matched. Using a swept frequency reflectometer the whole system was matched for a return loss of twenty-two decibels ± 2 decibels (VSWR ≤ 1.174). The sample arm is also matched looking towards the signal generator by adjusting tuner (3) so that reflections from the sample and quartz cell will not be reflected back again. The whole structure of waveguide and other components in front of the sample mount is put on rollers so that the sample mount can expand smoothly when heated. The expansion of the sample mount arm of the bridge at 900°C is about three millimeter. If rollers are not used, thermal expansion will cause the waveguide to push against the table on which it rests and cause erratic phase changes.

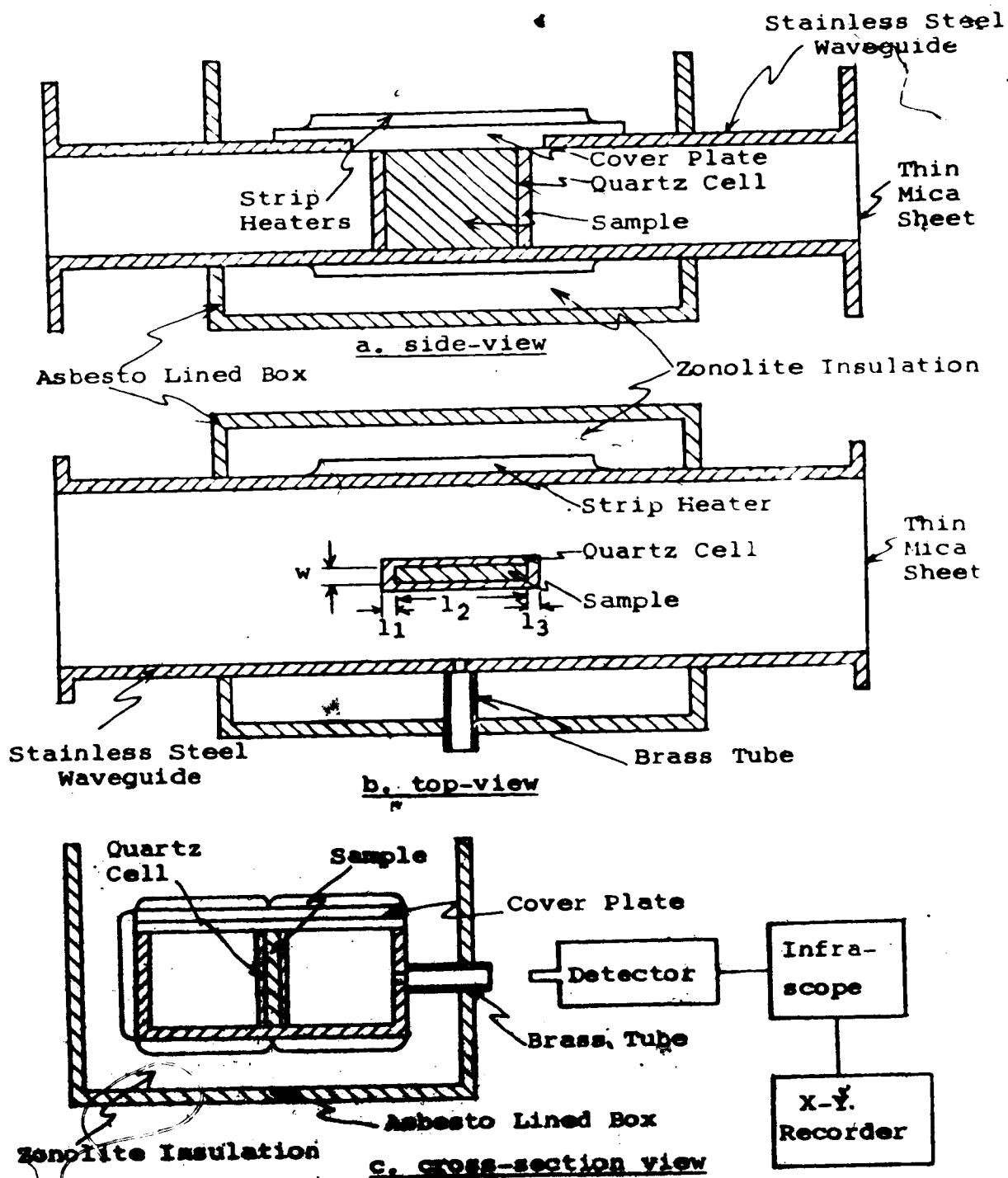


Fig. 3-2 Sample mount construction detail.

2. Sample mount design

The design of the sample mount deserves special consideration. Figure 3-2 shows construction of the sample mount. Since the maximum temperature which each strip heater (Chromolox PT-603, 300 watts) can reach in open air is around 700°C, an insulating box is built around the sample mount to insulate against heat loss. The box is made of plywood lined with asbestos sheet. Zonolite is used to fill the space between the box and the stainless steel guide. Using the insulating box, temperature of the waveguide mount can reach 1000°C. Further convective heat loss within the waveguide is prevented by covering each end of the stainless steel guide by a thin mica sheet. The two mica sheets cause only very small microwave reflections (VSWR \cong 1.005) yet they prevent convective heat loss from the sample cell to the rest of the waveguide system.

The waveguide mount itself is made of stainless steel to withstand high temperature°. As shown in figure 3-2, a removable cover plate is placed on the top of the waveguide mount so that the sample cell and sample can be placed in the sample mount more easily. Two holes (0.127" diameter) were drilled on the two narrow walls of the guide, one for temperature monitoring of the sample by the infrared detector and the other to allow a thermocouple to pass through for temperature monitoring purposes which will be explained in more detail in the following section. Reflections due to these small holes are negligible (VSWR \cong 1.004).

3. Temperature control and detection

High temperature dielectric measurements are problematic with respect to controlling and maintaining sample temperature at a desired high temperature level. To achieve controllable heating of samples, five high-heat-density electrical strip heaters are used as shown in figure 3-2c. The five heaters are parallel connected. Voltage supply to the heaters is controlled by a 10 amp variac (General Radio W10MT3). Temperature of the sample mount can be varied from room temperature up to 1000°C by varying the supply voltage. Heater voltage is varied in five-volt steps. Each voltage level is maintained for at least 20 minutes to allow the sample temperature to reach a steady state value.

Infrared temperature detection is used by focusing an infrared camera on the sample through the hole in the narrow waveguide wall. The infrascopes used (Huggins lab. 31L00-02) is factory calibrated up to 300°C. To increase the temperature detection range up to about 1000°C, a metal lens with a very small hole (.127" diameter) was made to cut down the infrared radiation reaching the detector at high temperature. The metal lens can be fitted inside the lens barrel of the infrared camera as shown in figure 3-4. Output of the indicator was recorded on an X-Y recorder. The procedure for calibrating the X-Y recorder output directly in terms of temperature will be outlined in the next section.

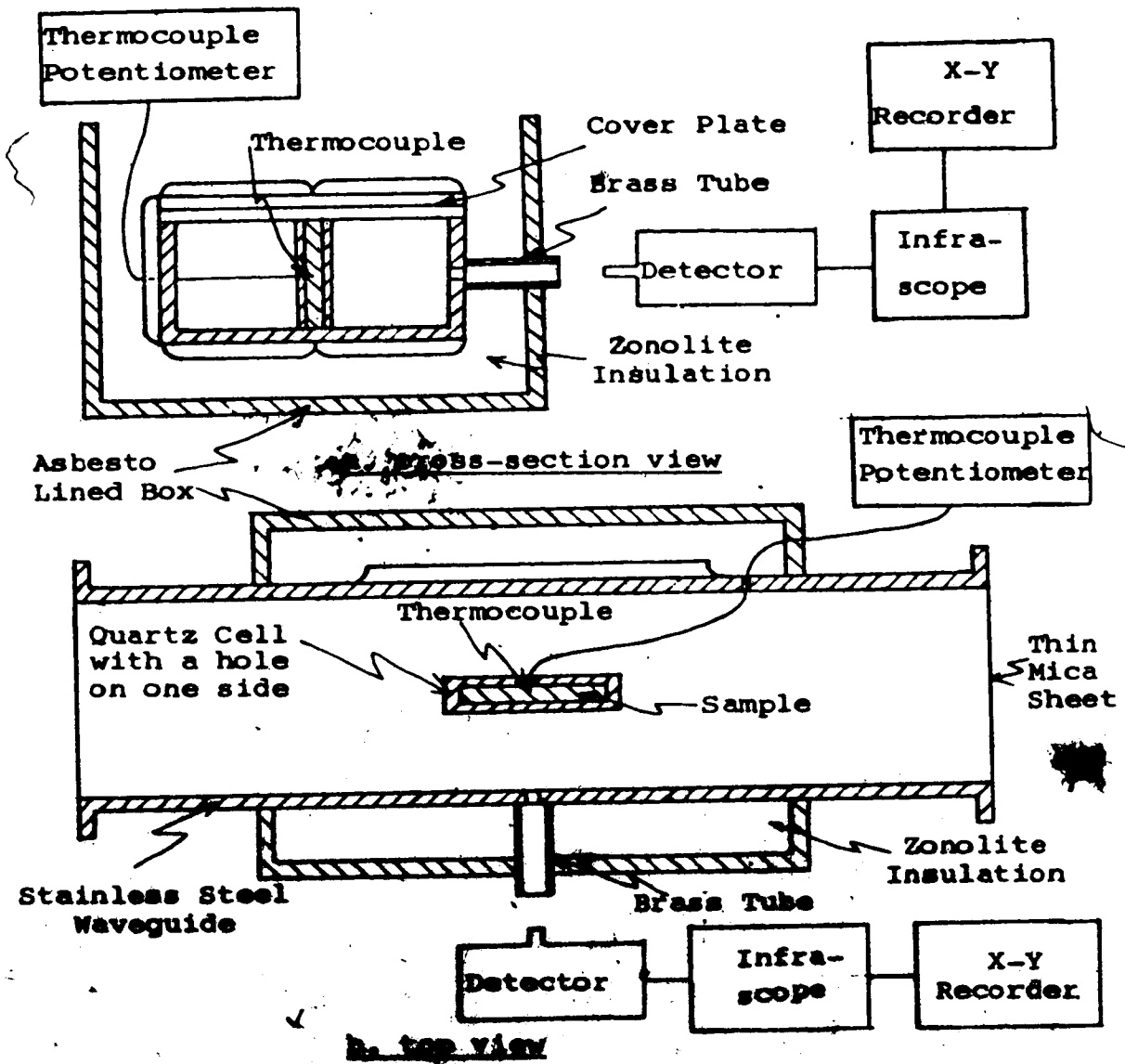


Fig. 3-3 Sample temperature calibration set-up

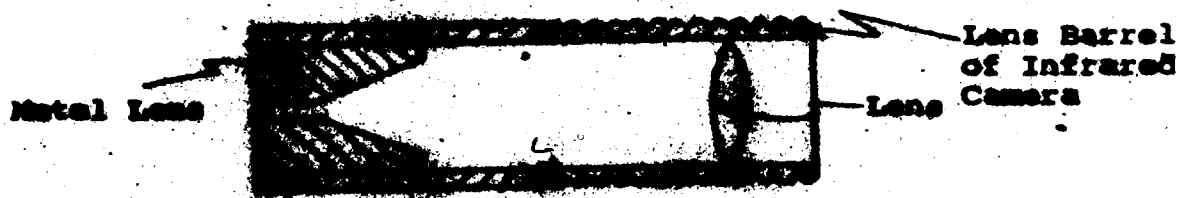


Fig. 3-4 Metal lens and lens barrel of infrared camera detail

C. Calibration

1. Calibration of sample temperature

Output of the X-Y recorder was calibrated in degrees Celsius, via the use of a chromel-alumel thermocouple. This also eliminates error due to the varying emissivity of the sample and obviates the need to know an absolute value of the emissivity. The temperature calibration set-up is shown in figure 3-3. A thermocouple is inserted into the sample under calibration through holes in the narrow waveguide wall and the quartz cell. The infrared camera is focused on the sample on the opposite side of the thermocouple. The reading on the X-Y recorder will then correspond to the temperature indicated on a thermocouple potentiometer. By increasing the heater voltage five volts every 20 minutes, temperature can be recorded in 10°C steps to 900°C using the marker on the recorder via a foot switch connected to the X-Y recorder. The temperature is first calibrated up to 300°C with the metal lens off. Then the metal lens is put on for calibration of higher temperatures. The recording made is then the calibrated temperature scale for that particular material. Before measurement of another sample material type is made, temperature has to be recalibrated since different materials have different emissivities.

2. Sample calibration

Calibration of the glass holder, designed by Tingo (27), is accomplished by inserting the calibration thermocouple sections, one

at a time and then both of them in series, in the sample mount ⁴⁸
arm of the bridge. The length of each precision waveguide,
when converted to phase angle for the frequency 2.45 GHz, can
then be compared to the change of phase recorded on the phase
shifter. The calibration shows that for the two precision
guides⁹ at 6.00 inches and 5.50 inches long and the combined
length of 11.50 inches, equivalent to 237.62 degree, 217.818
degree and 95.438 degree respectively, the measured phase
shift recorded on the phase shifter was 238.2 degree, 218.3
degree and 96.01 degree respectively, thus indicating errors
of 0.025%, 0.22% and 0.572% respectively.

3. Calibration of the microwave bridge using samples with known complex dielectric constants and comparing results of calculations of two sample cells on the same sample.

Before the measurements of different metal oxides and sulfides as a function of temperature are made, a calibration using samples with known complex dielectric constants must be made in order to quantify the microwave bridge accuracy for such measurements as well as the accuracy of the analytical measurements for the substances. Liquids and powder samples were chosen for this purpose. Samples of known loss tangent ranging from 0.2 to 1.5 were chosen since the permittivity and loss tangent of materials under test were thought to be in this range. The samples were selected to cover the range of the complex dielectric constants. The dielectric

tric constants for different kinds of materials were calculated and compared with the values given in the literature.

Since frequencies used by von Hippel and other authors were not 2.45 GHz, their results were interpolated to 2.45 GHz but even so, they can only be used as guides. The inaccuracy (that is, the deviation from the true value) is extremely difficult to estimate since the range of variation of literature values of several substances is surprisingly wide. Measured values of some so-called "standard" substances and literature data for them are given in Chapter four Table 4-1.

The effects of cell's size differences on the measurement results were checked using cupric oxide sample. The dimensions for the two cells used were 0.148 inches by 0.826 inches by 1.27 inches, and 0.096 inches by 0.698 inches by 1.318 inches respectively. The measurement results thus obtained for the compound indicate differences of one percent for the dielectric constant ϵ' , and two percent for the loss factor ϵ'' .

D. Measurement procedure

Before the actual measurement is made, care must be taken to minimize and control the moisture content in the sample since the value of the complex dielectric constant is very much dependent on moisture content. Furthermore, it is important to note that in order to get a minimum moisture content in a sample, a fairly long conditioning period is necessary, since diffusion of moisture between the sample's interior and a controlled atmosphere is a slow process. To accomplish this, samples are oven-dried for 24 hours at 105°C in a Delta Design MK 6300 temperature chamber, then placed in a dessicator to preserve their oven-dry condition.

Sample weight, and sample height in the sample cell are recorded for the purpose of subsequent density calculations. With the sample in the sample mount, the bridge is nulled after every 30°C sample temperature increase. The actual sample temperature at the null condition of the bridge is recorded by the marker on the X-Y recorder. The attenuator and phase shifter readings are recorded.

A second set of measurements at the same temperatures recorded before is made with an empty cell using the same procedure mentioned above. These two sets of data are then compared and the change of attenuation, $\Delta\alpha$, and phase, $\Delta\phi$, at different temperatures calculated. These data are then used in the computer program which is programmed to solve for

the complex dielectric constant at each temperature using the analytical equations developed in Chapter two.

E. Measurement errors

1. Mismatch errors

The microwave bridge is matched to have a maximum return loss of 22 decibels at any junction in the bridge, see figure 3-1. The power reflection for return loss of 22 decibels is only 0.627% and maximum attenuation due to any single mismatch is 0.028 db. Thus the error due to mismatch of the microwave bridge is neglected. Throughout the temperature range (23°C to 900°C), reflection due to the sample cell is large (up to 70% in power reflection) but it is almost completely accounted for by the multiple reflection theory used.

2. Errors due to thermal expansion

Since the expansion coefficient for fused quartz (5.5×10^{-7} cm/cm°C) is very low, corrections for all lateral and longitudinal dimensions of the quartz cell were unnecessary. The phase shift and attenuation caused by the thermal expansion of the sample ~~cell~~ can be accounted for by doing a series of measurements with respect to temperature with an empty quartz cell. The resultant phase shift¹ is then subtracted from the phase shift measured with a filled

quartz cell to get the true phase shift due to the sample itself. The result of phase shift versus temperature of an empty cell in the waveguide up to 900°C are shown in figure 3-5. The change of attenuation for the same temperature range is found to be negligible (.01 db).

3. Multimode propagation errors

Errors due to multimode propagation are very hard to determine and can only be estimated. It was shown in Chapter two that for the center loaded waveguide, a one mode approximation will yield an error of approximately -10% in the phase constant, β , compared to the exact solution. A two mode approximation will bring the error in β down to -5%, see figure 3-6, but that analysis was done (17) assuming loss-less material. A more accurate analysis accounting for loss in a material was done by Sheikh and Gunn (28). Using the Rayleigh-Ritz technique, they plotted the errors of attenuation and phase constant using the single and two mode approximation and compared them to the exact solution for different values of w/a , and ϵ_r , see figure 3-6. Note that the equivalent ϵ_r for σ of 10 mho/m is 73.31. In our case, the highest total ϵ_r value was less than ten. Moreover, the mode filter built, and the frequency of 2.45 GHz used on WR-284 waveguide prevented the propagation of higher order modes. Consequently, the only contribution to multimode errors were evanescent modes. Henceforth the worse case multimode errors were much less than those indicated in

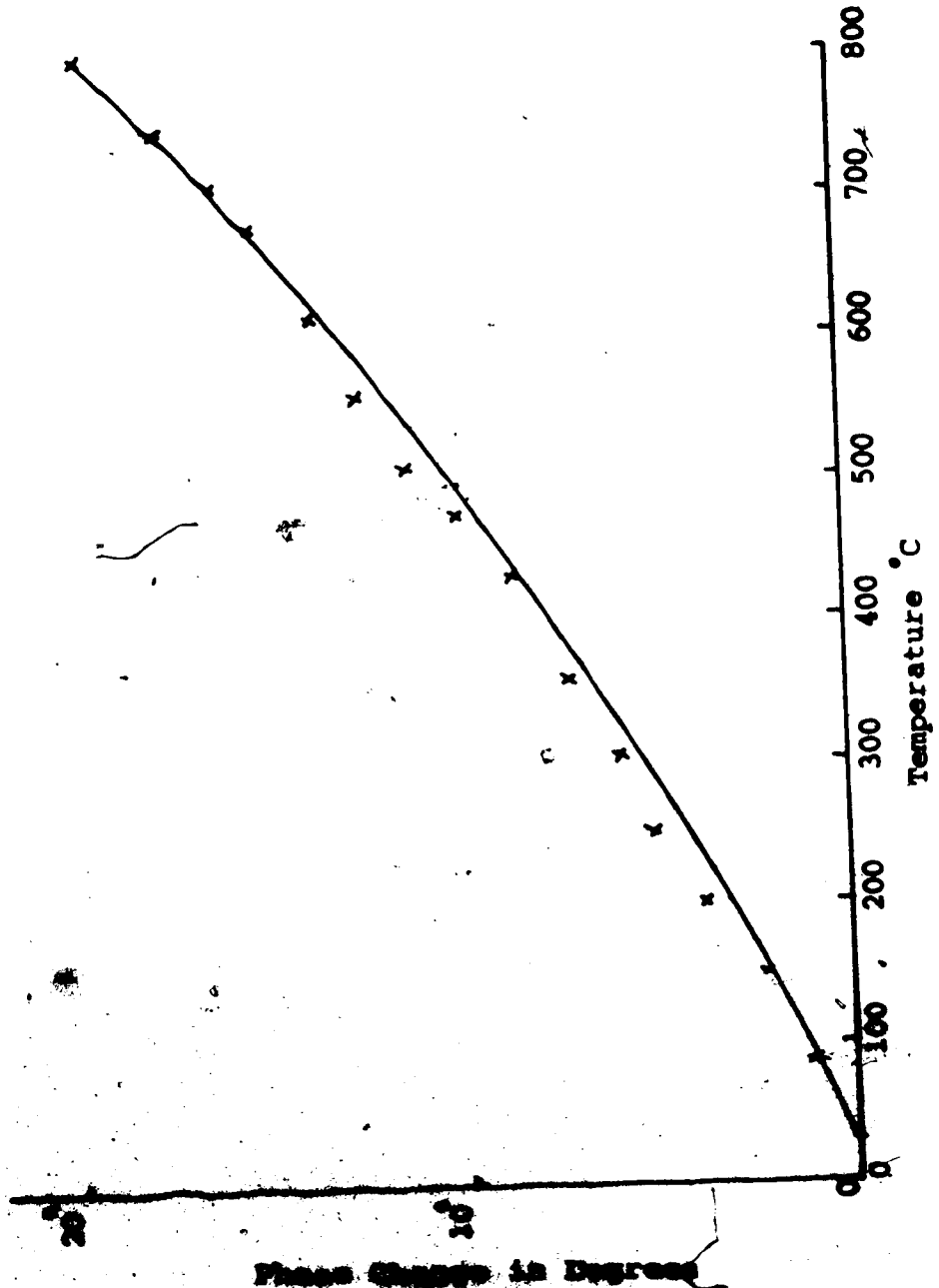


Fig. 2.5 Phase change in a function of temperature due to expansion in phase shift.

Sample mount arm and the reference arm of the bridge (phase shifter, attenuator, sample mount and padding attenuator) is accounted for when the bridge is first nulled. These uncertainties were fed into the analytical model to obtain the resulting total uncertainty in the complex dielectric constant (refer to Appendix A).

F. Heating time measurement using microwave energy

Experimental set-up and measurement procedure

To check on the temperature "cut-off" effect on metal oxides reported by Ford and Pei, temperature versus heating time experiments on cupric oxide, calcium oxide, lead oxide and zinc oxide were carried out. Figure 3-7 gives the block diagram of the experimental apparatus. High power microwaves at 2.45 GHz are generated by a one kilowatt magnetron. The power passes through a 60 db directional coupler^k and a circulator^l before it reaches the sample mount. After the sample mount, the power passes through a triple screw tuner and is dissipated in a matched water load. The triple screw tuner and the water load are tuned to 22 db return loss ($VSWR \leq 1.172$) at 2.45 GHz. Reflected power from the sample mount passes through the same circulator, through a 20 db crossed guide directional coupler^m, a triple screw tuner and is dissipated in a second matched water load. The second triple screw tuner and the matched water load are tuned to 23 db return loss ($VSWR = 1.152$) at 2450 MHz.

Transmitted power to and reflected power from the sample mount is monitored through the 60 db directional coupler and the 20 db crossed guide coupler plus a 40 db attenuator respectively by two power metersⁿ. Power output of the magnetron is controlled by a variac.

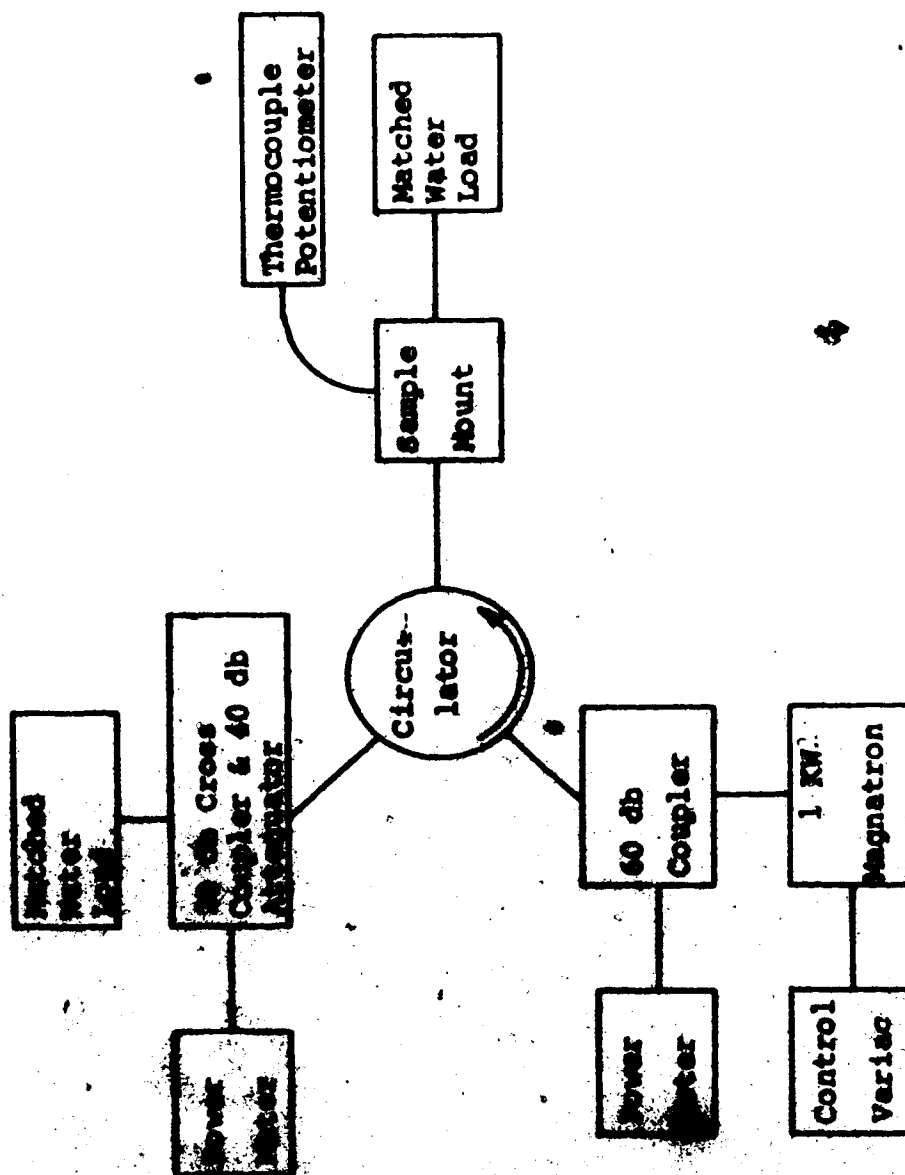


Fig. 3-7 Microwave heating set-up.

The sample mount is simply a waveguide section with a cover on the top broad waveguide wall. The sample is contained in a quartz tube ($3/16$ inches diameter) with a 0.127 inches diameter hole drilled halfway up the tube wall. To monitor the sample temperature, a thermocouple^o is placed through a hole in the narrow waveguide wall and through the hole in the sample tube into the sample.

Sample weight and height in the sample cell are recorded for density calculations. With the sample in the sample mount and the thermocouple placed in the sample, power output of the magnetron is set to about 100 watt. Time is recorded on a strip chart recorder^P for 50°C sample temperature steps up to the maximum temperature while the input power is kept constant. The same procedure is carried out for slightly higher and lower input power levels to check on the so-called "cut-off" temperature effect reported by Ford and Pei.

List of Footnotes

^aHP-S752C. At 2.45 GHz, coupling= 10.2 db, directivity =39.2 db, VSWR= 1.03.

^bMaximum error ± 1.5 degree, insertion loss .025 db, total length of travel= 26.02 cm, total calibrated range= 0 - 360° at 2.45 GHz(26).

^cHP-S382B, 0 - 60 db attenuator, residual attenuation < 1 db. At 2.45 GHz, measured VSWR= 1.21. Uncertainty of attenuation = ± 0.04 db for .5 db attenuation difference. (Calibrated using accurate power meters).

^dPolarad Model RW-T (2.0 to 75 GHz) tuner, Model R (.4 to 84 GHz) Microwave receiver.

^eMaximum temperature the sample mount and the insulating box built around it can stand is 1000°C.

^fA Higgins temperature range extender was no longer available from the manufacturer and hence the above method of temperature range extension was devised.

^gCommercial precision waveguide sections dimension: (3 x 1.5) ± 0.003 inches outside dimension, (2.94 x 1.340) ± 0.003 inches inside dimension.

^hThermal expansion coefficient for stainless steel 304 is 2.02×10^{-6} cm/cm°C. Maximum expansion for the sample mount arm is about 3.0 mm at 900°C.

ⁱMaximum phase shift due to the thermal expansion of the sample mount arm is 20° at 900°C. Attenuation remained constant.

^jFrequency used was 24.5 GHz and $\Gamma = 10$ db/m.

^kHP-111A coupler, 24.3 ± 0.05 db mean coupling, directivity 20.6 ± 1.0 db.

^lVarian Associates Model - 620112.

^mHP-111A coupler, 24.3 db mean coupling, directivity 20.6 ± 1.0 db.

Hewlett Packard Model 431C power meters.

Chromel - Alumel thermocouple and Leeds & Northrop Model 6693 Potentiometer. Temperature detection range 0 - 1200° C.

Hewlett Packard Model 7100B 2-channel Strip Recorder.

CHAPTER 4

EXPERIMENTAL RESULTS AND ANALYSIS

A. Introduction

Results of calibration of the microwave bridge at room temperature are given in table 4-1. These results are compared with results from the literature. Then, following the procedure outlined in the previous chapter, the attenuation and phase shift of cupric oxide, cupric sulfide, lead oxide, zinc oxide, and calcium oxide samples (see appendix C) as a function of temperature were measured on the microwave bridge and the data processed on a digital computer. Various plots of the important variables are presented as a function of temperature and density.

The physical meaning of the relaxation and conduction process is discussed to explain the temperature "cut-off" phenomenon of metal oxides. Plots of temperature versus time of different oxides and sulfides heated by microwave energy are then presented and compared with the results by Ford and Pei (2).

B. Experimental Results

Table 4-1 is the result of experiments used to test the accuracy of the microwave bridge using materials with known complex dielectric constant. As shown in table 4-1, the dielectric constant, ϵ' , has a maximum error of -12% for both quartz and eccofan. These errors in dielectric constant are due mainly to evanescent modes as discussed in Chapter three, section E3. The errors in the loss factor, ϵ'' , are extremely large for the Teflon and Quartz samples. These errors are due mainly to the uncertainty of the attenuator used as change in attenuation, ΔA becomes very small. Since minimum uncertainty of the attenuator used is .04 db at 2.45 GHz, a change in attenuation, ΔA of less than .16 db at .6 db will introduce error of 25%. The method used to calculate uncertainty error is shown in Appendix B. Uncertainty in both real and imaginary parts of the complex dielectric constant of cupric oxide measured by this method are known, but numerical agreement is obtained between the two values of ϵ' .

In figures 4-1 through 4-7, the variation of the complex dielectric constant of cupric oxide, cupric sulfide, calcium hydroxide, and zinc oxide with temperature are given. All measurements were taken at the ISM frequency of 2.45 GHz.

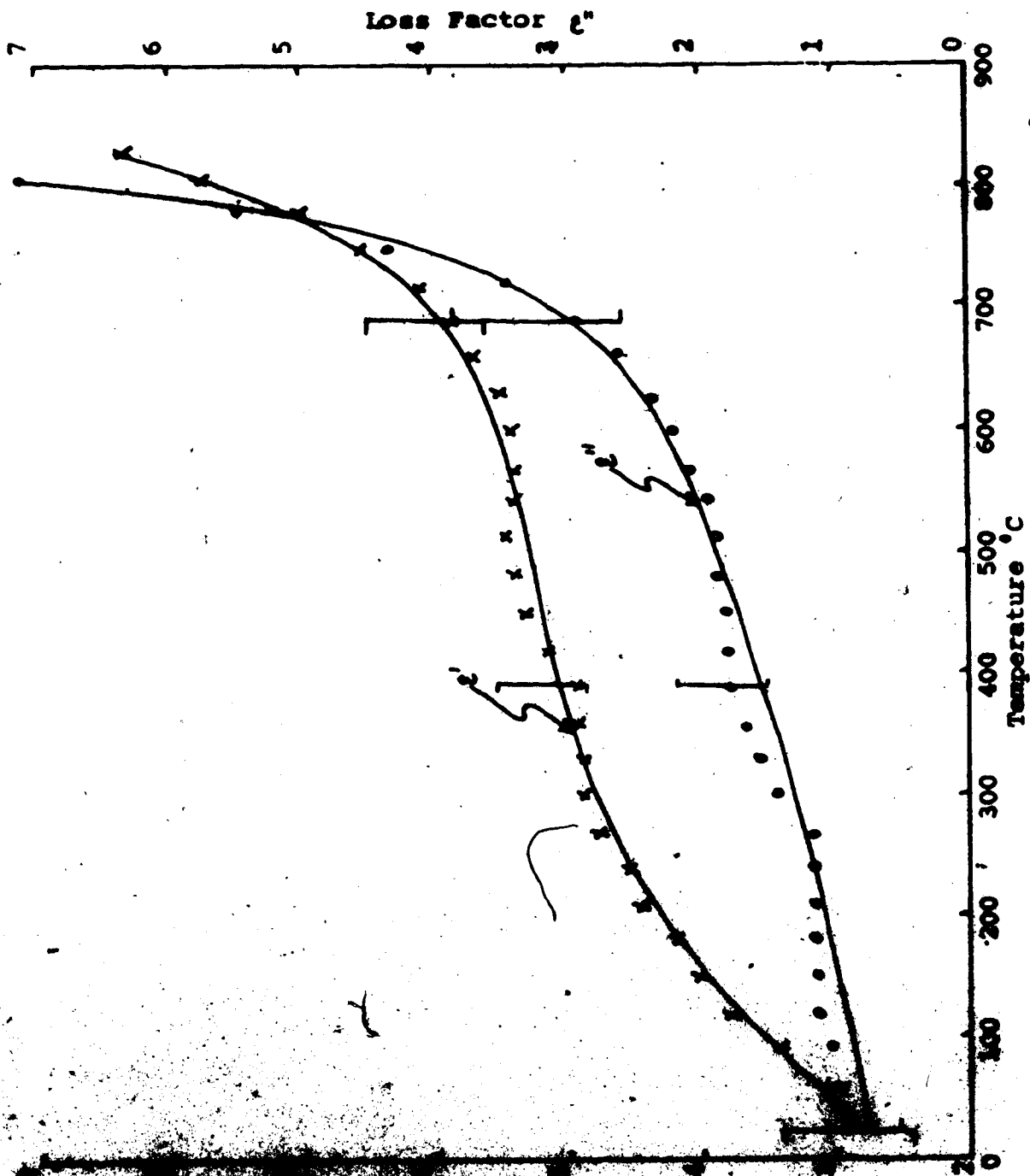
	Test results	Literature Citations	Source
	1. 207-j. 0003	2. 03-j. 0001	Walt, W., "Automatic Measurement of Complex Dielectric Constant and Permeability at Microwave Frequencies", Proc. IEEE, Vol. 62, No. 1, Jan 1974, p. 35.
	2. 201-j. 0006	2. 5-j. 0325	Eccofom Brochure, Standard Products, Emerson & Cuming Inc., Gardena, California.
	3. 29-j. 00	3. 70 -j. 0002368	Eccofom Brochure, Standard Products, Emerson & Cuming Inc., Gardena, California.
200	2. 01-j. 76	2. 01-j. 172	Tings, W.R., private communication.

Table 4-1 Comparison of test results and literature data.

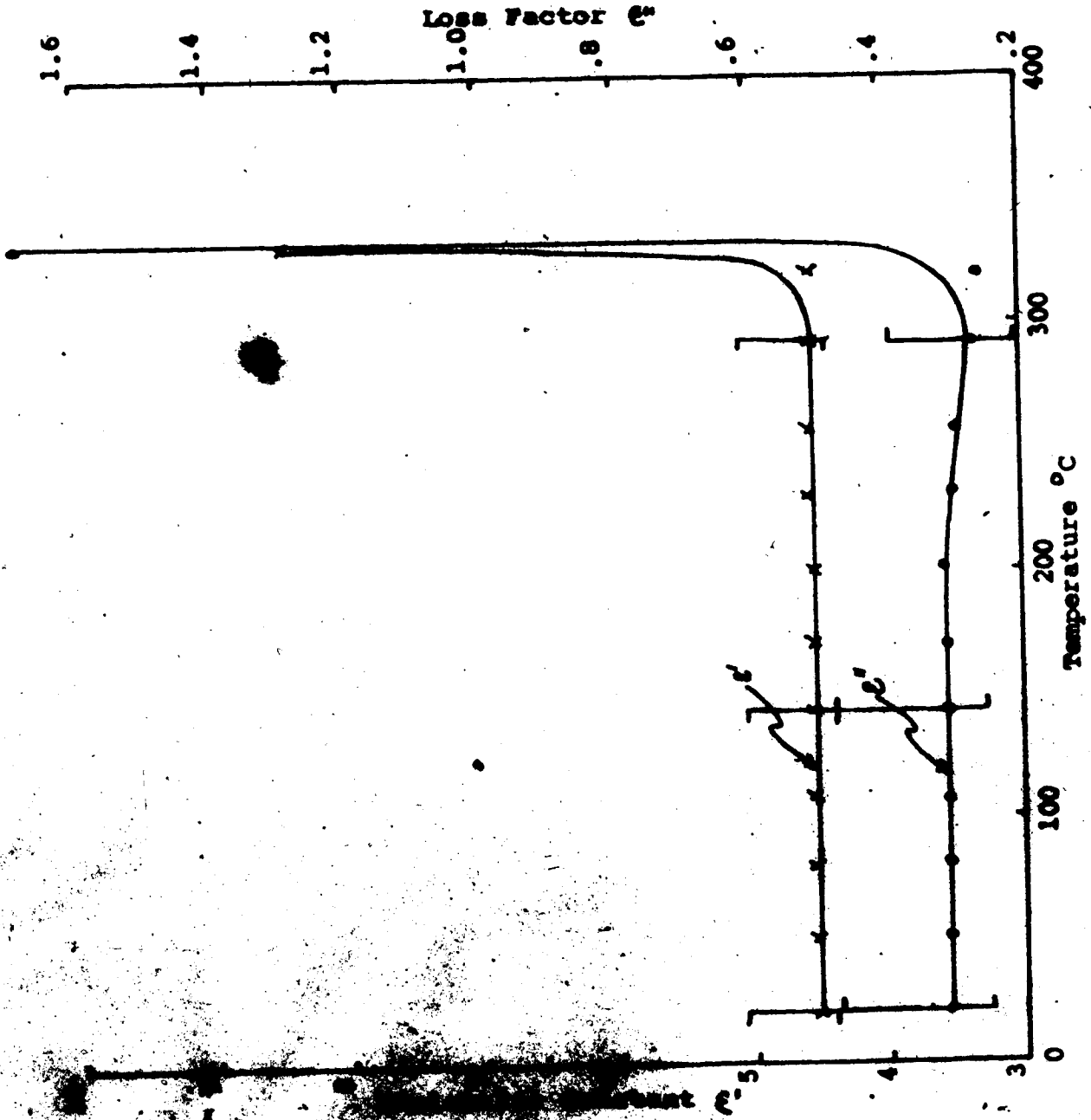
cular frequency, over the given temperature range, both the real and the imaginary parts of the complex dielectric constant of cupric oxide increase slowly with temperature up to 600°C. Beyond 600°C, ϵ' and ϵ'' increase at a rapid rate.

For cupric sulfide, (see figure 4-2), both the real and the imaginary parts of the complex dielectric constant have a near constant value up to around 300°C. Beyond 300°C, they both exhibit a sudden jump to a very high value after which readings on both the phase shifter and attenuator become erratic as temperature continues to go up during the experiment. After the heating sequence, it was observed that the sample had changed state. Sample material at the two ends of the quartz cell had changed to cupric oxide while that in the middle of the cell remained as cupric sulfide. When the heating time was prolonged in a second measurement on cupric sulfide, more of the sample was changed to cupric oxide. It was also observed that sample material which changed into cupric oxide appeared as small chunks rather than in uniform powder form.

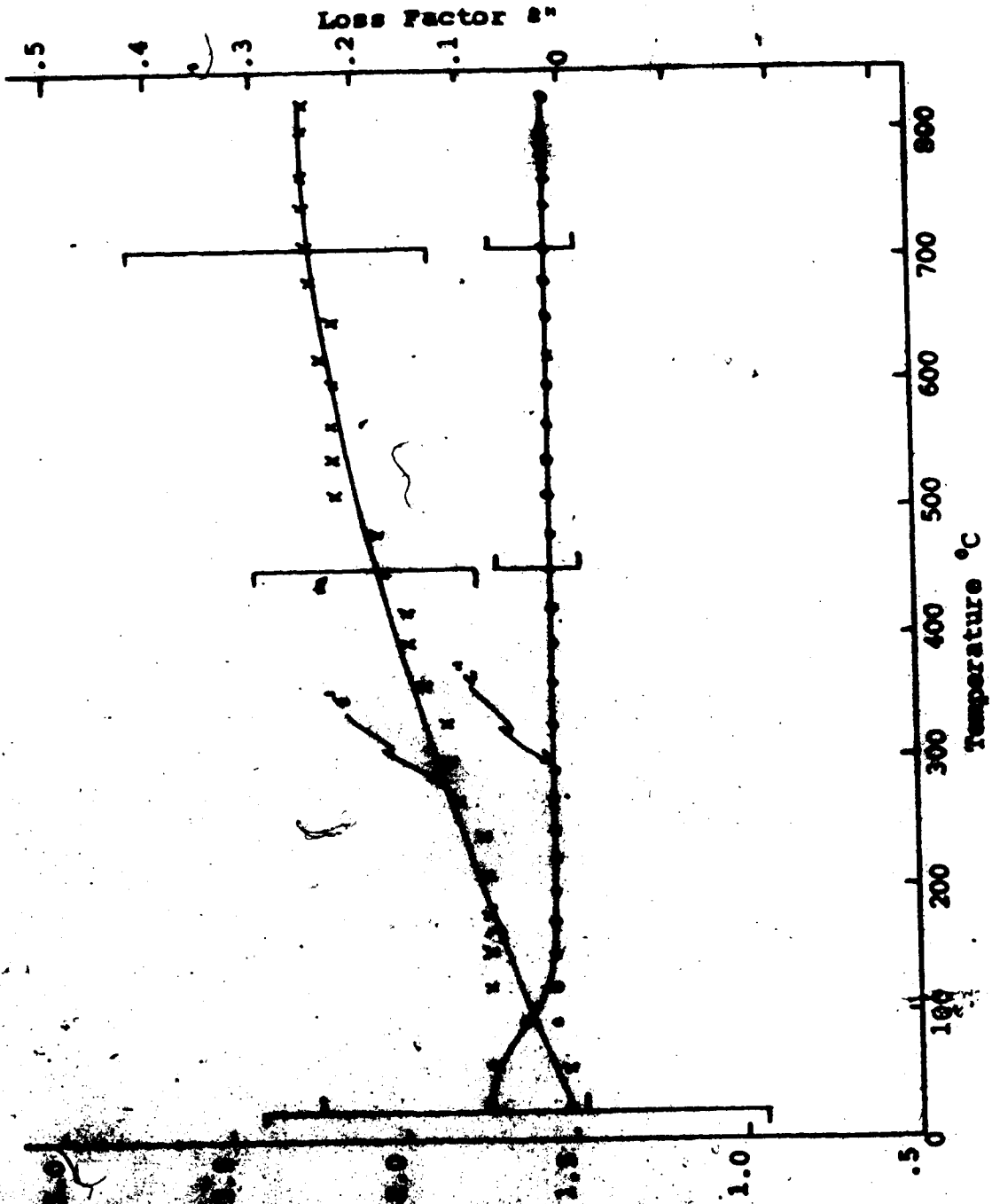
Cupric sulfide seems to be quite stable from room temperature up to 300°C (see figure 4-3). The real part of the complex dielectric constant was constant from 1.87 to 2.28 and the imaginary part was constant at a low value of



Loss factor vs temperature for various dielectric constant and loss tangent at 1.45 GHz and 1.45 GHz.



Temperature dependence of complex dielectric constant and loss factor at 2.45 GHz



Temperature dependent dielectric
loss factor at

Figure 4-4 shows a general increase of dielectric constant, ϵ' , of zinc oxide as temperature goes up. The plot of ϵ' versus temperature exhibits a "hump" at around 280°C. The "hump" also appears in the loss factor, ϵ'' , versus temperature plot at 280°C after which the value of ϵ' dropped down to near the room temperature value at around 500°C before it starts to go up again. Note that the ϵ'' plot is symmetrical on both sides of the hump between room temperature and 500°C. Due to the temperature limitation on sample mount and equipment, the experiment was carried to 800°C rather than the "cut-off" temperature of 1100°C reported by Ford and Pei(2).

Figure 4-5 shows a second interpretation of the same experiment on zinc oxide. A straight line indicating a linear increase of ϵ' between 150°C and 450°C is drawn. This is because the "hump" of ϵ' on figure 4-5 is thought to be due to experimental and/or calculation error. The second interpretation of data on zinc oxide agrees more closely with the explanation on the behavior of metal oxide as a function of temperature given in section C of this chapter. Inspection of the sample after the heating sequence showed that the sample was unchanged in physical appearance indicating a stable compound throughout the temperature range tested.

Lead oxide on the other hand, exhibits a change of

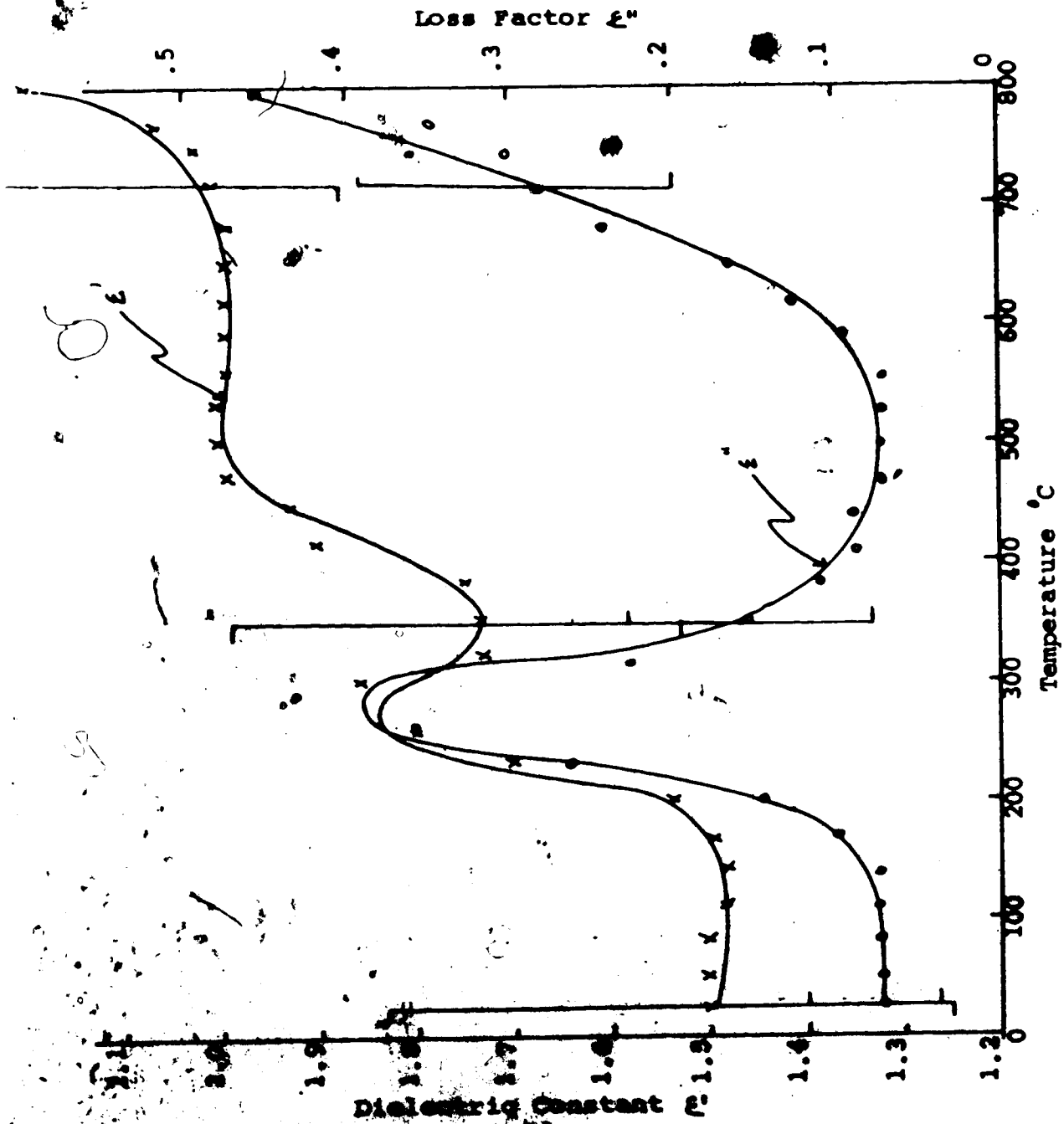


Fig. 4-4 Real and imaginary parts of complex dielectric constant of ZnO as a function of temperature at 2.45 GHz, and density of 6.816 gm/cc. See figure 4-5 also.

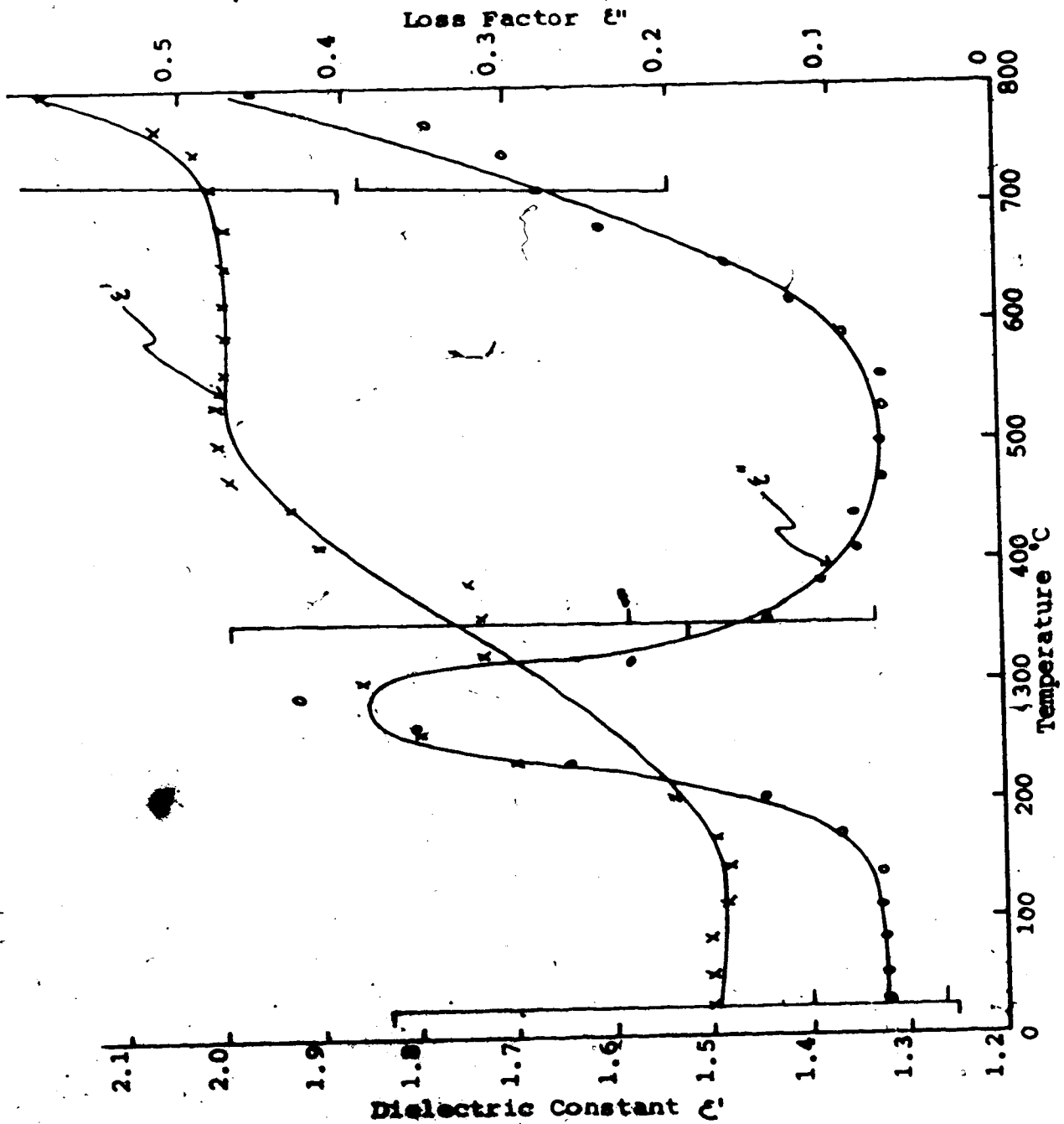


Fig. 4-5 Real and imaginary parts of complex dielectric constant of EO0 as a function of temperature at 2.45 GHz and density of 0.516 gm/cc. (Second interpretation)

physical properties after the powder sample was oven dried at 100°C for 12 hours as shown in figures 4-6 and 4-7. The dielectric constant, ϵ' , stays in the range between 2.2 and 3.5 while the loss factor, ϵ'' , stays in the range between 0.12 and 0.27. It was also observed that after the heating sequence, the sample powder changed from a dark to light yellow color. The experiment was carried out up to around 600°C since the sample starts to melt at around 700°C.

Figure 4-8 shows the temperature versus time curves for cupric oxide using microwave heating. However, the heating curves do not agree with the experiment by Ford and Pei(2). As more power was applied to the sample, the so called "cut-off" temperature increased. For the three different input power levels shown in figure 4-8 (~70 watts, 72 watts and 74 watts) the final steady state temperatures reached were 700°C, 810°C and 888°C respectively. The change of heating rate at around 450°C is due mainly to the geometry of the sample and quartz sample tube, and the temperature profile along the height of the sample^a.

Figure 4-9 shows the percentage power reflection of the sample versus detected temperature^b up to 888°C. Percentage power reflection of the sample reached as high as 65% at 888°C for cupric oxide.

Figure 4-10 shows the temperature versus time curve for zinc oxide. From room temperature up to about 100°C,

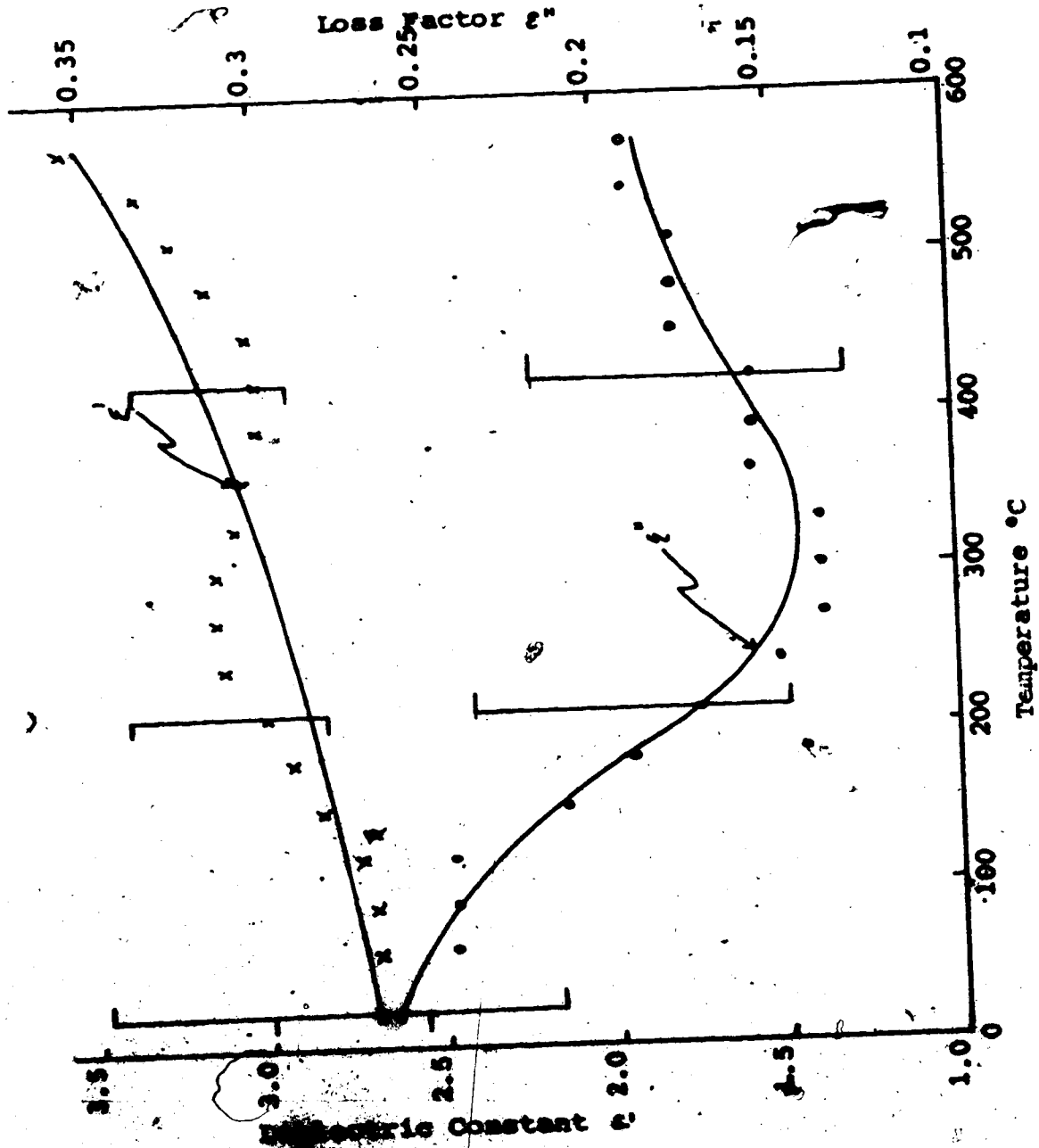


FIG. 4-6 Real and imaginary parts of complex dielectric constant versus temperature at 2.0 g/cc of water at 1.78 g/cc after oven drying at 100°C for 12 hours. See figure 4-7 also.

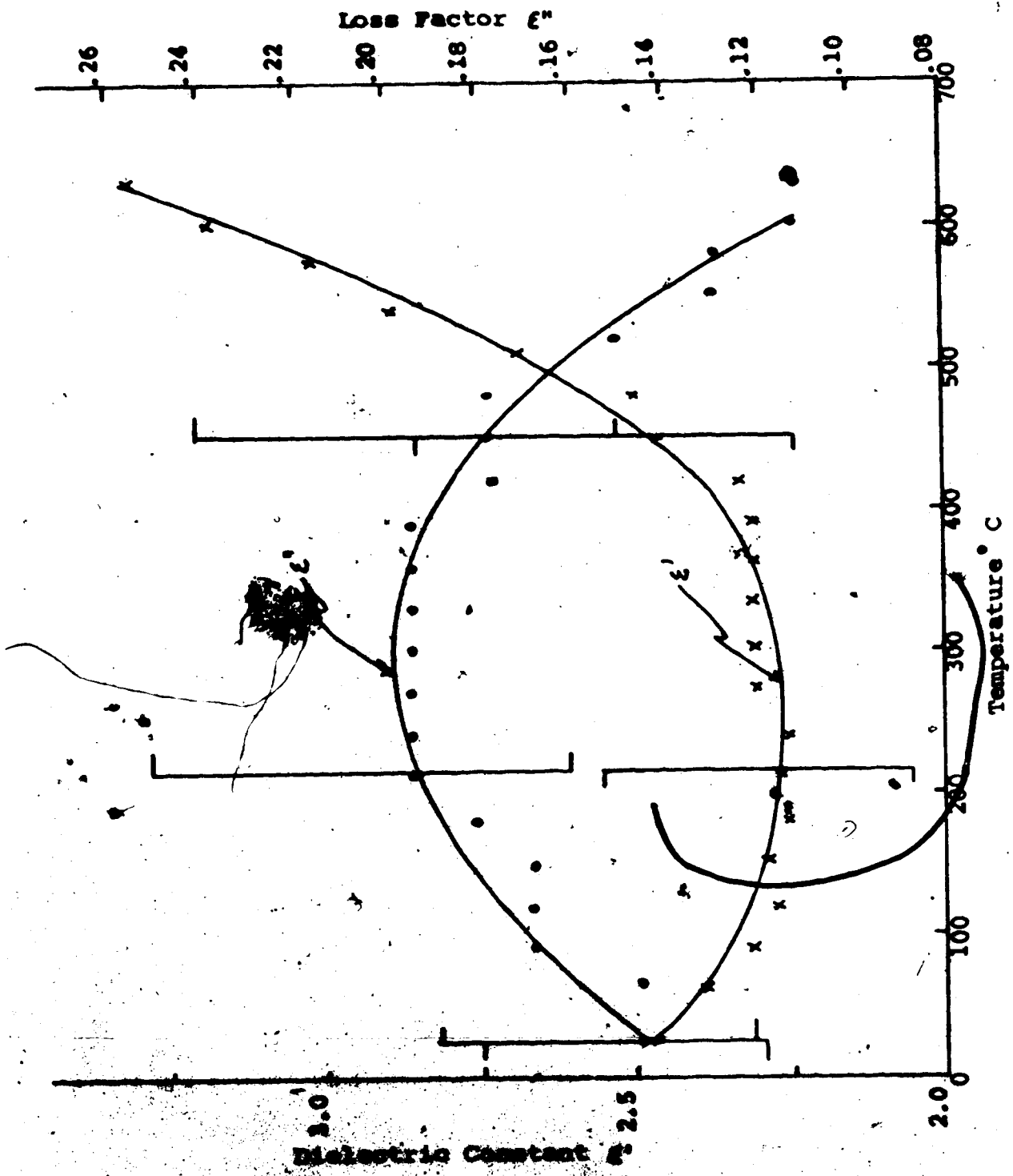


Fig. 4-7 Real and imaginary parts of complex dielectric constant of the polymer as a function of temperature at 2.5 g/cc and quality of 2.23 g/cc before oven drying.

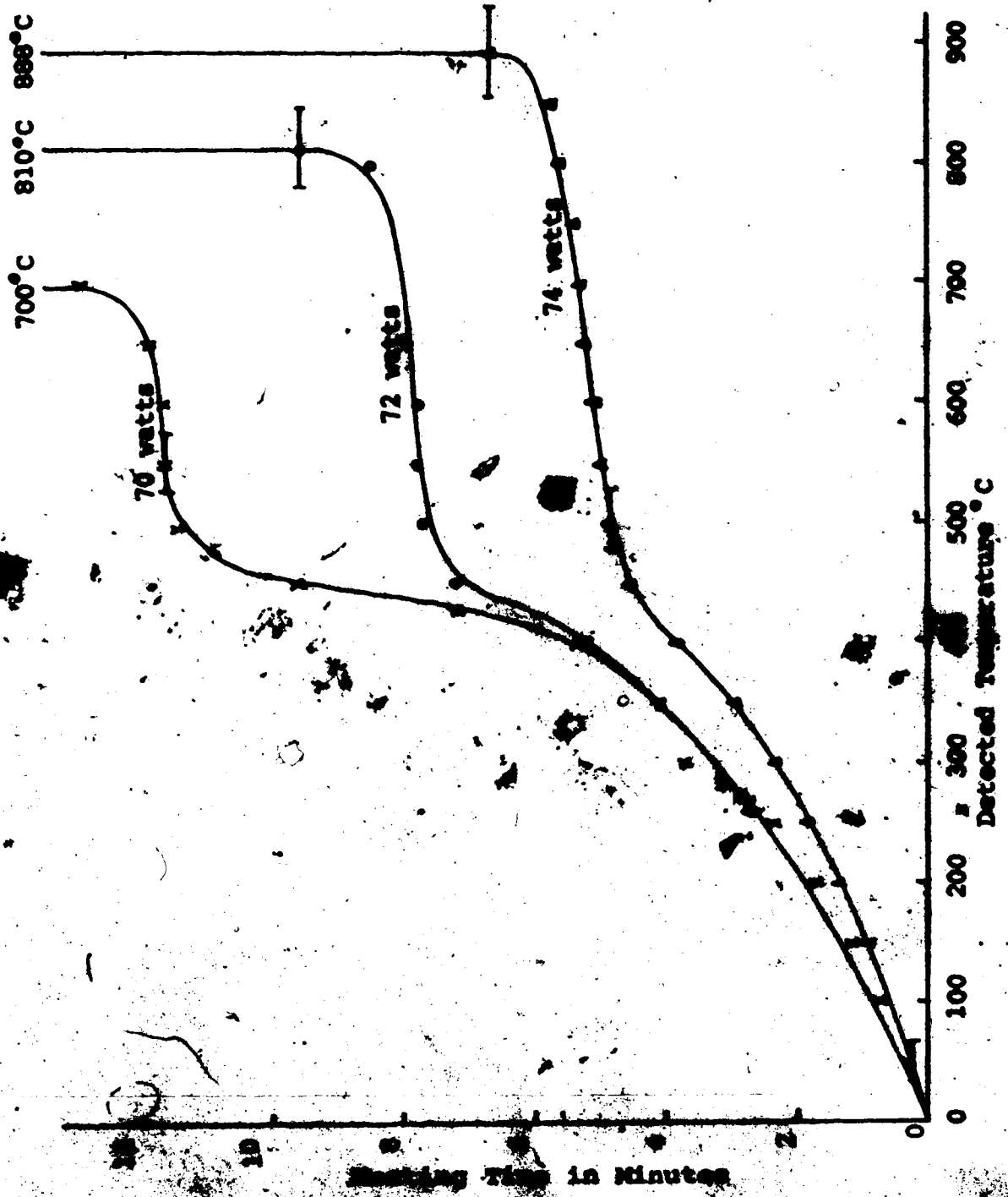


Fig. 2. Detected temperature versus time of CuO using microwave heating with sample density of 2.49 gm / cc.

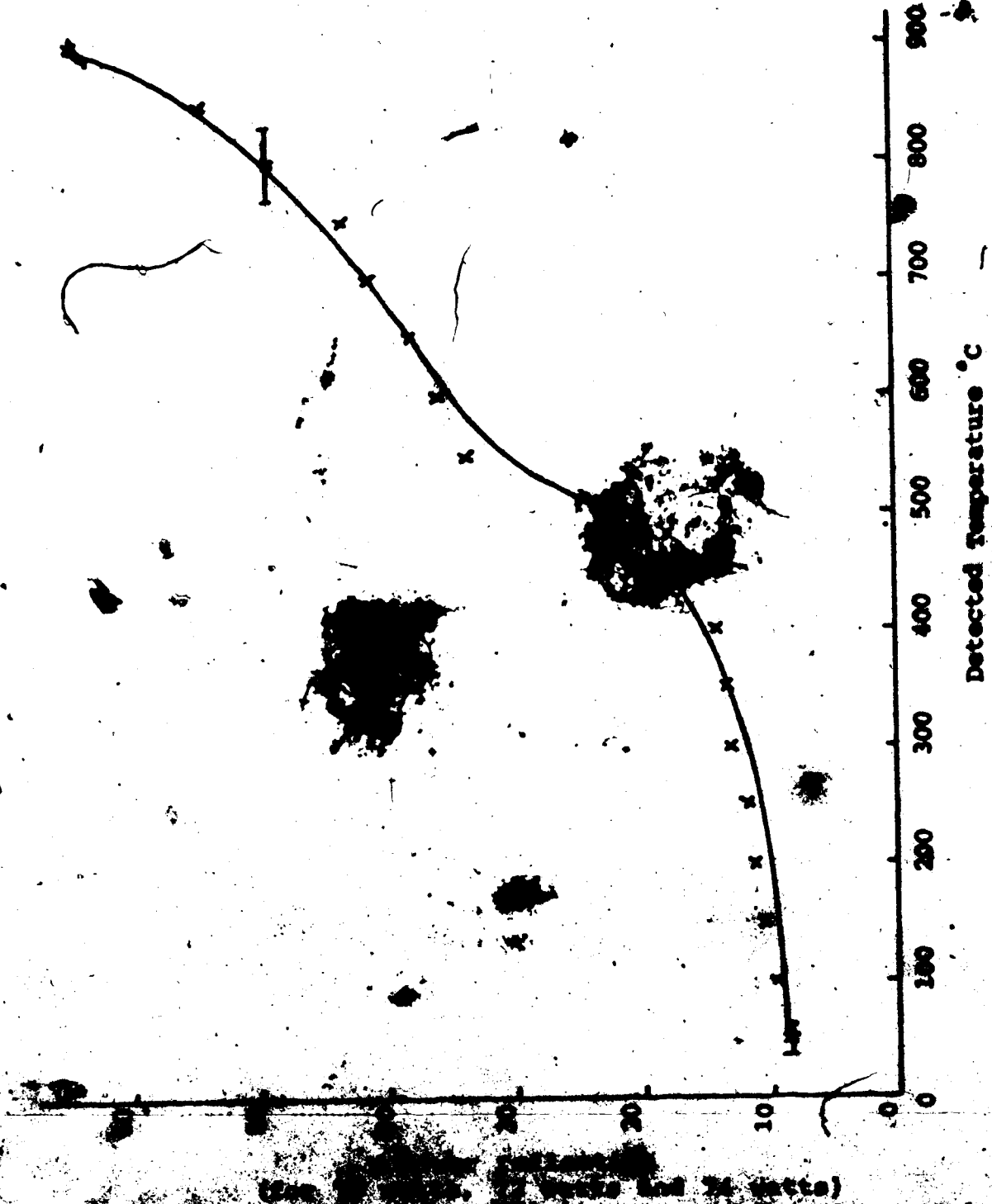
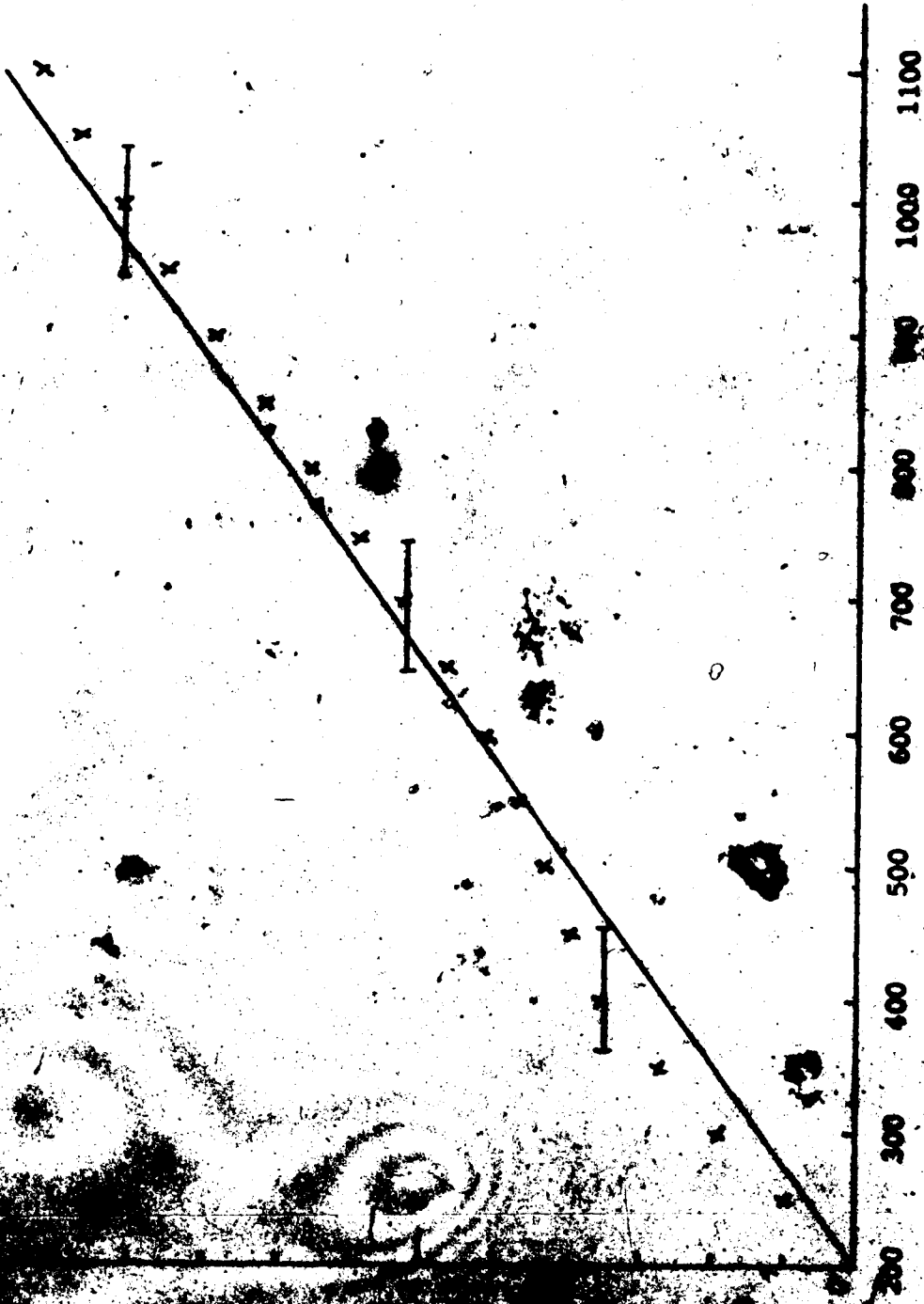


Fig. 4-9 Percentage power reflection versus detected temperature of CuO using microwave heating with sample density of 2.29 gm/cc.



Detected Temperature °C

1.10 Detected temperature versus time for ZnO using microwave heating with sample density of .82 gm / cc.

the heating rate was very slow. Therefore strip-heaters (Cromolox PT-603, 300 watts) were used to heat the sample to 200°C before microwave power was applied. Applying 510 watts incident power at 200°C sample temperature, zinc oxide heated up almost linearly as shown on figure 4-10. In less than two minutes, sample temperature^b reached 1100°C. These results indicate a different cut-off temperature than 800°C reported by Ford and Pei (2) for zinc oxide, since sample temperature^b was still rising when the sample tube cracked at 1130°C. Figure 4-11 shows the percentage power reflection versus detected sample temperature^b for the same compound up to 1100°C. Percentage power reflection increased from about 10% at room temperature to only 16% at 1100°C detected sample temperature.

Lead oxide was tested using 500 watts incident microwave power. Strip heaters were also used to preheat the sample. At preheat sample temperatures of 20°C, 170°C, 200°C, 220°C, 260°C, 307°C, 340°C, 380°C, 510°C and 590°C, the sample heating rate was extremely slow, typically, the heating rate was 1°C/min. At 510°C detected sample temperature, with an incident power of 500 watts, reflected power was 65.6 watts. This is a typical example of the "glow" problem (19) which could occur at high temperatures. At 590°C sample temperature, further heating experiments were not conducted.

Figure 4-11 shows the linear increase of the dielectric

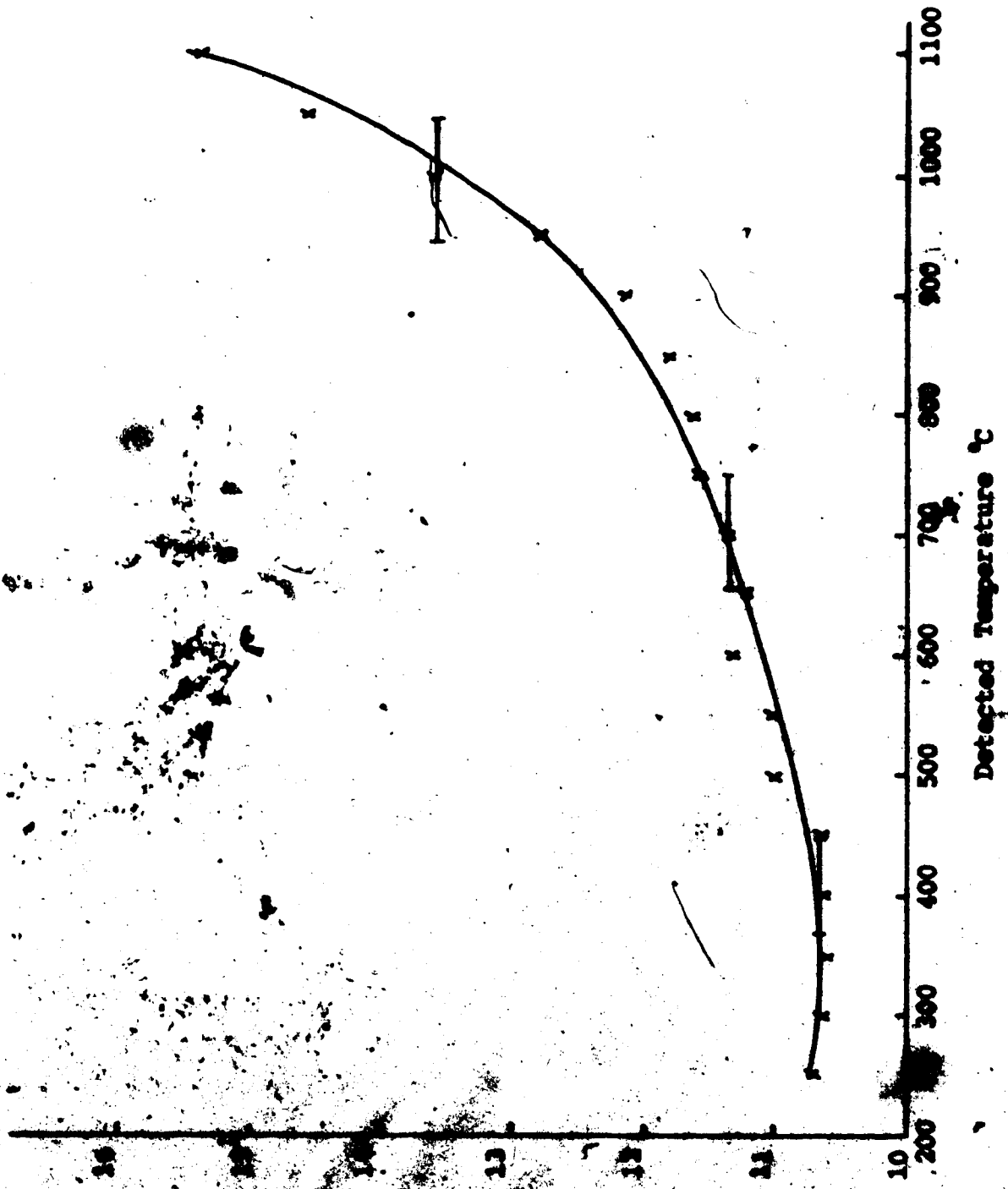
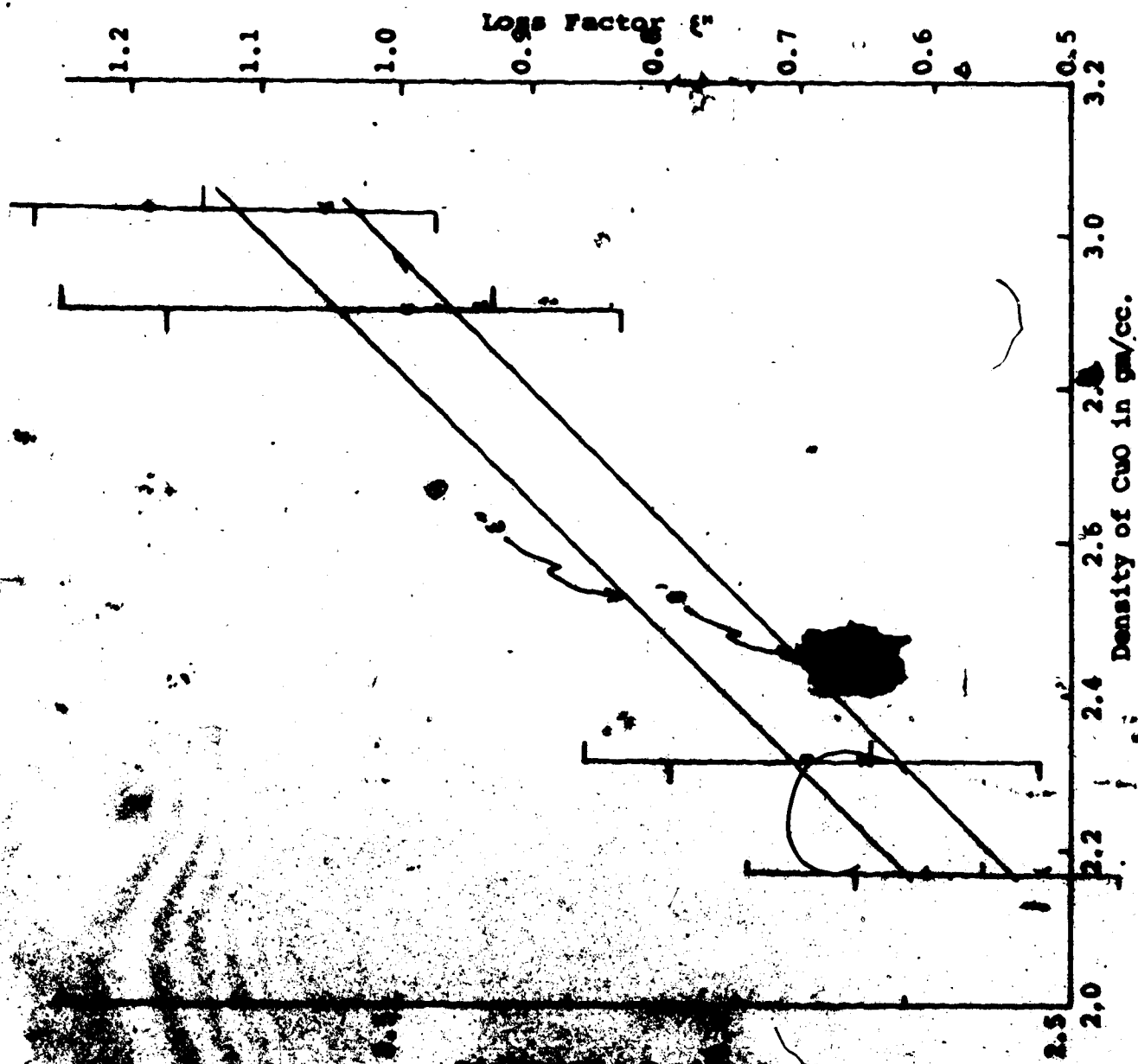


Fig. 4-11 Detected temperature versus percentage reflection of ZnO using microwave heating with sample density of .82 gm / cc.

constant ϵ' and loss factor ϵ'' of cupric oxide as the density of the sample is increased. Since density is directly proportional to the number of molecules in a given volume which in turn is directly proportional to the real and imaginary parts of the complex dielectric constant of the sample, the resultant linear relationship between density of the sample and the real and imaginary parts of the complex dielectric constant of cupric oxide is expected.



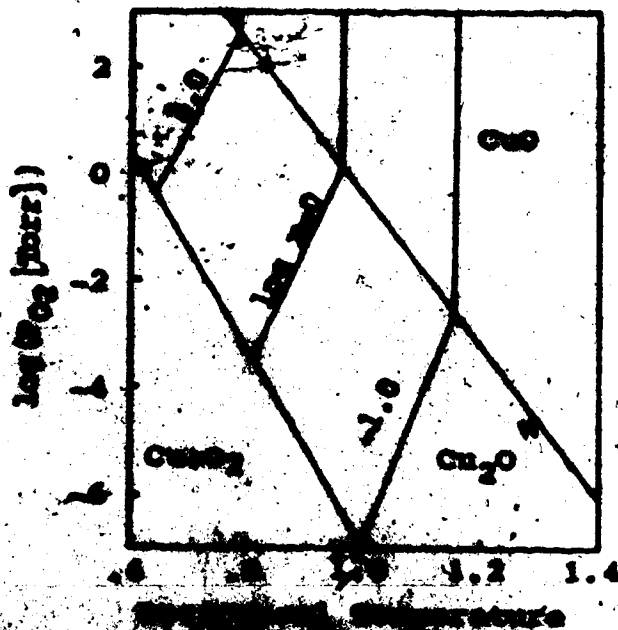
Graph showing the relationship of CuO as a function of density.

C. Analysis of Data

1. Data on physics and metallurgy of materials tested.

Most data on the physics and metallurgy of samples tested can be found in the Handbook of Chemistry and Physics (29) and the Encyclopedia of Chemical Technology (30).

Cupric oxide is black in color, it has a monoclinic unit cell structure and its melting point is 1326°C. That the compound is stable below 900°C and partial pressure of oxygen at one atmosphere (that is, at 152 Torr) can be inferred from a phase diagram in Stecker's paper (31), see figure 4-13.



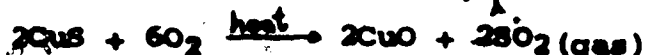
Note that the low conductivity of 10 mho/cm at the same temperature and partial pressure of oxygen is much lower than the conductivity of 10^3 mho/cm indicated in figure 3-6. Thus, errors due to evanescent modes should be much less than that indicated on the same figure.

Zinc oxide is white in color, has a hexagonal unit structure and its melting point is at 1975°C . It loses weight after sintering at 500°C and at oxygen pressure 10 mm from a paper by Secco (32). One possibility of weight loss, according to Secco, is the existence of an unstable superficial suboxide such as Zn_2O or Zn_4O_3 . If the surface of ZnO is covered by a layer of the suboxide, the loss of weight may be due mainly to the dissociation of the surface suboxide. Thus, the sample used for our measurement may not be pure ZnO. A small percentage of it may exist as surface suboxides.

Calcium oxide is colorless and has a cubic unit cell structure. Its melting point and boiling point are at 2580°C and 1480°C respectively.

Carbon dioxide is black in color. At room temperature, it has both a trigonal and a hexagonal unit cell structure. It is stable at room temperature and at 10°C and

oxide and sulfur dioxide gas. The decomposition is a gradual process at temperatures above 220° C. In our experiment, the reaction starts at the two open ends of the quartz cell and gradually proceeds to the middle of the cell. The chemical formula for the reaction is



The experiment for cupric sulfide was carried out from room temperature to the reported "cut-off" temperature of 600° C. Sulfur dioxide gas was given off between 200° C and 300° C during the experiment. After the heating sequence, part of the sample had changed to cupric oxide chunks. Given enough heating time at above 325° C, the decomposition to cupric oxide will complete and the sample will turn completely into cupric oxide.

Lead monoxide is also an unstable compound. It exists in two enantiotropic forms, alpha (yellow, tetragonal, low temperature modification) and beta (yellow, orthorhombic, high temperature modification). Its transitions are slow and the transition temperature is not known accurately (33). Therefore it could exist anywhere from room temperature up to the melting point of lead oxide which is 700° C. The complex dielectric properties show several gross anomalies which are likely to be associated with the change of state of the material. The color of the material changes from dark yellow to black as the temperature increases up to 600° C.

Tests were not carried to a higher temperatures because lead oxide melts at around 700°C.

2. Probable dielectric loss mechanism - dipolar relaxation and conductivity.

The dipole behavior of a molecule may arise from three distinct causes. First, the electron cloud of an atom may shift relative to its nucleus in the presence of an electric field, setting up an induced dipole. This induced effect is called electronic polarization. Second, the molecular structure may be due to an arrangement of positively and negatively charged ions, which can shift from their equilibrium positions under the influence of an electric field, thus giving rise to ionic polarization. Third, the molecules themselves can act as permanent dipoles or dipoles can be induced by an electric field. In the absence of an electric field, dipoles are randomly oriented. Presence of an imposed electric field then causes a partial orientation of the permanent or induced molecular dipoles, causing a net polarization. This is termed orientational polarization. Any or all these effects may be exhibited by a given material.

The five compounds under study, namely cupric oxide, cupric sulfide, zinc oxide, lead oxide and calcium oxide are ionic compounds. They are amorphous in structure and are powders at room temperature. For such materials, if a constant electric field E is applied to them, polarization will not reach a steady state immediately but instead, it will approach it gradually as shown in figure 4-13. If the constant electric field E is suddenly removed after the

steady state value of permittivity is reached, it will take some time for the polarization to vanish as shown in figure 4-14.

The instantaneous change of polarization, from zero to P_1 as shown in figure 4-13 and from P_2 to P_3 as shown in figure 4-14, are caused by the electronic and ionic contributions while the slow build up and decay of polarization is due to an orientational effect. Thus, materials which exhibit only electronic and ionic polarization have a permittivity which is frequency independent at all wavelengths longer than infrared. However, the materials tested in this project do not fit into this category. They exhibit complex permittivities in the microwave frequency range which is due to the frequency dependence of their orientational polarization and conductivity.

For time varying fields, the force opposing the complete alignment of the dipole in the direction of the field is due mainly to random thermal motions. This thermal effect causes the alignment of the dipole to relax exponentially against "viscous" forces.

Debye's (35) classical analysis showed, for dielectric materials with a simple relaxation time, that for the total complex permittivity $\epsilon(\omega)$, as a function of frequency,

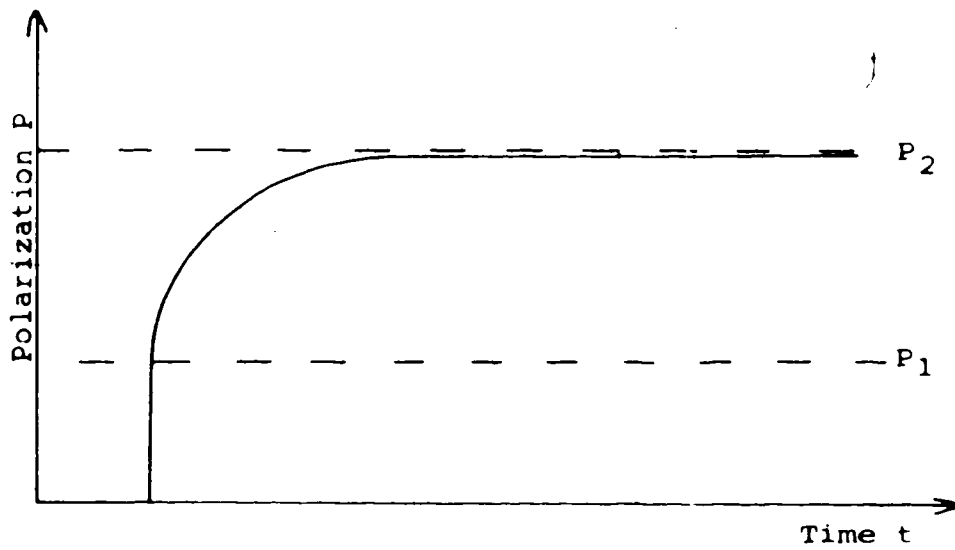


Fig. 4-13 Build-up of polarization upon sudden application of steady field (34).

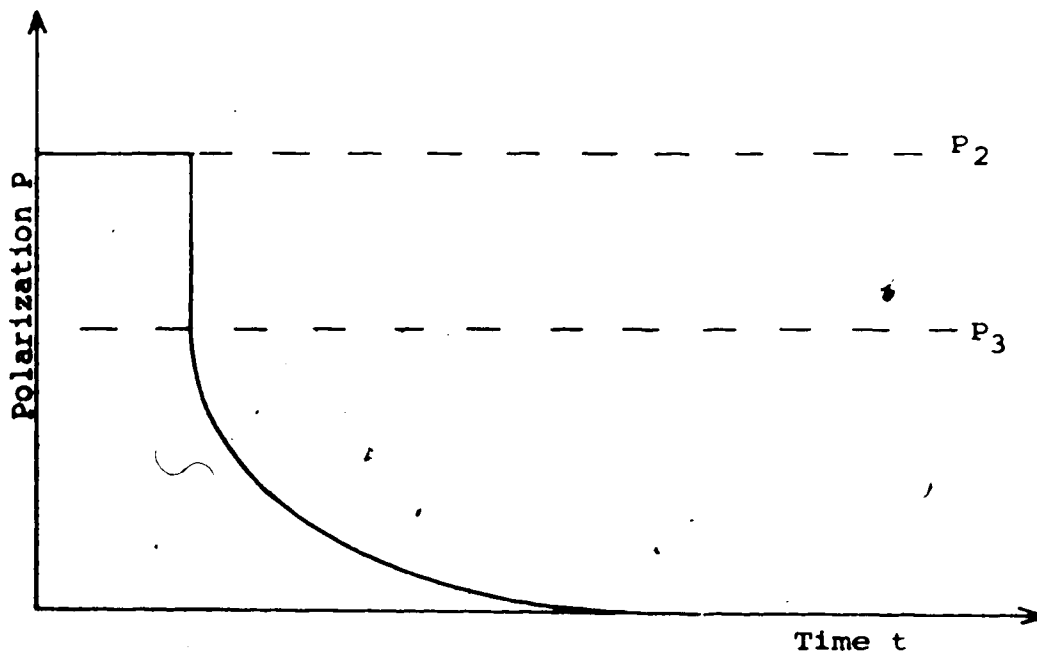


Fig. 4-14 Decay of polarization upon sudden removal of steady field (34).

$$\epsilon(\omega) = \epsilon_{ei} + \frac{\epsilon_s - \epsilon_{ei}}{1 + j\omega t} \quad (4.2)$$

where t is the relaxation time of a particular polarization mechanism. Separating the above equation into its real and imaginary parts,

$$\epsilon'(\omega) = \epsilon_{ei} + \frac{\epsilon_s - \epsilon_{ei}}{1 + \omega^2 t^2} \quad (4.3)$$

$$\epsilon''(\omega) = (\epsilon_s - \epsilon_{ei}) \frac{\omega t}{1 + \omega^2 t^2} \quad (4.4)$$

where ϵ_s is the static dielectric constant and ϵ_{ei} is the electronic and ionic contribution of the complex dielectric constant. Figure 4-15 shows a plot of $\epsilon'(\omega)$ and $\epsilon''(\omega)$ as a function of ωt assuming a value of $\epsilon_s = 8$ and $\epsilon_{ei} = 2$. As ω increases, $\epsilon'(\omega)$ changes smoothly from ϵ_s to ϵ_{ei} while $\epsilon''(\omega)$ has a maximum at $\omega t = 1$.

Since the energy loss per cycle W , within the dielectric material is given by the equation,

$$W = \pi \int \vec{E} \cdot \epsilon''(\omega) \vec{E} \, dV \quad (4.5)$$

when only displacement currents are present.

The maximum absorption of energy occurs when $\epsilon''(\omega)$ is maximum. The frequency at which $\epsilon''(\omega)$ is maximum is called the relaxation frequency.

As the temperature increases, the rate of build up and decay of order of the dipoles imposed by the electric field also increases due to increased kinetic energy of the dipoles. Thus the relaxation frequency increases and

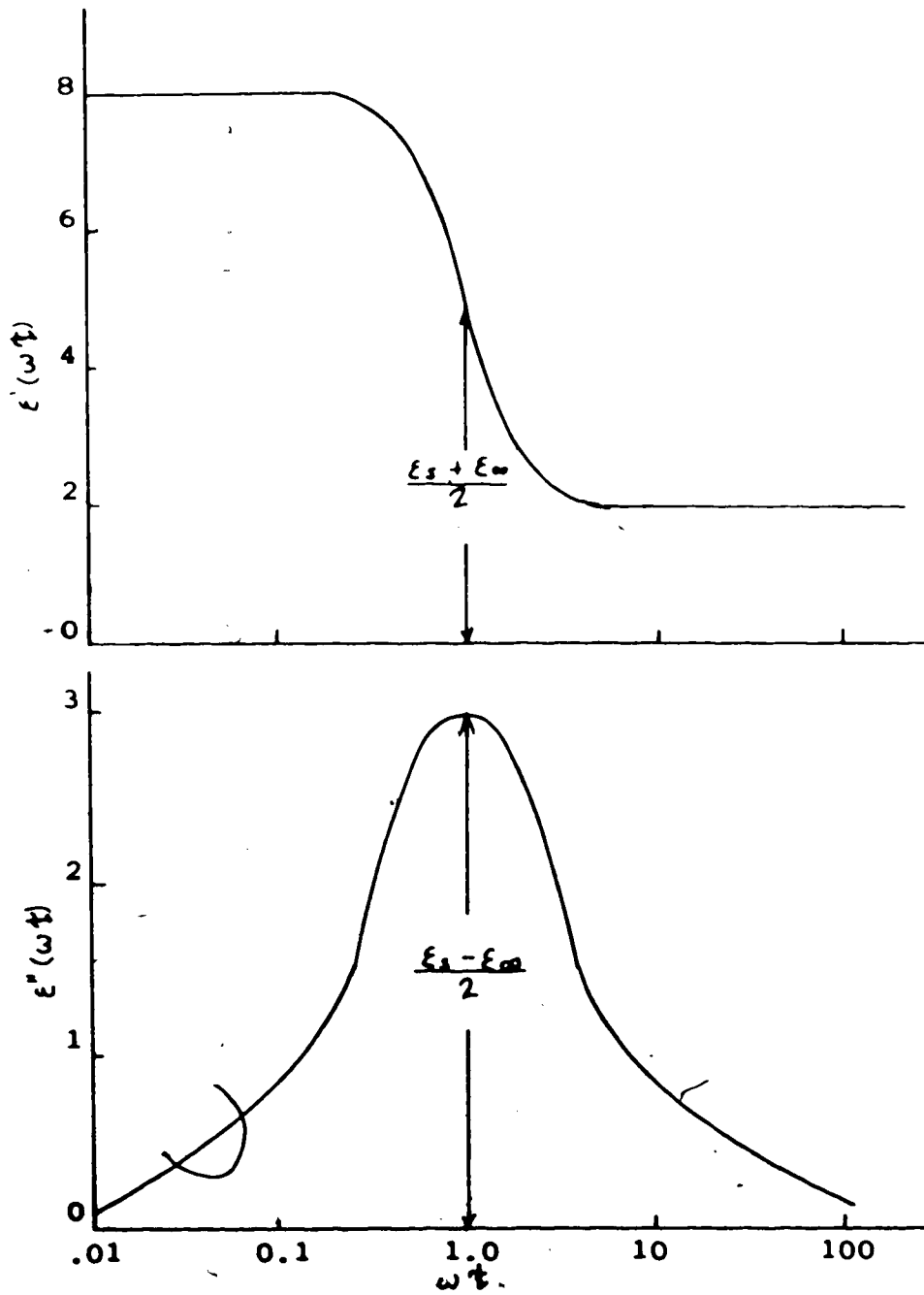


Fig. 4-15 Debye curves for a dielectric material with $\epsilon_s = 8$, $\epsilon_\infty = 2$ (36).

the curves of both the real and imaginary parts of the complex dielectric constant as a function of frequency shift towards higher frequencies as shown in figures 4-16 and 4-17. Thus for a constant frequency, varying the temperature alone, the real part, $\epsilon'(T)$, will go up and the imaginary part $\epsilon''(T)$ will increase to a maximum and then decrease again.

The above analysis accounts for those materials which have only bound charges. But for materials with appreciable number of free charge carriers such as electrons and holes in a semiconductor, there is an ohmic loss caused by the collision of the holes or electrons with the crystal lattice. This ohmic loss and that contributed by dipolar relaxation add directly. So for macroscopic properties of a material, the loss term, ϵ'' , includes the ohmic loss and dipolar relaxation loss.

$$\epsilon''_{\text{total}} = \epsilon''_{\text{dipolar}} + \epsilon''_{\text{conduction}} \quad (4.6)$$

where

$$\epsilon''_{\text{conduction}} = \frac{\sigma}{\omega} \quad (4.7)$$

It is known (37, 38) that electrical conductivity σ can be expressed in the form

$$\sigma = \sigma_0 \exp(aT) \quad (4.8)$$

where σ_0 and a are material constants and T is temperature in degrees Kelvin. Equation (4.8) shows that electrical conductivity of a material is always an exponentially

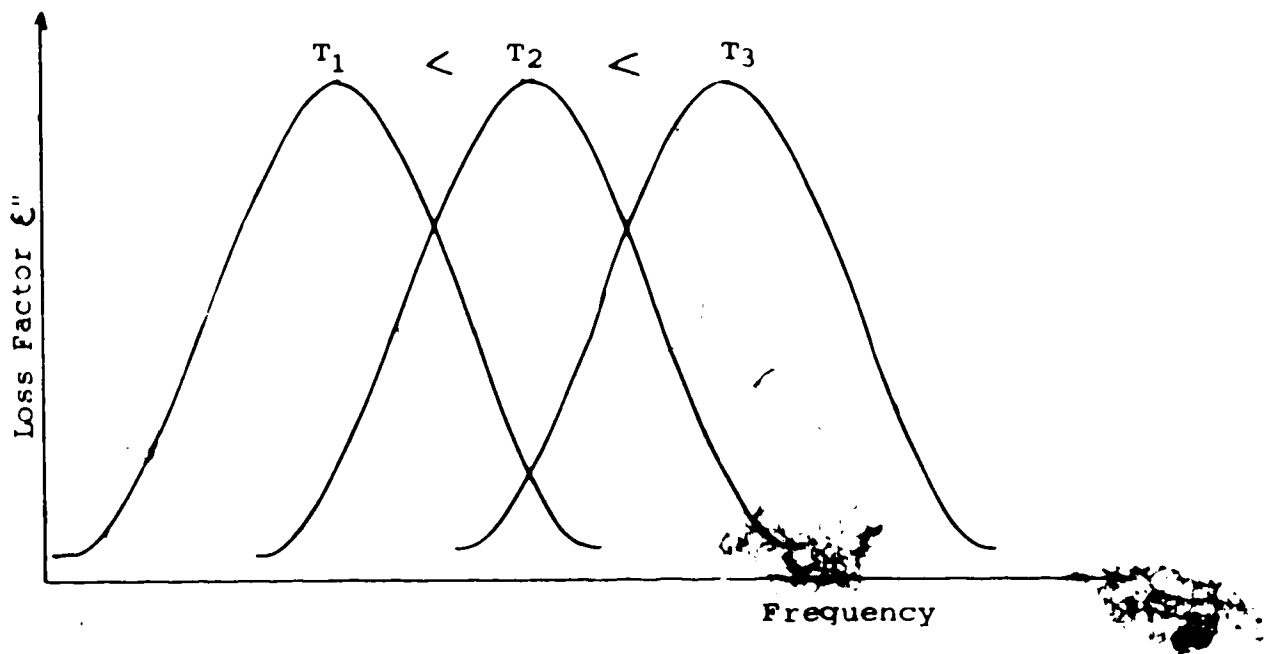


Fig. 4-16 Shift of ϵ'' curve as temperature increases.

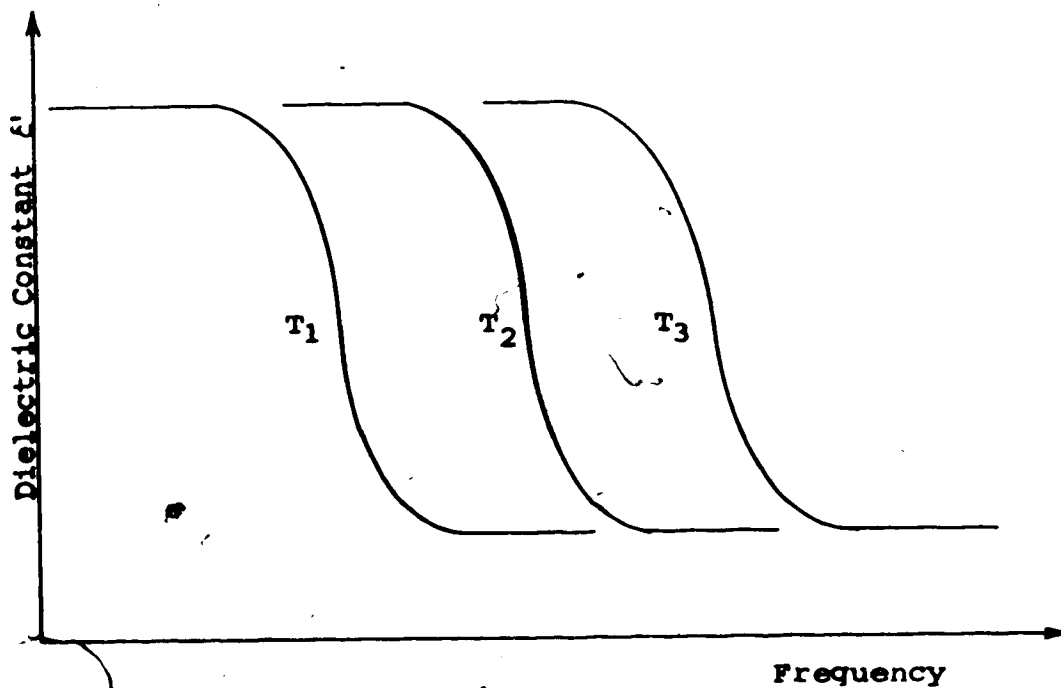


Fig. 4-17 Shift of ϵ' curve as temperature increases.

increasing function of the temperature. Consequently, as evident from equation (4.7), $\epsilon''_{\text{Conduction}}$ will also be an exponentially increasing function of temperature. At low temperatures, the increase of $\epsilon''_{\text{total}}$ will be due mainly to dipolar relaxation if it exists. As temperature increases further, $\epsilon''_{\text{dipolar}}$ will reach a maximum and start decreasing. At still higher temperatures, the conduction loss will start increasing exponentially as shown on figure 4-18.

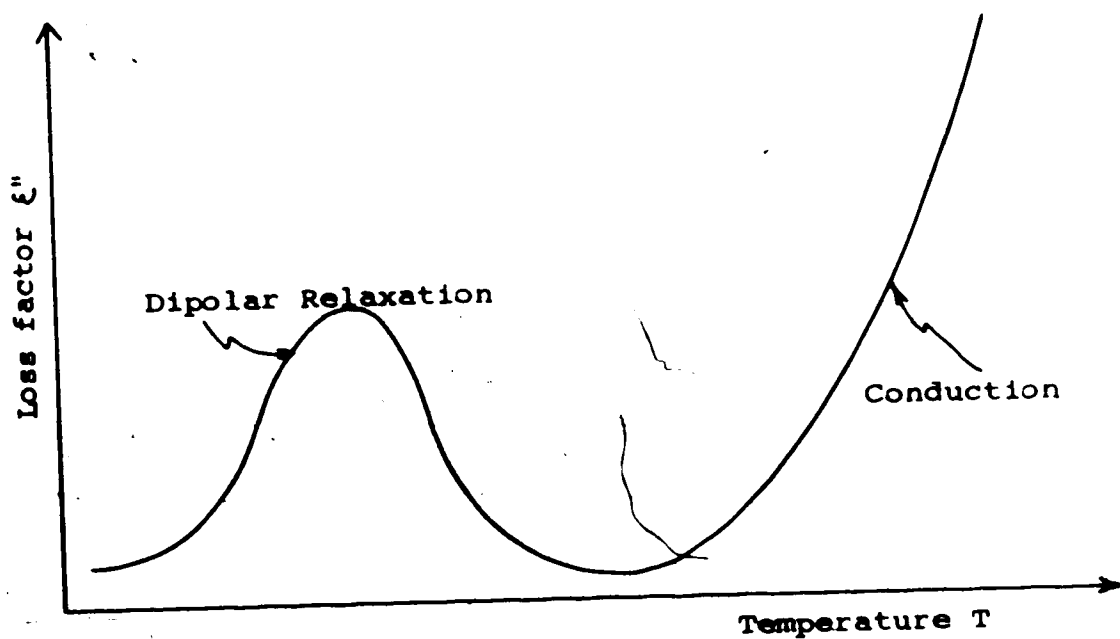


Fig. 4-18 Loss factor ϵ'' as a function of temperature T showing separate effects of dipolar relaxation and conductivity. (Refer to figure 4-4).

However, $\epsilon''_{\text{dipolar}}$ and $\epsilon''_{\text{conduction}}$ may overlap resulting in a plot of $\epsilon''_{\text{total}}$ as a function of temperature as shown on figure 4-19.

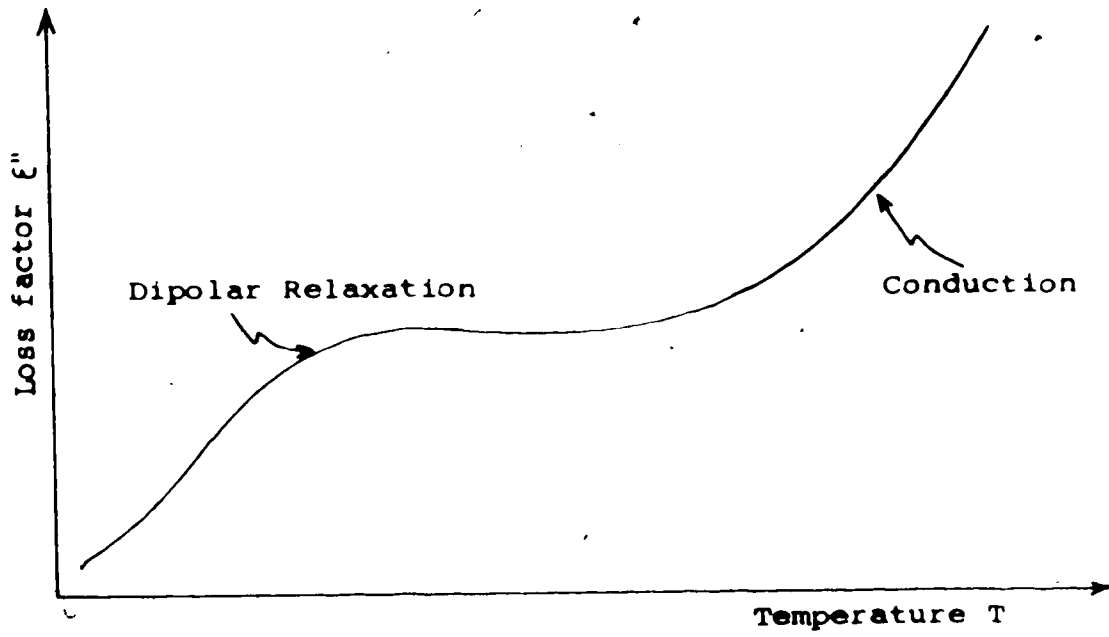


Fig. 4-19 Loss factor ϵ'' as a function of temperature T with effects of dipolar relaxation and conductivity overlap. (Refer to figure 4-1).

3. Explanation of Temperature cut-off Effect.

Results of experiments on the high temperature complex dielectric constant of cupric oxide seem to agree quite well with the theory presented in the previous section. The curves of the real and imaginary parts of the complex dielectric constant of cupric oxide show a sharp increase at around 800°C due to the exponential increase of conductivity. Figure 4-1 shows that the conductivity effect is very strong already at low temperatures. No dipole relaxation peak in ϵ'' is evident even though ϵ' increases between 20°C and 300°C. At least part of the loss factor peak could possibly be found by going to sub-zero temperatures.

Since high values of ϵ' and ϵ'' will cause large reflection, at high temperatures, the sample will reflect microwaves more and more like a metal. But still, some microwave energy is transmitted into the sample and being absorbed. Thus sample temperature should increase until the sample itself melts or decomposes. But this increase in temperature due to microwave absorption could be balanced by the heat loss to the surroundings due to conduction, convection and radiation resulting in a steady state temperature which would give rise to an apparent "cut-off" temperature. The 800°C (+100°C) cut-off temperature for cupric oxide reported by Ford and Pei(2)

may be low, partly due to experimental artifacts. As more power is applied to the sample, more power is reflected but more power will also be transmitted and absorbed by the sample material. This increase of absorbed power will raise the steady state temperature. Results of the heating experiment of cupric oxide show that as incident power is increased, final steady state temperature also increased. But as temperature continues to increase, the conductivity will become so high as to reflect nearly all the microwave energy and a cut-off temperature could ultimately be reached. However, the experimental data is not sufficient to predict what that cut-off temperature would be.

The above analysis holds true only if the material tested doesn't change state or decompose. Since cupric sulfide decomposes in air at around 200°C , the heating experiment for the compound using microwave energy was not performed.

The heating rate for calcium oxide is extremely slow, namely, $0.5^{\circ}\text{C}/\text{min}$ for temperature up to 300°C . The slow heating rate is due mainly to the low loss factor, $\epsilon'' = 0.03$, from room temperature to 800°C as shown in figure 4-3. Due to this low loss factor, little microwave energy is absorbed by the sample material. The slow

absorption of microwave energy is easily balanced by the heat energy loss to the surroundings through conduction, convection and radiation. Due to this slow absorption rate and long heating time, heating time versus temperature experiments using microwave energy were not carried out. Instead, strip heaters were used to preheat the calcium oxide sample to temperature steps of 50°C, 100°C, 150°C, 200°C, 250°C and 300°C. At each temperature step, heating rate of about .5°C/min was observed by applying 150 watts of incident microwave power.

Heating rate of zinc oxide is very slow from room temperature to 200°C. Typical heating rate is 1°C/min. Thus, strip heaters were also used to preheat the sample to 200°C before microwave energy is applied. From 200°C to 1100°C, the heating rate is almost a straight line as shown in figure 4-10. The "cut-off" temperature of 1100°C (±100°C) reported by Ford and Pei(2) is probably low since the temperature was still going up when the sample tube cracked at 1130°C. Heating rate of zinc oxide does not seem to agree with the curves of the real and the imaginary parts of the complex dielectric constant of the sample. The low value of ϵ'' between 400°C and 600°C would indicate a slow absorption of microwave energy. However, since the sample tube for the heating experiment rested on a relatively cool broad waveguide wall, the sample temperature

profile along the sample tube can vary by as much as 300°C between the middle and the ends of the tube. The average value for ϵ' and ϵ'' for the sample along the sample tube will not be the same as indicated at a particular temperature on the complex dielectric constant versus temperature curves. Therefore, the heating experiments using microwave energy is only useful for testing the "cut-off" temperature concept. The heating behavior of samples heated in this manner cannot be determined by data from complex dielectric constant versus temperature curves. Increasing the waveguide temperature (using external heaters) as microwave heating of the sample progresses may be one way to overcome this experimental limitations.

List of Footnotes

^aTemperature difference between the middle of the sample tube and the two ends can be as large as 300°C at 800°C detected sample temperature.

^bTemperature in the middle of the sample tube is detected. Whereas temperature at the two ends of the sample tube can be 300°C cooler.

CHAPTER 5CONCLUSION

The theory of reflection from a multiple interface, combined with the development and limitations of perturbation theory is presented which allows dielectric data of metal oxides and sulfide as a function of temperature up to 800°C to be obtained. The results of the experiments show that the heating rate for a metal oxide is dependent on the complex dielectric constant of the material itself. The transmission of microwave energy into the sample depends on both ϵ' and ϵ'' : The higher the value for ϵ' and ϵ'' , the lower the transmission of microwave energy into the sample. The absorption of microwave energy, on the other hand, is determined by the loss factor ϵ'' . The higher the value for ϵ'' , the more microwave energy transmitted into the sample is absorbed by the sample.

At high temperatures, both ϵ' and ϵ'' show exponential increases with temperature. Therefore, energy impinging on the sample will, mostly be reflected. But some energy will still be transmitted and absorbed by the sample. A steady state temperature is reached when the absorbed energy is equal to the heat energy loss to the surroundings through conduction, convection and radiation. Since the total heat

energy loss is difficult to estimate, the final steady state temperature is difficult to predict.

Due to low absorption of microwave energy, materials with low loss factors are difficult to heat with microwave. This difficulty is shown by the results of the experiment on calcium oxide from room temperature to 800°C.

The measurement method presented is useful for measurement of dielectric materials with ϵ' values ranging from 1.5 to 8, and ϵ'' values between .1 and 7 over a temperature range of 20°C - 900°C. Within these ranges, the total uncertainty error is less than $\pm 15\%$ for ϵ' and less than $\pm 25\%$ for ϵ'' . With ϵ'' values below 0.1, percentage errors may go as high as 150%. This is due mainly to the uncertainty of detecting a small attenuation by the attenuator used. Errors due to the presence of evanescent modes are less than -5% for ϵ' and -10% for ϵ'' .

Once the characteristic impedance for each layer of dielectric is obtained, the reflection, transmission and absorption of microwave energy through three layers of dielectrics can be calculated. The theory of reflections from a multiple interface, presented in chapter two, is useful for such calculation.

Results of the experiment can be used to advantage in

the heating or sintering of metal oxides and/or sulfides. This work also laid a basis for a better understanding of the heating process of metal oxides and sulfides materials using microwave energy. A more detailed study on the physical properties of these materials using more accurate dielectric measurements will likely resolve the remaining uncertainties in the explanation of the dielectric behavior of these materials at high temperatures. A better understanding of the overall dielectric behavior of metal oxides and sulfides as a function of temperature may be achieved by extending the dielectric measurements to sub-zero temperature.

BIBLIOGRAPHY

1. Tinga, W.R., "Interactions of Microwaves with Materials", Proceedings of IMPI, Short Course for Users of Microwave Power, pp. 19-29, Nov. 1970.
2. Ford, J.D., and Pei, D.C.T., "High Temperature Chemical Processing via Microwave Absorption", Journal of Microwave Power, Vol. 2(2), pp. 61-64, 1967.
3. Von Hippel, A.R., Dielectric Materials and Application, John Wiley and Sons, New York, 1954.
4. Ford, J.D., and Tinga, W.R., "Temperature Dependence of Dielectric Constant of Powdered Metallic Oxides", Unpublished work, July, 25, 1968.
5. American National Standard Institute, "Complex permittivity (Dielectric Constant) of Solid Electrical Insulating Materials at Microwave Frequencies and Temperature to 1650°C", D 2520 C59, p. 127, 1970.
6. Wickenden, B.V.A., and Duerden, S.F., "High Temperature Shorted Line Measurement on Alumina at 10 GHz", High Frequency Dielectric Measurement, IPC Science and Technology Press Ltd., Guilford, England, pp. 135-139, 1973.
7. Tinga, W.R., and Nelson, S.O., "Dielectric Properties of Materials for Microwave Processing - Tabulated", Journal of Microwave Power, Vol. 8(73), No. 1, pp. 23-66, March, 1973.
8. Condors, B., and Giroux, M., and Bosisio, P.G., "Dynamic High Temperature Microwave Complex Permittivity Measure-

- ments on Samples Heated via Microwave Absorption", Journal of Microwave Power, Vol. 8(1), pp. 69-82, 1973.
9. Weichman, F.L., "Some Rational for the Universal Behavior of the Dielectric Constant of Cu_2O ", Canadian Journal of Physics, Vol. 51, No. 6, pp. 680-685, 1973.
 10. Montgomery, C.G., "Technique of Microwave Measurements", McGraw Hill Book Co., New York, pp. 570-577, 1947.
 11. Harvy, A.F., Microwave Engineering, Academic Press, New York, p. 235, 1963.
 12. Lynch, A.C., High Frequency Dielectric Measurement, IPC Science and Technology Press Ltd., Guilford, England, p.35, 1973.
 13. Buchanan, T.J., "Balance Methods for the Measurement of Permittivity in the Microwave Region", IEE-Proc., pp. 61-66, 1952.
 14. Stratton, J.A., Electromagnetic Theory, McGraw Hill Co., New York, 1941.
 15. Chamberlain, J., and Chantry, G.M., "High Frequency Dielectric Measurement", Proceedings of a Tutorial Conference on Measurement of High Frequency Dielectric Properties of Materials, IPC Science and Technology Press Ltd., March 1972.
 16. Lynch, A.C., "Transmission Method for the Measurement of Dielectric Loss", High Frequency Dielectric Measurement, IPC Science and Technology Press Ltd., pp. 34-37, March, 1972.
 17. Hord, W.E., and Rosenbaum, F.J., "Approximation Tech-

- nique for Dielectric Loaded Waveguide", IEEE Transaction, Vol. MTT-16, No. 4, April, 1968.
18. Altman, J.L., Microwave Circuit, D. Van Nostrand Co. Inc., New York, pp. 412-415, 1964.
 19. Soohoo, R.F., Theory and Application of Ferrites, Prentice hall Inc., New Jersey, pp. 186-189, 1960.
 20. Tinga, W.R., and Voss, W.A.G., "Microwave Power Engineering", Academic Press, New York, Vol. 2, pp. 189-194, 1968.
 21. Foulds, K.W.H., and Sampaio, P.M.J.C. da S., "Measurement of Electric Field Distribution in a Waveguide containing a Dielectric Slab", Proc. IRE, Vol. 47, pp. 1663-1667, 1959.
 22. Voss, W.A.G., "Advances in the Use of Microwave Power", Seminar Paper, N008, U.S. Dept. of Health, Education and Welfare, p. 16, Feb. 1970.
 23. Ramo, S., Whinnery, J., and Van Duzer, T., Fields and Waves in Communication Electronics, John Wiley and Sons Inc., p. 409, 1965.
 24. Sutton, P.M., "The Dielectric Properties of Glass", Progress in Dielectrics, John Wiley and Sons Inc., New York, Vol. 2, pp. 145-146, 1960.
 25. Tinga, W.R., and Edwards, E.M., "Dielectric Measurement Using Swept Frequency Techniques", Journal of Microwave Power, Vol. 3(68), No. 3, pp. 144-175, 1968.
 26. Stratton, J.A., Electromagnetic Theory, McGraw Hill Co., New York, 1941.

27. Tinga, W.R., "Multiphase Dielectric Theory - Applied to Cellulose Mixtures", Thesis, Dept. of Electrical Engineering, University of Alberta, pp. 62-65, 1969.
28. Sheikh, R.H., and Gunn, M.W., "Wave Propagation in a Rectangular Waveguide Inhomogeneously filled with Semiconductors", IEEE Trans. Vol. MTT-16, pp. 121-177, Feb. 1968.
29. Weast, R.C., Handbook of Chemistry and Physics, CRC Press, Division of the Chemical Rubber Co., Cleveland, Ohio, 54th Edition.
30. Kirk-Othmer Encyclopedia of Chemical Technology, John Wiley and Sons Inc., New York, 2nd Edition, completely revised.
31. Stecker, Von K., "Die Leitfähigkeit des Kupferoxyduls innerhalb des Existenzgebietes bei hohen Temperaturen im Bereich kleiner Drucke", Annalen der Physik, Vol. 3-4, pp. 55-69, 1959.
32. Secco, E.A., "Decomposition of Zinc Oxide", Can. J. Chem., Vol. 38, pp. 596-601, 1960.
33. Moeller, T., Inorganic Chemistry and Advanced Text Book, John Wiley and Sons Inc., New York, p. 688, 1952.
34. Elliott, R.S., Electromagnetics, McGraw Hill Book Co., 1966.
35. Debye, P., "Polar Molecules", the Chemical Catalog Co. Inc., 1929, also Dover Publications, London, 1945.
36. Daniel, V.V., Dielectric Relaxation, Academic Press, New York, p. 17, 1967.

37. White, J.R., "Why Materials Heat", Proceedings of IMPI, Short Course on Theory and Application of Microwave Power in Industry, p. 7, May 1970.
38. Whitehead, s., and Nethercot, W., "The Breakdown of Dielectric under High Voltage, with Particular Reference to Thermal Instability", Proc. Phys. Soc., London, Vol. 47, pp. 974-997, 1935.

APPENDIX A - ERROR ANALYSIS

In this section, the method for calculating the uncertainties of phase shift attenuation and temperature are worked out. The uncertainties in phase shift, $\Delta\phi$, and attenuation, ΔA , are then fed into the computer. The resultant changes in ξ' and ξ'' calculated are taken as the uncertainties in ξ' and ξ'' caused by the uncertainties in the phase shifter and attenuator used. The uncertainty in temperature detected is estimated to be $\pm 5^\circ\text{C}$, $\pm 15^\circ\text{C}$ and $\pm 20^\circ\text{C}$ at 25°C , 400°C and 800°C sample temperature respectively. From the complex dielectric constant versus temperature curves for each compound tested, uncertainties of ξ' and ξ'' due to the uncertainty of temperature are determined.

Resultant worst-case uncertainty errors for cupric oxide at three different temperatures are summarized in Table A-1. Table A-2 gives the total uncertainty errors for different compounds tested using the same method.

Suppose we have two approximations, \bar{x} and \bar{y} , to two true values, x and y , with the respective errors, e_x and e_y . Then we have,

$$\bar{x} - \bar{y} = x + e_x - y + e_y = (\bar{x} - \bar{y}) + (e_x - e_y) \quad (\text{A-1})$$

where the error in the difference, denoted by e_{x-y} is

$$e_{x-y} = e_x - e_y \quad (A-2)$$

Rearranging terms, equation (A-2) becomes

$$\frac{e_{x-y}}{\bar{x} - \bar{y}} = \frac{e_x}{\bar{x} - \bar{y}} - \frac{e_y}{\bar{x} - \bar{y}} \quad (A-3)$$

where $e_{x-y}/(\bar{x} - \bar{y})$ is the ratio of error to the approximate difference. Multiplying the ratio by a hundred gives the percentage error.

For cupric oxide at room temperature, $\Delta\phi = 5.8^\circ$ and $\Delta A = .49$ db have respective uncertainties of ± 0.5 and ± 0.04 db. Therefore, the relative uncertainty in $\Delta\phi$ is $\pm 0.5^\circ/5.8^\circ = \pm 0.086$ or $\pm 8.6\%$. Similarly, uncertainty in ΔA is ± 0.08 db/.49 db = ± 0.16 or $\pm 16\%$. Substituting the uncertainties for $\Delta\phi$ of $\pm 8.6\%$ into the computer program yields $\Delta\xi' = 8.2\%$ and $\Delta\xi'' = 0\%$. Similarly, the uncertainty for ΔA of $\pm 16\%$ yields $\Delta\xi' = 1\%$ and $\Delta\xi'' = 17\%$.

At room temperature, temperature uncertainty, ΔT is $\pm 5^\circ\text{C}$. From the ξ' and ξ'' versus temperature curves, the corresponding $\Delta\xi'$ and $\Delta\xi''$ are $\pm 5.3\%$ and $\pm 1.8\%$ respectively. The total uncertainty error for ξ' for cupric oxide at room temperature is the sum of the uncertainty errors in ξ' . Similarly, for ξ'' , the total uncertainty error is the sum of all uncertainty errors in ξ'' .

Worst case errors due to evanescent modes can be estimated and corrected for as discussed in chapter 3, section F3. Table A-3 gives the worst case error due to evanescent modes for different compounds tested at different temperatures.

T°C	Amplitude uncertainty error	Phase uncertainty error	Temperature uncertainty error	Total uncertainty error
23°C	$\Delta A = 16\%$	$\Delta \phi = 8.6\%$	$\Delta T = 5^\circ\text{C}$	
$\xi' = \pm 1$	1%	8.2%	5.3%	14.5%
$\xi'' = \pm$	17%	0%	1.8%	18.8%
390°C	$\Delta A = 5\%$	$\Delta \phi = 4\%$	$\Delta T = 15^\circ\text{C}$	
$\xi' = \pm$	1%	1.3%	.0%	2.9%
$\xi'' = \pm$	5.1%	.04%	1.9%	7.04%
690°C	$\Delta A = 3.4\%$	$\Delta \phi = 3.5\%$	$\Delta T = 20^\circ\text{C}$	
$\xi' = \pm$.6%	1%	3.05%	4.65%
$\xi'' = \pm$	3.1%	.01%	6.8%	9.91%

Table A-1 Summary of uncertainty errors for CuO.

	CaO	PbO ₁	Pb ₂ O ₃	ZnO ₁	ZnO ₂	Cu ₂ S	CuO
T°C	Rm	Rm	Rm	Rm	Rm	Rm	Rm
Δξ' = ±	5%	6.3%	5%	16.6%	16.1%	2.6%	6.3%
Δξ'' = ±	201%	15.7%	16.2%	47%	48.5%	17.6%	6.8%
T°C	450	210	210	350	350	141	Rm
Δξ' = ±	13%	7.1%	4.5%	11.4%	9.7%	2.3%	6.5%
Δξ'' = ±	161%	17.2%	17.1%	44.7%	45.5%	17.5%	6.0%
T°C	710	470	420	710	710	290	Rm
Δξ' = ±	16.8%	8.9%	3.6%	7.2%	6.4%	2.5%	6.1%
Δξ'' = ±	160%	17.33%	17.6%	26.1%	27.1%	19.6%	5.5%
						T°C	Rm
						ξ' = ±	6.2%
						ξ'' = ±	3.9%

Table A-2 Total uncertainty errors for sample materials tested.

CuO	CuO	PbO _I	PbO _{II}	ZnO _I	ZnO _{II}	CuS	CuO
T°C	Rm	Rm	Rm	Rm	Rm	Rm	Rm
Δε' =	-4%	-5%	-6%	-4%	-4%	-8%	-5%
Δε'' =	-10%	-15%	-16%	-10%	-10%	-24%	-15%
T°C	450	210	210	350	350	141	Rm
Δε' =	-5%	-4%	-7%	-4%	-4%	-8%	-7%
Δε'' =	-15%	-12%	-20%	-12%	-12%	-25%	-20%
T°C	710	470	420	710	710	290	Rm
Δε' =	-6%	-5%	-7%	-5%	-5%	-8%	-7%
Δε'' =	-16%	-15%	-20%	-15%	-15%	-25%	-22%
T°C						T°C	Rm
Δε' =						Δε' =	-7%
Δε'' =						Δε'' =	-23%

Table A-3 Estimated worst case error due to evanescent modes.

APPENDIX B - COMPUTER PROGRAM FOR ITERATION METHOD

This work was run on IBM program product APLSV being run under Michigan Terminal System operation system running on IBM system / 360 model 67 at the University of Alberta.

```

      VPPFL [P]V
V PFTL
[1]  F+24.5
[2]  NUO+O4*10
[3]  P+0.713545028
[4]  X+(O1*Y)+2.658
[5]  P+((10X)+2)*141.6593583*W1*W1
[6]  P+G+T+(O2*X*(1-T)*0.5)+2.597925
[7]  G2+JS D2C
[8]  P1+B20+O2*(P-1)*15.43169918*W*W+
      3.8056
[9]  A1+-O2*15.43169918*W*W*EQ[2]+
      3.8056
[10] G1+(CS A1) CADD JS CS B1
[11] Z0+711.8848955
[12] Z1+(JSO2*X*NUO) CDIV G1
[13] GAQ1+(Z1 CA D-20) CDIV Z1 CADD Z0
[14] GAS1+-GAQ1
[15] GAQ2+-GAC1
[16] GAS2+-GAS1
[17] R1+GAQ2
[18] R2+(GAS2 CADD R1 CMUL CEXP-2*L3*G1) CDIV 1 CAD GAS2
      CMUL R1 CMUL CE P-2*L3*G1
[19] R3+(GAS1 CADD R2 CMUL CEXP-2*L2*G2) CDIV 1 CADD GAS1
      CMUL R2 CMUL CEXP-2*L2*G2
[20] R4+(GAQ1 CADD R3 CMUL CEXP-2*L1*G1) CDIV 1 CADD GAQ1
      CMUL R3 CMUL CEXP-2*L1*G1
[21] T1+1 CADD GAQ2
[22] T2+(1 CADD GAS2) CDIV 1 CADD R1 CMUL GAS2 CMUL CEXP-
      2*L3*G1
[23] T3+(1 CADD GAS1) CDIV 1 CADD R2 CMUL GAS1 CMUL CEXP-
      2*L2*G2
[24] T4+(1 CADD GAQ1) CDIV 1 CADD R3 CMUL GAQ1 CMUL CE P-
      2*L1*G1
[25] T+1 CMUL T2 CMUL T3 CMUL T4 CMUL CEXP-(G1*L3+L1)
      CADD G2=L2
[26] PT+(ABS(T CPHR 2))[1]

```

```

▽RFFLS [P]▽
▽ RFFLS
[1] AT+|(ATC-AT)
[2] PH+|(PHS-PHF)*01+180
[3] G1S+G1
[4] GA 1S+GA01
[5] GAQ2S+GAQ2
[6] R1S+R1
[7] T1S+T1
[8] E2S+E20+02*(ES[1]-1)*15.43169918*W*H+
3.8056
[9] A2S+-0.1*15.43169918*W*H*ES[2]+
3.8056
[10] G2S+(CS A2S) CADD JS CS B2S
[11] Z2S+(JS02*F*UO) CDIV G2S
[12] GAS1S+(Z2S CADD-Z1) CDIV Z2S CADD Z1
[13] GAS2S+-GAS1S
[14] R2S+(GAS2S CADD R1S CMUL CEXP-2*L3*G1S) CDIV 1 CADD
GAS2S CMUL R1S CMUL CEXP-2*L3*G1S
[15] R3S+(GAS1S CADD R2S CMUL CEXP-2*L2*G2S) CDIV 1 CADD
GAS1 CMUL R2S CMUL CEXP-2*L2*G2S
[16] R4S+(GAQ1S CADD R3S CMUL CEXP-2*L1*G1S) CDIV 1 CADD
GAQ1S CMUL R3S CMUL CEXP-2*L1*G1S
[17] T2S+(1 CADD GAS2S) CDIV 1 CADD R1S CMUL GA 2S CMUL
CEXP-2*L3*G1S
[18] T3S+(1 CADD GAS1S) CDIV 1 CADD R2S CMUL GAS1S CMUL
CEXP-2*L2*G2S
[19] T4S+(1 CADD GAQ1S) CDIV 1 CADD R3S CMUL GAQ1S CMUL
CEXP-2*L1*G1S
[20] TS+T1S CMUL T2S CMUL T3S CMUL T4S CMUL CEXP-(G1S*L3+
L1) CADD G2S*L2
[21] PTS+(ABS TS PWR 2)[1]
[22] [+ATC+|10*10*(PTS+PT)
[23] [+PHC+|((ARG TS) CADD-ARG T)[1]
[24] *((( |(PHC-PH))>0.005)*25)+((( |(PHC-PH))<
0.005)*31
[25] +(((PHC>PH)*26)+((PHC<PH)*28)
[26] ES[1]+ES[1]-0.08*|(PHC-PH)*180+01
[27] +29
[28] ES[1]+ES[1]+0.08*|(PHC-PH)*180+01
[29] E+ES+(CS ES[1]) CADD JS CS S[2]
[30] +8
[31] *((( |(ATC-AT))>0.02)*32)+((( |(ATC-AT))<
0.02)*37
[32] +(((ATC>AT)*33)+((ATC<AT)*35)
[33] ES[1]+ES[2]+|(AT-ATC)*1.7
[34] +20
[35] ES[2]+ES[2]-|(AT-ATC)*1.7
[36] +29
[37] E2S+E20+02*(ES[1]-1)*15.43169918*W*H+
3.8056
[38] E2S+E20+02*(ES[1]-1)*15.43169918*W*H+
3.8056
[39] E2S+E20+02*(ES[1]-1)*15.43169918*W*H+
3.8056
[40] E2S+E20+02*(ES[1]-1)*15.43169918*W*H+
3.8056

```

APPENDIX C - IMPURITIES OF COMPOUNDS TESTED

Powdered CuO, ZnO, CuS and PbO used in this work were the Fisher Certified Reagent Grade. The list that follows contains these compounds' impurities. Only CaO was industrially graded.

1. Cupric oxide

Maximum limits of impurities	
Insoluble in HCl	0.02%
Carbon compounds (as C)	0.010%
Chloride (Cl)	0.005%
Nitrogen compounds (as N)	0.002%
Sulfur compounds (as SO ₄)	0.02%
Free alkali	To pass test
Substances not precipitated by H ₂ S (as Sulfates)	0.20%
Ammonium hydroxide precipitate	0.10%

2. Zinc oxide

Maximum limits of impurities	
Chloride (Cl)	0.001%
Insoluble in dilute H ₂ SO ₄	0.004%
Iron (Fe)	0.002%
Sulfur compounds (as SO ₄)	0.002%
Lead (Pb)	0.00002%
	P.T.

Lead (Pb)	0.002%
Manganese (Mn)	0.0003%
Substances not ppt'd by Ammonium sulfide	0.04%
Alkalinity	P.T.
3. Lead oxide	
Maximum limits of impurities	
Nitrate (NO ₃)	0.005%
Iron (Fe)	0.001%
Copper (Cu)	0.000%
Alkalies and earths	0.17%
Insoluble in acetic acid	0.00%
Loss on ignition	0.12%
Chloride (Cl)	0.003%
Bismuth (Bi)	0.01%
Silver (Ag)	0.0002%
4. Copper(II) sulfide	
Maximum limits of impurities	
Chloride (Cl)	0.005%
Iron (Fe)	0.05%
Alkali salts	0.14%
5. Calcium oxide	
Industrial grade	